APPLIED CHEMICAL ENGINEERING

Editorial Board

Editor-in-Chief

Prof. Sivanesan Subramanian
Anna University
India

Prof. Hassan Karimi-Maleh
Department of Chemical Engineering, Laboratory of Nanotechnology,
Quchan University of Technology
Islamic Republic of Iran

Associate Editor

Prof. György Keglevich
Department of Organic Chemical Technology
Hungary

Editorial Board Member

Applied Chemical Engineering

Applied Chemical Engineering

Contents

ORIGINAL RESEARCH ARTICLE

Use of sodium tetraphenyl boron for fabrication of potentiometric membrane sensor for the assay of olanzapine in pharmaceuticals and human urine

Rajendra Prasad Nagaraju*

PG Department of Chemistry, JSS College of Arts, Commerce & Science, B N Road, Mysore 570001, Karnataka, India.
E-mail: prasadtnpur@gmail.com

ABSTRACT

Olanzapine (OLP), chemically known as 2-Methyl-10-(4-methyl-piperazin-1-yl)-4H-3-thia-4, 9-diaza-benzo[f]azulene, is an atypical antipsychotic drug. It is used for the treatment of schizophrenia and bipolar disorder. A new simple and selective membrane based potentiometric sensor was developed for potentiometric determination of olanzapine. The membrane was constructed using an ion-pair of OLP and sodium tetraphenyl boron in dioctyl phthalate and PVC. The membrane provides good linear Nernstian response covering relatively wide concentration range of 4×10^{-6} - 1×10^{-2} M OLP over pH range of 2.6 - 7.8. The detection limit for the developed sensor was founded as 2.02×10^{-6} M. The response time of developed sensor is <10 s for the range of determination. The sensor showed good selectivity for OLP in the presence of various cations, anions and other organic molecules. The membrane was successfully applied in direct potentiometric determination of OLP in tablets. The percentage recovery of OLP, ranged from 96.2 to 99.68% with a mean standard deviation <5%, indicates the adoptability of sensor for the direct estimation of OLP in pharmaceuticals. The developed sensor was used to determine OLP in spiked human urine sample and the satisfactory results were obtained.

Keywords: Olanzapine; Membrane Sensor; Assay; Pharmaceuticals; Spiked Human Urine

1. Introduction

Olanzapine (OLP), chemically known as 2-Methyl-10-(4-methyl-piperazin-1-yl)-4H-3-thia-4, 9-diaza-benzo[f]azulene (**Figure 1**), is the most commonly prescribed second generation neuroleptic agent for the treatment of schizophrenia and other psychotic disorders.
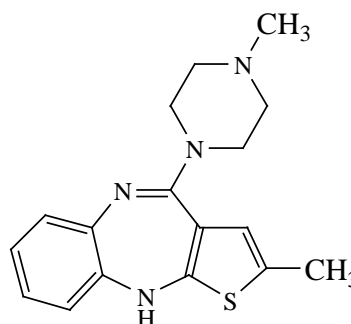
Figure 1. Structure of OLP.

In the literature, titrimetry[1–3], visible spectrophotometry[3–10], kinetic spectrophotometry[11], UV-spectrophotometry[2,12], capillary zone electrophoresis and linear voltammetry[12] and high-performance thin layer chromatography (HPTLC)[13–15] have been reported for determi-

nation of OLP in pharmaceuticals. Several liquid chromatographic methods[16–33] have also been reported for the assay of OLP in pharmaceuticals and biological materials.

Research in the field of development of potentiometric sensors is gaining an increasing number of attention and numerous potentiometric sensors have been developed for the determination of species in the areas of chemical, pharmaceutical and biomedical analyses[34–45]. Potentiometric sensors offers advantages as their use to quantify the compounds since they neither need sophisticated instrument nor relying on stringent experimental conditions.

As presented above, literature did not reveal the report for determining OLP with potentiometric sensor. Hence, an attempt has been made to develop a potentiometric membrane sensor for the determination of OLP in pharmaceuticals and spiked human urine. The membrane sensor has been fabricated by preparing ion pair complex of OLP with sodium tetraphenyl boron using dioctyl phthalate and polyvinyl chloride. Different parameters were optimized to improve the selectivity of membrane to determine OLP with accurate and precise results. The fabricated sensor has been used to develop a new potentiometric method to determine OLP in pharmaceuticals and spiked human urine.

2. Experimental

2.1 Apparatus

Potentials were measured with Labman Micrprocessor based potentiometer (Ahmedabad, India). An Elico (Mumbai, India) pH meter was used to measure the pH of solutions.

2.2 Reagents and materials

All reagents used were of analytical grade. Sodium tetraphenyl boron (NaTPB), dioctyl phthalate (DOP), polyvinyl chloride (PVC), tetrahydrofuran (THF), sucrose, fructose, glucose, maltose, starch, lactose, glycine, sodium fluoride, calcium chloride, nickel chloride, potassium chloride, ammonium chloride, cadmium chloride, cobalt chloride, sodium acetate (NaOAc) and sulphuric acid (H_2SO_4; 98% v/v, Sp. Gr 1.84) were purchased from Merck, Mumbai, India. The drug sample of OLP, certified

to be 99.88% pure, was obtained as gift from Cipla India Ltd, Mumbai, India. Three brands of tablets, namely, Oleanz (2.5 and 7.5 mg OLP per tablet) and Olanex (10 and 15 mg OLP per tablet) marketed by Sun Pharmaceuticals Industries Ltd, Mumbai, India, and Ranbaxy Laboratories Ltd (Solus), Haryana, India, respectively, were purchased from local commercial sources. A fresh urine sample was collected from a 25-year-old men volunteer.

2.3 Standard solutions

A stock solution of 0.01M OLP was prepared by dissolving and diluting the required quantity of pure drug in 0.1M H_2SO_4 in a volumetric flask. All dilutions were made with the same solvent to prepare calibration standards of OLP. Solutions of 0.01 M NaTPB and 2 M NaOAc were prepared by dissolving calculated amount the compound in distilled water. Solutions of 0.001M each of sucrose, fructose, glucose, maltose, starch, lactose, glycine, sodium fluoride, calcium chloride, nickel chloride, potassium chloride, ammonium chloride, cadmium chloride and cobalt chloride were prepared in water.

3. General procedures

3.1 Sensor fabrication

An ion-pair complex of OLP and NaTPB was prepared by mixing 20 mL each of 0.01M solutions. The mixture was stirred for 20 minutes and filtered the obtained yellowish white precipitate. The precipitate was washed with deionized water and dried overnight at room temperature.

The membrane was prepared by mixing 15 mg of ion-piar complex of OLP and NaTPB, 50 mg of DOP and 65 mg of PVC, and dissolving in 5 mL of THF. The content was poured into a Petri Dish of 5 cm diameter and kept for slow evaporation for 24 hours. The master membrane with thickness 0.13 mm was mounted to the softened end of the PVC tube with the aid of adhesive prepared using PVC and THF. A 20 mL of 0.01M OLP solution with 0.25 mL of 0.5 M KCl was filled into the tube. Pure copper wire of 2.0 mm diameter and 15 cm length was tightly insulated leaving 1.0 cm at one end and 0.5 cm at other end for connection. One terminal of the wire was inserted into the tube and the other

terminal was connected to the potentiometer. Silver-AgCl electrode was allied with the membrane as reference electrode. The membrane was conditioned by soaking it into a solution of ion-pair at least for 24 hours.

3.2 Preparation of calibration curve

Into a series of 25 mL volumetric flasks varying aliquots of 0.01 M OLP standard solutions equivalent to 4×10^{-6} - 1×10^{-2} M OLP placed by means of a microburet, the pH were adjusted to ~4.0 with 2 M NaOAc and the final volume was brought to the mark and the contents were mixed well. The potential of each solution was measured by using Ag/AgCl reference electrode and membrane electrode.

The calibration graph of measured potential *versus* –log [OLP] was prepared. The concentration of the unknown was found by using calibration graph or regression equation derived using potential and –log [OLP] data.

3.3 Procedure for interference study

In a 10 ml volumetric flask, 2 ml of 0.01M drug solution and 2ml of 1mM solution of interferent were taken. The solution after adjusted to pH 4 and diluting to mark the potentials of each were measured using the electrochemical cell assembled for preparation of calibration curve.

3.4 Procedure for tablets

Twenty tablets were weighed and ground to a fine powder. Portion of the powdered tablet equivalent to 78.11 mg of OLP was transferred in to a 25 ml volumetric flask and shaken with 20 ml of 0.1M H_2SO_4 for 20 minutes. The content after diluting to the mark with the same solvent was mixed and fil-

tered through Whatman No. 41 filter paper. A suitable aliquot was used to measure the potential by following the procedure as described under procedure for preparation of calibration curve. The concentration of OLP was calculated using the calibration curve or regression data.

3.5 Procedure for spiked human urine

In a 10ml volumetric flask, 1ml of 1:10 urine and 2ml of 0.01M OLP solution were taken. The volume was brought to the mark and mixed well. After bringing the solution to the optimum pH of 4 the potential of the solution was measured using OLP-NaTPB sensor and Ag-AgCl reference electrode. The concentration of OLP in the solution was calculated using the calibration curve or regression data.

4. Results and discussions

The development and validation of ion-selective electrodes using membranes is of interest for pharmaceutical analysis because they offer the advantages of simplicity of fabrication and operation, rapid response time, fair detection limits, acceptable selectivity, accuracy and precision, applicable to the detection of wide concentration range to colored and turbid solutions, and probability to automate and computerize. The acidic solution of OLP reacted with sodium tetraphenylborate and formed a stable 1:1 water insoluble yellowish ion association complex, with low solubility product and suitable grain size precipitate. The probable structure of OLP and NaTPB is proposed and given in **Scheme 1**. This precipitate was used to fabricate the membrane consisting of ion-pair, DOP and PVC.
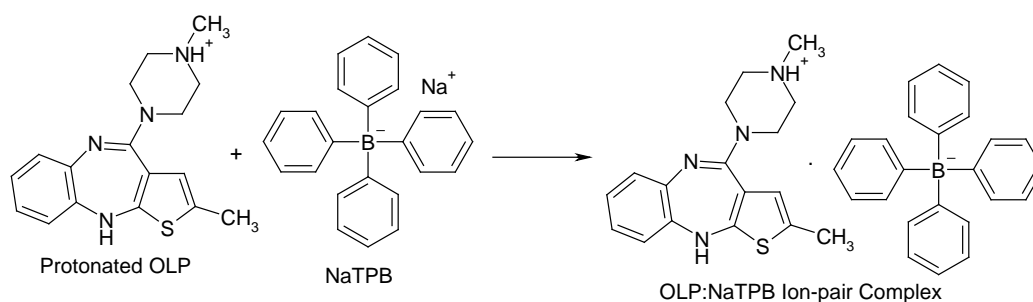
Scheme 1. Reaction pathway for formation of OLP-NaTPB ion-pair complex**.**

Different experimental variables such as pH, soaking time, response time, stability and effect of

ions etc., were studied by measuring the potential of the OLP solution of known concentration using the developed sensor.

The optimum pH range of the sensor was found to be 2.6 to 7.8 and at which the potential measured for each solution of OLP of any concentration within the linear range were almost constant. There is higher and lower potential values were observed at pH lesser than 2.6 and at higher than 7.8 (**Figure 2**).

The developed sensor was subjected to measure the potential of OLP solution in the presence of various organic and inorganic compounds, cations and anions by spiking the solutions of 0.001M each of sucrose, fructose, glucose, maltose, starch, lactose, glycine, sodium fluoride, calcium chloride, nickel chloride, potassium chloride, ammonium chloride, cadmium chloride or cobalt chloride into 6.0×10^{-5} M OLP solution. This was done in accordance to the IUPAC guidelines[46,47]. None of the added species showed effect on the potential. This confirmed that the sensor is selective for the determination of OLP in the presence of such charged or neutral species.
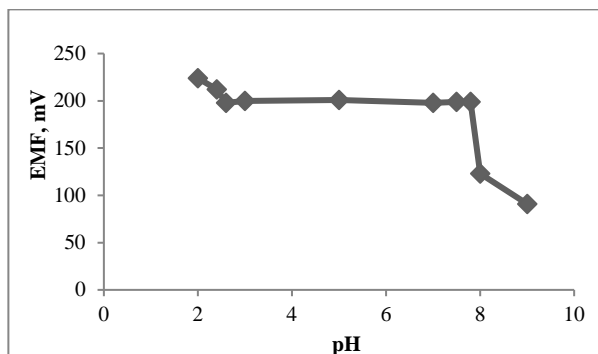
Figure 2. Effect of pH on EMF (6.0×10^{-5} M OLP).

5. Validation results

5.1 Linearity and sensitivity

The electrochemical response parameters of developed OLP-NaTPB sensor was evaluated according to IUPAC recommendations[46,47] using the membrane working electrode and Ag-AgCl reference electrode. The results showed that the sensor provides rapid, stable and linear response for the OLP concentration range 4×10^{-6} - 1×10^{-2} mol L^{-1}. The calibration graph (**Figure 3**) obtained Nernestian response with slope of 60 ± 1 mV/decade. This

confirms that the sensor obeys the linearity equation of $y = mx + c$; where y, c and m refers to E (mV), E^o (mV) and slope (mV/decade) of the curve, respectively. Stable potentiometric readings were obtained with variations within ± 5 mV during the period of 11 weeks. The limit of detection determined from the intercept of the two lines of the calibration graph is 2.02×10^{-6} mol L^{-1}. These results are summarized in **Table 1**.
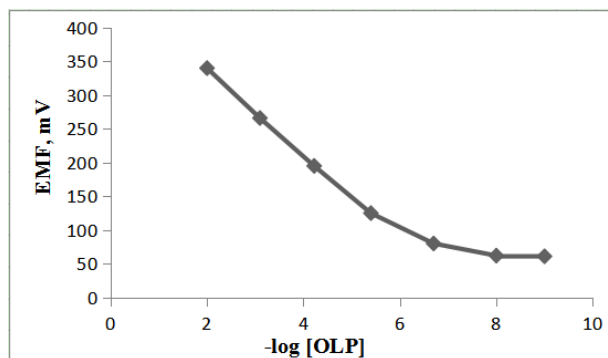
Figure 3. Calibration curve.

Table 1. Electrochemical characteristics of the membrane sensor

Parameters	Values
Linear range, mol L^{-1}	4×10^{-6} - 1×10^{-2}
Limit of detection (LOD), mol L^{-1}	2.02×10^{-6}
Limit of quantification (LOQ), mol L^{-1}	3.15×10^{-6}
Slope (m), mV/decade	60 ± 1
Intercept (b), mV	384.8
Correlation coefficient (r)	0.9996
Response time, s	<10
Working pH range	2.6-7.8
Life span of sensor, weeks	11

5.2 Accuracy and precision

Intra- and inter-day precision were evaluated by analyzing pure OLP solutions at three different concentrations in seven replicates during the same day and five replicates during different days. The amounts of OLP found in each case were computed. Precision for each set of results was assessed by calculating RSD values. The accuracy in the measurement was evaluated by calculating the amount of OLP for respective potentials of drug solution. The relative error (RE), the metric for accuracy, is calculated for each concentration of OLP found. The percent relative error which is an index of accuracy, ranged from 0.2 to 2.0, indicated acceptable accuracy. The obtained RSD values ranged between 2.81 and 4.14% indicated satisfactory precision of the results. These results are presented in **Table 2**.

5.3 Robustness and ruggedness

The robustness of an analytical procedure is a measure of its capacity to remain unaffected by small, but deliberate variations in method parameters and provides an indication of its reliability during normal usage. At the deliberate varied experimental conditions [pH: 4.0($\pm$2) and temperature: 25$\pm$2 ^{O}C], the %RSD, remained unchanged to the actual values. The RSD values ranged from 2.15 to 3.42% confirmed the robustness of the proposed method. In method ruggedness, the analyses with different potentiometers, at different day by different analyst were performed. Such variations did not yield any appreciable change in the measurement. The inter-instrumental and inter-analysts RSD values of <3.4% declares the potentiometric sensor is robust in nature.

Table 2. Results of accuracy and precision study

OLP taken, mmol L^{-1}	Intra-day (n = 7)			Inter-day (n = 5)		
	OLP Found, mmol L^{-1}	% RE	% RSD	OLP Found, mmol L^{-1}	% RE	% RSD
2.00	1.96	2.00	2.81	2.04	2.00	3.45
5.00	5.03	0.60	2.92	5.03	0.60	4.14
10.00	9.92	0.80	2.99	10.02	0.20	2.86

Note: %RE: Percent relative error; %RSD: Percent relative standard deviation.

5.4 Application to tablets

A 5 mL of 0.01M OLP solution of tablets extract prepared under "procedure for tablets" was subjected to analysis by the optimized procedure. The mean measured potential of the tablets extract was found to be equivalent to that of the pure drug and the results were compared with those of a reference method[2].

Table 3. Results of analysis of tablets by the proposed method and statistical comparison of the results with the reference method

Tablet analyzed	Label claim, mg/tablet[a]	Found[b] (Percent of label claim ±SD)	
		Reference method	Proposed method
Oleanz-7.5	7.5	99.17±0.76	98.00±1.21 t = 1.87 F = 2.53
Olanex-10	10	97.15±1.16	99.00±1.21 t = 2.47 F = 1.09

Note: [a]Amount in mg per tablet; [b]mean value of 5 determinations.

The method consisted of the visual titration of the acetous solution of the tablet with acetous per-chloric acid in acetic acid medium. The accuracy and precision were evaluated by applying Student's t- test and variance ratio F- test, respectively. The calculated t- and F- values at 95% confidence level did not exceed the tabulated values and this confirms that there is no significant difference between the reference and proposed method. The mean percent recovery of OLP from tablets was found as 98.5 with RSD value of less than 3%. These data are presented in **Table 3**.

5.5 Recovery study

The accuracy of the sensor was further assessed by following a standard addition procedure. The solutions were prepared by spiking pure drug into a pre-analyzed tablet powder at three different levels and potential measured using the sensor. A 3 mL of 0.01M OLP from tablet five replicate each of 1.5, 3 and 4.5 mL of 0.01 OLP from pure drug were spiked, pH adjusted and after diluting to 25 mL, and the potential measured. For obtained potentials, the amounts of OLP were calculated. The recovery of the known amount of added OLP was calculated. The percentage recovery of OLP from tablets, presented in **Table 4**, ranged from 95.0 to 105.0% with less than 4% of RSD revealed that good and acceptable recovery values were obtained.

Table 4. Results of accuracy assessment by recovery test for tablets

Tablet Studied	OLP in tablet, mmol L^{-1}	Pure OLP added, mmol L^{-1}	Total found, mmol L^{-1}	Pure OLP recovered (Percent±SD*)
Ole-anz-2.5	1.20	0.60	1.78	96.70±0.87
	1.20	1.20	2.36	96.70±1.00
	1.20	1.80	3.02	101.1±3.44
Ole-anz-7.5	1.20	0.60	1.83	105.0±2.33
	1.20	1.20	2.41	100.8±1.87
	1.20	1.80	2.96	97.78±3.21
Olanex-10	1.20	0.60	1.79	98.33±0.97
	1.20	1.20	2.34	95.00±1.21
	1.20	1.80	3.03	101.7±2.22
Olanex-15	1.20	0.60	1.82	103.3±2.32
	1.20	1.20	2.43	102.5±1.10
	1.20	1.80	3.08	104.4±2.21

Note: *Mean value of three measurements.

5.6 Spiked human urine analysis

From the analysis of urine sample spiked with known amount of OLP solution, the percent recovery of OLP were ranged from 94.12 to 97.22% with RSD of <5% indicates that the endogenous sub-

stances did not interfere while measuring the potential of the solution of OLP in presence of urine. This inference paved the applicability of the procedure using the developed sensor for physiotherapeutic administration of OLP.

6. Conclusions

This is the first paper describing the fabrication of membrane sensor and its application to determine olanzapine in pharmaceuticals and spiked human urine. The sensor provides fast and linear Nernestian response over a wide range of olanzapine concentration. The sensor has been successfully used in the determination of drug content in pure state, brands of tablets and from spiked human urine with acceptable recovery. The results obtained were highly accurate and precise with good agreement to consider the sensor for its use as a tool to determine olanzapine in routine quality control laboratories. The assembly presents simple, low cost and selective method for direct determination of olanzapine in aqueous media without prior separation.

Conflict of interest

No conflict of interest was reported by the author.

Acknowledgements

References

1. Basavaiah K, Rajendraprasad N, Vinay KB. Microtitrimetric determination of drug content of pharmaceuticals containing olanzapine in non-aqueous medium. Chemical Industry and Chemical Engineering (Quarterly) 2009; 15: 77–81.
2. Firdous S, Aman T, Nisa A. Determination of olanzapine by UV spectrophotometry and nonaqueous titration. Journal of Chemical Society of Pakistan 2005; 27: 163–167.
3. Basavaiah K, Sameer AMA. Sensitive and selective methods for the determination of olanzapine in pharmaceuticals using n-bromosuccinimide and two dyes. International Journal of ChemTech Research 2010; 2: 660–668.
4. Krebs A, Starczewska B, Puzanowsha-Tarasiewicz H, et al. Spectrophotometric determination of olanzapine with N-bromosuccinimide and cerium (IV) sulphate. Analytical Sciences 2006; 22: 829–833.
5. Jasinska A, Nalewajko E. Batch and flow-injection methods for the spectrophotometric determination of olanzapine. Analytica Chimica Acta 2004; 508: 165–170.
6. Rajendraprasad N, Basavaiah K, Tharpa K, et al. Quantitative determination of olanzapine in tablets with visible spectrophotometry using cerium (IV) sulphate and based on redox and complexation reactions. Eurasian Journal of Analytical Chemistry 2009; 4: 193–203.
7. Rajendraprasad N, Basavaiah K. Highly sensitive spectrophotometric determination of olanzapine using Cerium (IV) and iron (II) complexes of 1,10-phenanthroline and 2,2'-bipyridyl. Journal of Analytical Chemistry 2010; 65: 482–488.
8. Basavaiah K, Sameer AMA, Vinay KB. New extractive spectrophotometric methods for the determination of olanzapine in pharmaceutical formulatins using bromocresol green. Jordan Journal of Chemistry 2010; 5: 101–117.
9. Rajendraprasad N, Basavaiah K. Determination of olanzapine by spectrophotometry using permanganate. Brazilian Journal of Pharmaceutical Sciences, 2009; 45: 539–550.
10. Basavaiah K, Tharpa K, Rajendraprasad N, et al. Spectrophotometric determination of antipsychotic drug olanzapine in pharmaceuticals. Jordan Journal of Chemistry 2009; 4: 65–76.
11. Mohamed AA. Kinetic and maximum-absorbance spectrophotometric methods for the determination of olanzapine. Monatshefte für Chemie - Chemical Monthly 2008; 139: 1005–1010.
12. Raggi MA, Casamenti G, Mandrioli R, et al. Quantification of olanzapine in tablets by HPLC, CZE, derivative spectrometry and linear voltammetry. Journal of Pharmaceutical and Biomedical Analysis 2000; 23: 973–981.
13. Patel R.B, Patel MR, Bhatt KK, et al. Development and validation of an HPTLC method for determination of olanzapine in formulations. Journal of AOAC International 2010; 93: 811–819.
14. Shah CR, Suhagia BN, Shah NJ, et al. Stability-indicating simultaneous HPTLC method for olanzapine and fluoxetine in combined tablet dosage form. Indian Journal of Pharmaceutical Sciences 2008; 70: 251–255.
15. Patel S, Patel NJ. Simultaneous RP-HPLC and HPTLC estimation of fluoxetine hydrochloride and olanzapine in tablet dosage forms. Indian Journal of Pharmaceutical Sciences 2009; 71: 477–480.

16. Olesen OV, Linnet K. Determination of olanzapine in serum by high-performance liquid chromatography using ultraviolet detection considering the easy oxidizability of the compound and the presence of other psychotropic drugs. Journal of Chromatography B: Biomedical Science Applications 1998; 714: 309–315.

17. Weigmann H, Härtter S, Sabine M, et al. Simultaneous determination of olanzapine, clozapine and demethylated metabolites in serum by on-line column-switching high-performance liquid chromatography. Journal of Chromatography B 2001; 759: 63–71.

18. Olesen OV, Poulsen B, Linnet K. Fully automated online determination of olanzapine in serum for routine therapeutic drug. Therapeutic Drug Monitoring 2001; 1: 51–55.

19. Concetta D, Gaetana M, Vincenza S, et al. Determination of olanzapine in human-plasma by reversed-phase high-performance liquid chromatography with ultraviolet detection. Therapeutic Drug Monitoring 2006; 28: 388–393.

20. Dusci LJ, Hackett LP, Fellows LM, et al. Determination of olanzapine in plasma by high-performance liquid chromatography using ultraviolet absorbance detection. Journal of Chromatography B 2002; 773: 191–197.

21. Raggi MA, Casamenti G, Mandrioli R, et al. A sensitive high-performance liquid chromatographic method using electrochemical detection for the analysis of olanzapine and desmethylolanzapine in plasma of schizophrenic patients using a new solid-solid phase extraction procedure. Journal of Chromatography B; 2001; 750: 137–146.

22. Raggi MA, Casamenti G, Mandrioli R, et al. Determination of the novel antipsychotic drug olanzapine in human plasma using HPLC with amperometric detection. Chromatographia 2000; 51: 562–566.

23. Raggi MA, Mandrioli R, Sabbioni C, et al. Determination of olanzapine and desmethylolanzapine in the plasma of schizophrenic patients by means of an improved HPLC method with amperometric detection. Chromatographia 2001; 54: 203–207.

24. Saracino MA, Koukopoulos A, Sani G, et al. Simultaneous high-performance liquid chromatographic determination of olanzapine and lamotrigine in plasma of bipolar patients", Therapeutic Drug Monitoring 2007; 29: 773–780.

25. Eap CB, Veuthey JL, Guillarme D, et al. Therapeutic drug monitoring of seven psychotropic drugs and four metabolites in human plasma by HPLC-MS. Journal of Pharmaceutical and Biomedical Analysis 2009; 50: 1000–1008.

26. Josefsson M, Roman M, Skogh E, et al. Liquid chromatography/tandem mass spectrometry method for determination of olanzapine and N-desmethylolanzapine in human serum and cerebrospinal fluid. Journal of Pharmaceutical and Biomedical Analysis 2010; 53: 576–582.

27. Saracino MA, Gandolfi O, Dall'Olio RO, et al. Determination of olanzapine in rat brain using liquid chromatography with coulometric detection and a rapid solid-phase extraction procedure. Journal of Chromatography A 2006; 1122: 21–27.

28. Kasper SC, Mattiuz EL, Swanson SP, et al. Determination of olanzapine in human breast milk by high-performance liquid chromatography. Journal of Chromatography B 1999; 726: 203–209.

29. Xia X, Tao Z. Determination of olanzapine and its tablets by HPLC. Chinese Journal of Pharmaceuticals 2004; 35: 46–48.

30. Pathak A, Rajput SJ. Development of stability-indicating hplc method for simultaneous determination of olanzapine and fluoxetine in combined dosage forms. Journal of Chromatographic Sciences 2009; 47: 605–611.

31. Reddy BV, Suresh Reddy KVN, Sreeramulu J, et al. Simultaneous determination of olanzapine and fluoxetine by HPLC. Chromatographia 2007; 66: 111–114.

32. Shah CR, Shah NJ, Suagia BN, et al. Simultaneous assay of olanzapine and fluoxetine in tablets by column high-performance liquid chromatography and high-performance thin-layer chromatography. Journal of AOAC International 2007; 90: 1573–1578.

33. Hiriyanna SG, Basavaiah K, Goud PSK, et al. Identification and characterization of olanzapine degradation products under oxidative stress conditions. Acta Chromatographica 2008; 20: 81–93.

34. Ensafi A, Allafchian AR. Novel and selective potentiometric membrane sensor for amiloride determination in pharmaceutical compounds and urine. Journal of Pharmaceutical and Biomedical Analysis 2008; 47(4-5): 802–806.

35. Kanberoglu GS, Coldur F, Topcu C, et al. A Flow−injection potentiometric system for selective and sensitive determination of serum lithium level. IEEE Sensors Journal 2015; 15(11): 6199–6207.

36. AlRabiah H, Al-Majed A, Abounassif M, et al. Two novel potentiometric sensors for determination of clonidine in some pharmaceutical formulation. International Journal of Electrochemical Science 2016; 11: 6761–6774.

37. Ganjali MR, Karimi S, Shahtaheri SJ, et al. Determination of clonidine by potentiometry using PVC membrane electrode. International Journal of Electrochemical Science 2013; 8: 1999–2008.

38. Del Valle EM. Cyclodextrin and their uses a review. Process Biochemistry 2004; 39: 1033–1046.

39. Hedges AR. Industrial applications of cyclodextrins. Chemical Reviews 1998; 98: 2035–2044.

40. Yang R, Li K, Wang K, et al. Porphyrin assembly on β-cyclodextrin for selective sensing and detection of a zinc ion based on the dual emission fluorescence ratio. Analytical Chemistry 2003; 75: 612–621.

41. El-Kosasy AM, Nebsen M, El-Rahman MKA, et al. Comparative study of 2-hydroxy propyl beta cyclodextrin and calixarene as ionophores in potentiometric ion-selective electrodes for neostigmi-

ne bromide. Talanta 2011; 85(2): 913–918.

42. Trojanowicz M. Enantioselective electrochemical sensors and biosensors: A mini-review. Electrochemistry Communications 2014; 38: 47–52.

43. Patil SR, Turmine M, Peyre V, *et al*. Study of β-cyclodextrin/fluorinated trimethyl ammonium bromide surfactant inclusion complex by fluorinated surfactant ion selective electrode. Talanta 2007; 74: 72–77.

44. El-Kosasy AM. Determination of hydroxyurea in capsules and biological fluids by ion-selective potentiometry and fluorimetry. Journal of AOAC International 2003; 86: 15–21.

45. Ozoemena KI, Stefan RI. Enantioselective potentiometric membrane electrodes based on alpha-, beta- and gamma-cyclodextrins as chiral selectors for the assay of L-proline. Talanta 2005; 66: 501–504.

46. IUPAC Analytical Chemistry Division. Recommendation for Nomenclature of Ion Selective Electrode. Pure and Applied Chemistry 1994; 66: 2527–2536.

47. IUPAC Analytical Chemistry Division. Potentiometric selectivity coefficients of ion selective electrodes. Pure and Applied Chemistry 2000; 72: 1851–2082.

Oʀɪɢɪɴᴀʟ ʀᴇsᴇᴀʀᴄʜ Aʀᴛɪᴄʟᴇ

In situ synthesis of PANI/CuO nanocomposites for non-enzymatic electrochemical glucose sensing

Gul Rahman*, Mustifuz Ur Rahman, Zainab Najaf

Institute of Chemical Sciences, University of Peshawar, Peshawar 25120, Pakistan. E-mail: gul_rahman47@uop.edu.p pk

ABSTRACT

We report the in situ synthesis of polyaniline/copper oxide (PANI/CuO) nanocomposites and their characterization as electrocatalyst for non-enzymatic electrochemical glucose detection. Copper oxide (CuO) nanoparticles were prepared by wet chemical precipitation method followed by thermal treatment while the composites of PANI and CuO were synthesized by in situ chemical polymerization of aniline with definite amount of CuO. X-ray diffraction (XRD) results revealed that the composites are predominantly amorphous. The composite formation was confirmed by fourier transform infrared (FTIR) and UV-Vis spectroscopy analysis. The surface morphology was greatly altered with the amount of CuO in composite structure. PANI/CuO nanocomposites were coated on copper substrate to investigate their electrocatalytic activity for glucose sensing. PANI/CuO with 10 wt. % CuO exhibited good response towards electrochemical glucose oxidation.

Keywords: Polyaniline; Copper Oxide; Nanocomposites; Electrocatalyst; Glucose Sensing

1. Introduction

Diabetes mellitus, a chronic metabolic disorder, resulting from glucose concentrations lower or higher than the normal range (4.4–6.6 mM)[1]. The increasing number of diabetic patients has compelled scientists to search for fast and stable technologies to detect blood glucose level. The development of rapid, simple, effective, highly selective, biocompatible, easily portable, environment friendly and inexpensive glucose sensors are extremely desirable in several fields, including pharmaceutics, clinical diagnostics and food industry[2]. Enzyme-based electrodes using glucose oxidase (Gox), due to their selectivity and high sensitivity have been extensively used to design various amperometric biosensors for the detection of glucose[3]. Besides their potential applications in biosensing, enzyme-modified electrodes have a number of drawbacks, including inadequate thermal stability, high cost of enzymes, acute functioning environments and complex procedure of immobilization. Moreover, the environmental conditions such as humidity, pH value, ionic detergents, temperature and toxic chemicals can easily affect the catalytic activity of Gox[4,5].

Researchers are nowadays taking interest to develop simple enzyme-free glucose sensors with desirable properties of sensitivity, selectivity, environment friendly, stability, using simple organic and inorganic precursors. For this purpose, electrodes modified with pure metals[6,7], alloys[8,9], metal/metal oxide[10,11] and composites of conduc-

ting polymers with other materials[12,13] have been developed. However, the high cost of rare metals, poor sensitivity, narrow linear range and reduced selectivity to glucose, possibly due to the surface etching or poisoning during the electrochemical process that have limited their potential applications in biosensors[14]. Hence, the development of a highly sensitive, cheap and free of interference sensor for non-enzymatic monitoring of glucose is still critically required. The organic conducting and non-conducting polymers due to their facile synthesis and low cost are nowadays used for the preparation of a number of nonenzymatic biosensors. The polymer provides a matrix for immobilization of enzyme or inorganic catalyst having a three dimensional arrangement and have been used for the detection of carbohydrates in alkaline and neutral medium[15]. The conclusion derived from these studies showed that polymer based modified electrodes are advantageous due to ease of fabrication, wider linear response range, having good stability and low detection limits.

Recently, PANI has drawn considerable interest due to their unique conducting properties and has been largely applied in biosensing owing to its distinctive and controllable electrochemical characteristics[16], its environmental[17], thermal[18] and electrochemical stability[19] as well as interesting electro-optical properties[20]. Additionally, PANI is known to have comprehensive tunable properties originating from its structural flexibility which ultimately leads to many applications in the fields of anti-corrosive coatings, energy storage systems and gas sensing[21]. Conversely, copper oxide, a P-type semiconductor, is of particular interest in various applications including catalysis[22], semiconductors[23] gas sensors[24], biosensors[25], and field transistors[26] due to narrow band gap (1.2 eV), high specific surface area, good thermal conductivity, good electrochemical activity, antibiotic properties and photovoltaic properties[27]. The presence of CuO nanoparticles as impurities in carbon nanotubes based electrodes has been confirmed to be responsible for the electroxidation of glucose[28]. A glucose sensor fabricated by electrodepositing copper oxide nanocubes on graphene has shown good activity[29]. Furthermore, CuO/Cu(OH)$_2$ nanoparticles deposited on graphite-like carbon films exhib-

ited greater sensitivity and stability for sensing of glucose[30]. These studies suggest the importance of supporting material of CuO nanoparticles for its enhanced glucose sensing performance.

In the present work, PANI/CuO nanocomposites were prepared by in situ chemical polymerization of aniline and CuO nanoparticles and their activity was tested for non-enzymatic electrochemical glucose sensing. Various physicochemical and spectroscopic techniques were used to characterize the synthesized PANI/CuO nanocomposites. PANI/CuO nanocomposites were coated on copper substrate to make electrode for glucose detection. The results revealed that our synthesized PANI/CuO nanocomposites can be used as electrocatalysts for glucose detection and related applications.

2. Experimental

2.1 Reagents

All the reagents were of analytical grade and used without further purification except aniline which was distilled repeatedly for every experiment. Aniline, sodium hydroxide and ammonium persulphate were purchased from Merck (E. Merck, D-6100, Darmstadt, FR. Germany). Hydrochloric acid, copper acetate, acetic acid, and absolute ethanol were purchased from BDH London.

2.2 Synthesis of CuO nanoparticles

CuO nanoparticles were synthesized by wet chemical precipitation method. A 0.4 M solution of copper acetate was prepared, with 3 ml acetic acid added. Then the resulting solution was heated in boiling water bath for half an hour with constant stirring in a magnetic stirrer followed by the rapid addition of 30 ml concentrated solution of NaOH (6 m) to the boiling mixture. After the addition of NaOH, the blue solution immediately turned black. The solution was further stirred for 3 h, keeping the temperature at 100 °C. The final product was centrifuged and washed several times with deionized water and absolute ethanol, respectively. The black colored copper oxide nanoparticles were first dried in air for 18 h and then in an oven at 80 °C for 3 h and then stored in an air tight bottle.

2.3 Synthesis of PANI

Polyaniline was prepared via oxidative chemical polymerization method using hydrochloric acid as dopant and ammonium persulphate as oxidant. A 100 ml hydrochloric acid solution (0.2 m) was prepared, with 1.9 ml aniline monomer added and stirred at 0 °C in an ice bath for 10 minutes. Then a precooled ammonium persulphate solution (0.2 m) was added dropwise for half an hour with constant stirring at 0 °C. The solution was further stirred for 6 h in an ice bath by magnetic stirrer and then kept in a refrigerator for 18 h at 0 °C. The final product was filtered and washed with distilled water and ethanol respectively many times. After washing, the resultant polymer was dried in an oven at 80 °C for 6 h and stored in airtight bottle.

2.4 Synthesis of PANI/ CuO nanocomposites

Different percent composition of PANI/CuO nanocomposite were prepared by in situ chemical polymerization method using hydrochloric acid as dopant and ammonium persulphate as oxidant. A 100 ml hydrochloric acid solution (0.2 m) was taken to which aniline monomer was added and stirred at 0 °C for 10 minutes. Then a known weight of CuO nanoparticles was added to the aniline monomer solution and stirred for half an hour in an ice bath. Then 50 ml ammonium persulphate solution was added dropwise for 30 minutes keeping the temperature at 0 °C with constant stirring. The solution was further stirred at the same temperature for 6 h and then placed in a refrigerator for 18 h at 0 °C. The final product was washed with water and absolute ethanol respectively several times and then dried in an oven at 80 °C for 6 h. In this way, five different composites of PANI with 10%, 20%, 30% 40% and 50% (weight %) of CuO were prepared.

2.5 Fabrication of glucose sensor

PANI/CuO nanocomposites were coated on copper substrate. Prior to deposition, the substrate was cleaned with detergent, followed by ultrasonicationin distilled water, absolute ethanol and acetone for 20 minutes each, respectively. The substrates were then dried in an oven at 80 °C for 1 h.

The composites were deposited on copper by drop casting method. For this purpose, a small amount of the composite was dissolved in N-methylpyrrolidone and sonicated for 15 min. A few drops of the solution were drop casted onto the surface of copper that covered the surface completely. This step was followed by drying the electrode at 80 °C for 2 h and stored in air tight bottles before use.

2.6 Characterization

The surface morphology of PANI/CuO nanocomposites was characterized using scanning electron (JEOL, JAPAN, Model: JSM 5910). The XRD spectra were acquired by using XRD; JEOL-JDX: 3532) with Kα radiations (λ= 1.5406 Å). The spectra were obtained by scanning the samples from 5°−80° with a sampling pitch of 0.05° and step time of 1 s.The UV-Vis spectra were obtained from UV/Vis Perkin Elmer (spectrophotometer; UK), while FTIR was carried out using FTIR model Shimadzu, IR Prestige-21& FTIR 8400S. Cyclic voltammetry (CV) measurements were performed in an electrochemical cell consisting on working electrode, graphite counter electrode and (Ag/AgCl) as reference electrode coupled with a potentiostat (Gamry: USA, ZRA potentiostat ref 3000).

3. Results and discussion

3.1 XRD studies

Figure 1 (A) represents the XRD pattern of CuO nanoparticles. Well distinguished sharp peaks are observed at 2θ equal to 35° and 38°, while small peaks in the region 32°, 48°, 61° and 65°. All these XRD signals correspond to the CuO phase and consistent with the literature[31]. The average crystallite size of copper oxide nanoparticles was calculated by Debye-Scherrer equation:

$$D = K\lambda/\beta Cos\theta$$

Where, D is the average crystallite size, λ is the wavelength of X-rays, β is the full width half maximum of the peak and θ is the angular position of the peak. The average crystallite size was found to be equal to 49.19 nm. **Figure 1 (B)** represents the XRD pattern for synthesized PANI. The analysis of the XRD pattern reveals that there are no sharp peaks suggesting an amorphous phase for the prepared PANI. Furthermore, the XRD patterns of PANI/CuO nanocomposites, i.e., 10%, 20%, 30%,

40% and 50% shown in **Figure 1 (C-G)** suggest an amorphous phase for nanocomposites similar to that of the pure PANI.
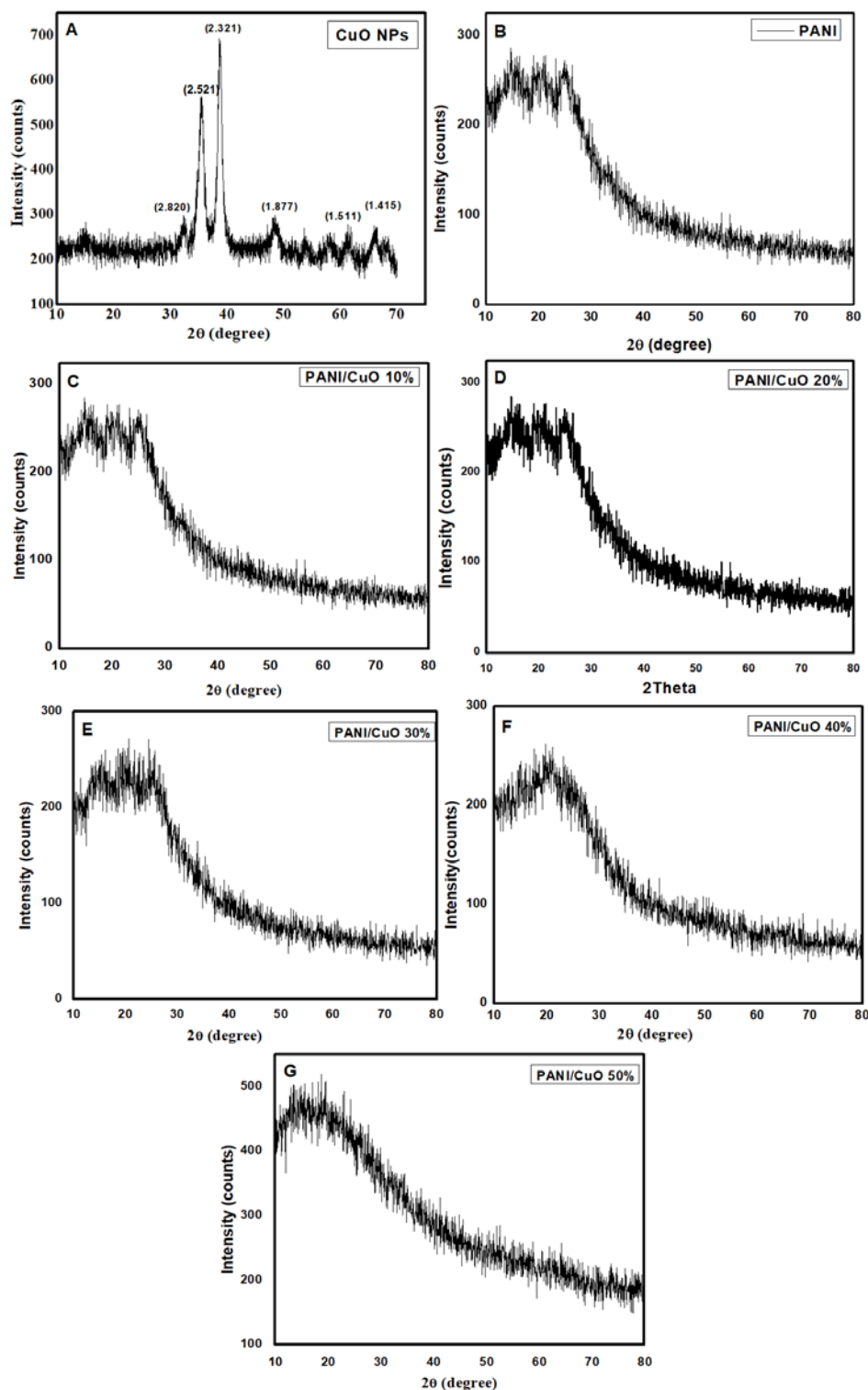
Figure 1. XRD patterns of **(A)** CuO nanoparticles; **(B)** PANI and different composition of PANI/CuO nanocomposite; **(C)** 10%; **(D)** 20%; **(E)** 30%; **(F)** 40%; **(G)** 50%.

3.2 FTIR analysis

FTIR spectra of CuO nanoparticles are shown in **Figure 2 (A)**, the bands at 525 cm^{-1} to 750 cm^{-1} are assigned to the vibrations of the CuO functional group. The bands at the region 1404 cm^{-1} is due to the presence of carboxylate ions bound to CuO nanoparticles as bidentate ligand[32]. The band at 1639 cm^{-1} might be due to the formation of covalent bond between CuO nanoparticles and the –OH group

12

from adsorbed water.
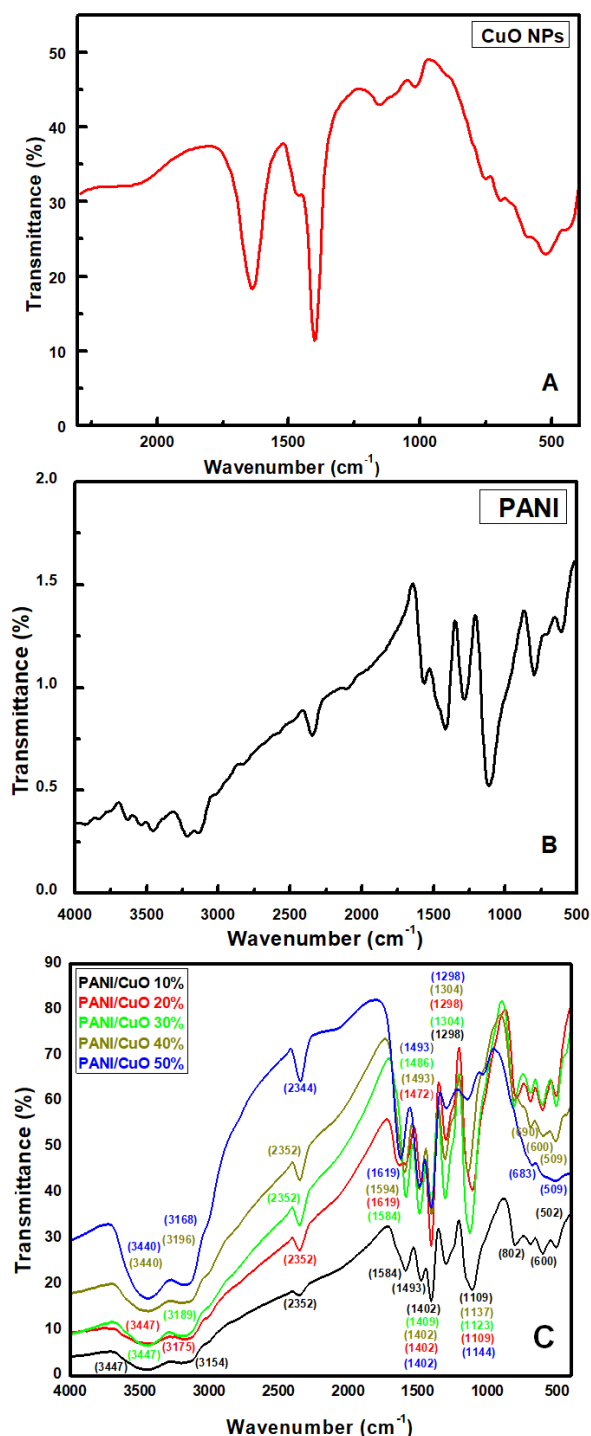
Figure 2. FTIR spectra of (A) CuO nanoparticles, (B) PANI, and (C) different percent composition of PANI/CuO nanocomposites.

The FTIR spectra of PANI and PANI/CuO nanocomposites are presented in **Figure 2 (B)** and **(C)**, respectively. The bands at 1569 cm^{-1} and 1426 cm^{-1} are assigned to the stretching mode of vibration of C = C and C = N of quinonoid and benzinoid units of PANI. The band at 1114 cm^{-1} is due to in plane bending vibrations of =C-H mode. The peak at 1283 cm^{-1} is assigned to C-N stretching vibration of benzenoid moiety of PANI. The peaks arise between values of 3216-3453 cm^{-1} is the result of N-H stretching vibration. The band at 788 cm^{-1} is due to out of plane bending vibration of =C-H. The FTIR spectra of nanocomposites are identical in shape with that of pure PANI with a slight red shift. The band at 1426 cm^{-1} is shifted to 1493 cm^{-1} in case of 10%, 40% and 50% nanocomposites, while the same band is shifted to 1486 cm^{-1} and 1472 cm^{-1} in case of 20% and 30% nanocomposites, respectively. The band at 1569 cm^{-1} is shifted to 1584, 1619, 1584, 1594 and 1619 cm^{-1} in case of 10, 20, 30, 40 and 50% nanocomposites, respectively. Moreover, there is band shifting from 1114 cm^{-1} to 1137, 1123, 1144, 1109 and 1109 cm^{-1} in case of 40, 20, 30, 10 and 50% nanocomposites, respectively. The band at 3216 cm^{-1} is shifted to lower wavenumber in all nanocomposites. All the above mentioned changes in the spectra reveal that there is some sort of interaction between PANI and CuO nanoparticles. This change has been attributed to the change in molecular order and slight loss of conjugation in PANI, resulting in strong localization of electrons over PANI ring[33].

3.3 UV-Vis spectroscopy

The UV-Vis spectra of CuO nanoparticles were obtained using water as solvent, while the UV-Vis spectra of PANI and all nano-composites were recorded using N-methylpyrrolidine as solvent. The UV-Vis spectra of CuO nanoparticles show a broad absorption peak at 290 nm, while that of PANI as shown in **Figure 3 (A)** has two distinctive broad bands at 330 nm and 641 nm. The spectra are identical to previous work in literature[34,35]. The band at 330 nm is attributed to π-π* transition of benzenoid ring, while the band at 640 nm is assigned to π-π* transition of quinoid ring of PANI.

The UV-Vis spectra of nanocomposites are shown in **Figure 3 (C)**. The general shape of the curve is similar to PANI and the shift in absorption band is obvious. The band at 330 nm in PANI is shifted to higher wavelengths in the composite material, i.e., from 330 nm to 326, 325, 320, 314 and 290 nm in 10, 20, 30, 40 and 50% nanocomposites, respectively. The shift in the band at 642 nm

13

is even much pronounced, i.e., from 642 nm to 639, 623, 622, 602 and 590 nm in 10, 20, 30, 40 and 50% nanocomposites, respectively.
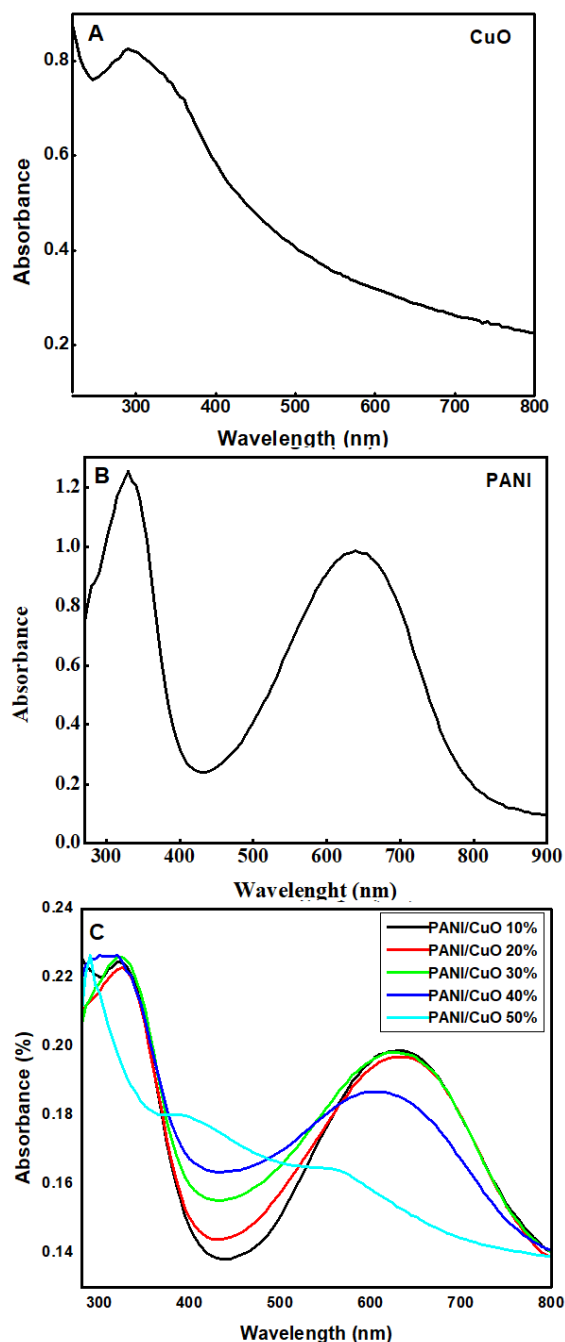
Figure 3. UV-Vis spectra of (A) Copper oxide, (B) PANI, and (C) different percent composition of PANI/CuO nanocomposites.

3.4 Morphology of PANI/CuO

Figure 4 (A) shows the SEM image of pure CuO nanoparticles. From the image, we can see the surface morphology of the finely dispersed nanoparticles.

The average particle size of the CuO nanoparticles was found to be 55.25 nm. As can be seen

from the SEM image, the particles are fine, homogenous and granular. Surface morphology of the prepared PANI is shown in **Figure 4 (B)** which shows that PANI has a highly porous structure. One can easily conclude from the image that it has a high surface area. Moreover, fussy surface morphology with interconnected fibers can also be seen from the image. The SEM images of the nanocomposites shown in **Figure 4 (C-G)** reveal that the incorporation of nanoparticles into PANI has a significant effect on its morphology.
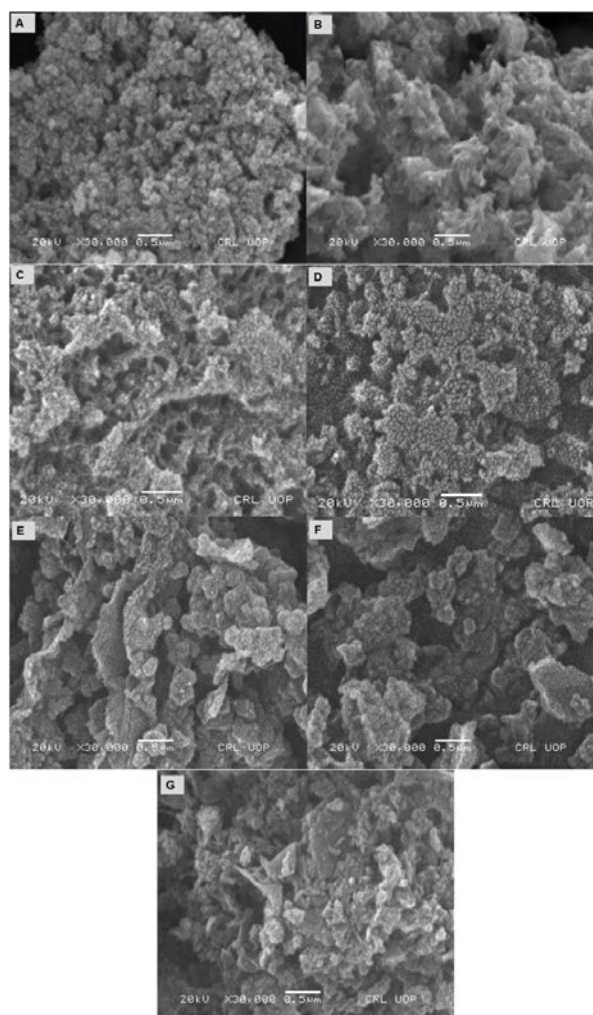
Figure 4. SEM images of **(A)** copper oxide nanoparticles, **(B)** PANI, and **(C-G)** different percent composition of PANI /CuO nanocomposites with 10%, 20%, 30%, 40% and 50% CuO, respectively.

From the **Figure 4 (C)** PANI/CuO 10%, it can be seen that the finely dispersed nanoparticles are loaded into PANI fibers, resulting a decrease in porosity. The image also suggests that there are no bare or free nanoparticles and all the nanoparticles are incorporated by the polymer uniformly. Thus, it can be concluded that this method can be

14

used to prepare uniformly dispersed layer of nano-particles. The SEM image of PANI/CuO 20% in **Figure 4** (D) shows that the increase in weight of nanoparticles has further decreased the porosity and the particles are now more tightly packed. Furthermore, the SEM images of composites with percent composition of 30, 40 and 50% shown in **Figure 4 (E-G)** are further closely packed as compared with 20% loading of nanoparticles. The nanoparticles have been homogenously incorporated into the polymer matrix.

3.5 Electrochemical glucose sensing

Figure 5 represents the cyclic voltammetry of PANI/CuO (10%) in the absence and presence of glucose in 0.1 M NaOH solution. In the absence of glucose, there is no distinguished peak as can be seen in the figure. When glucose is added into solution, there is a well distinguished peak around 0.65 V corresponding to irreversible oxidation of glucose. Further, the current density of the peak is proportional to the concentration of glucose in solution during cyclic voltammetry. The peak current improved over the potential range of 0.4 to 0.65 V following addition of 4-10 mM of glucose.
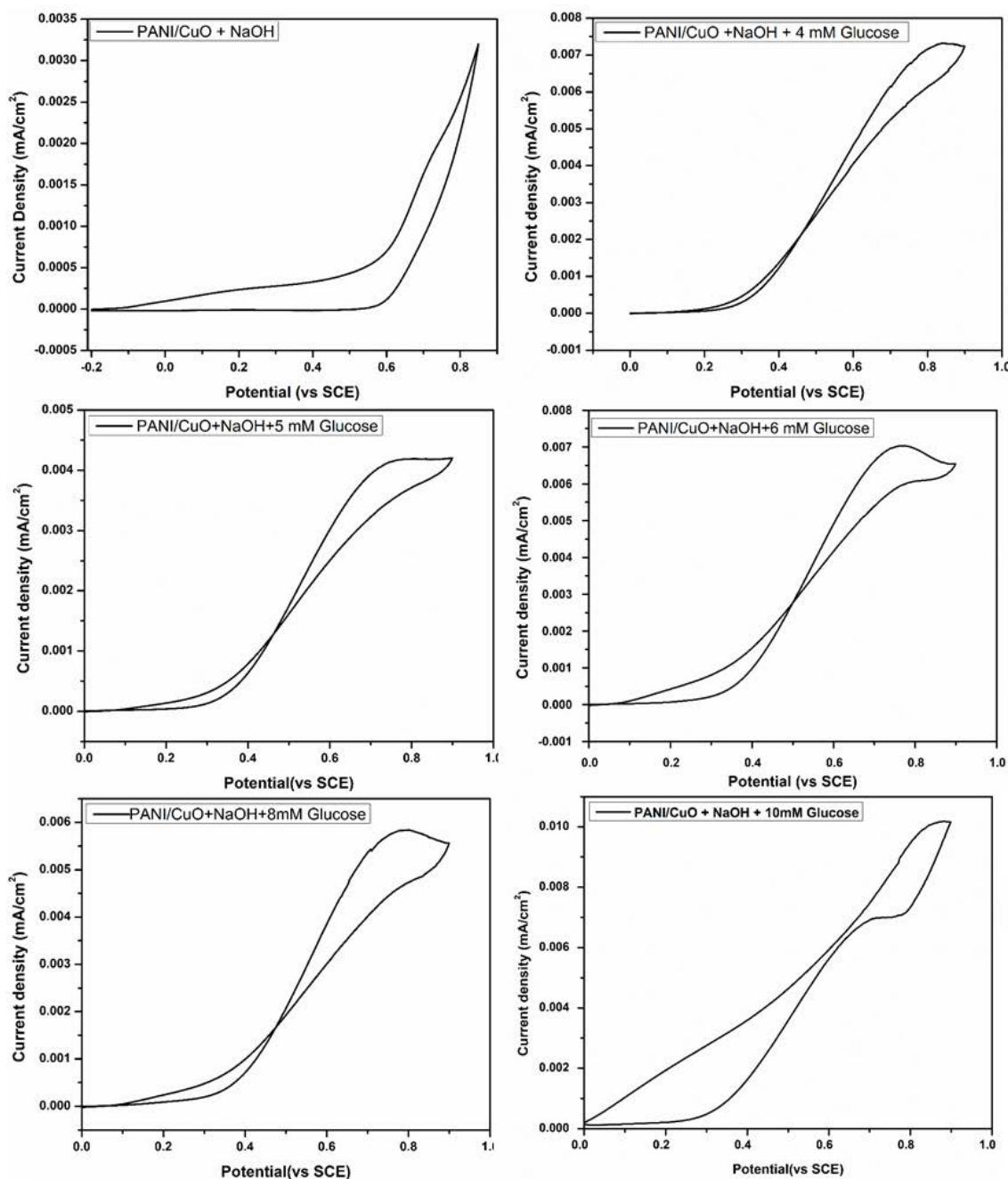
Figure 5. Cyclic voltammograms of PANI/CuO (10%) in NaOH solution in the absence and presence of various glucose concentrations.

15

4. Conclusion

In summary, PANI/CuO nanocomposites have been successfully synthesized by in situ chemical polymerization of aniline and CuO nanoparticles. The synthesized samples were characterized by various techniques, including XRD, SEM, UV-Vis spectroscopy, FTIR, and cyclic voltammetry. With the addition of CuO nanoparticles into the matrix of PANI, the crystallinity remained unchanged while the UV-Vis absorption properties altered drastically. In addition, the surface morphology varied with CuO composition in the composites. When tested for electrochemical detection of glucose, the PANI/CuO (10 %) electrode exhibited good response, thus indicating its potential as electrocatalyst for electrochemical glucose sensing applications.

Conflict of interest

The authors declare that they have no conflict of interest.

Acknowledgements

References

1. Wang G, He X, Wang L, *et al*. Non-enzymatic electrochemical sensing of glucose. Microchimica Acta 2013; 180(3-4): 161–186.
2. Newman JD, Turner AP. Home blood glucose biosensors: A commercial perspective. Biosensors & Bioelectronics 2005; 20(12): 2435–2453.
3. Deng C, Chen J, Chen X, *et al*. Direct electrochemistry of glucose oxidase and biosensing for glucose based on boron-doped carbon nanotubes modified electrode. Biosensors & Bioelectronics 2008; 23(8): 1272–1277.
4. Wilson R, Turner APF. Glucose oxidase: an ideal enzyme. Biosensors & Bioelectronics 1992; 7(3): 165–185.
5. Kang X, Mai Z, Zou X, *et al*. A novel glucose biosensor based on immobilization of glucose oxidase in chitosan on a glassy carbon electrode modified with gold–platinum alloy nanoparticles/multiwall carbon nanotubes. Analytical biochemistry 2007; 369(1):71–79.
6. Li L, Zhang W. Preparation of carbon nanotubes supported platinum nanoparticles by an organic colloidal process for nonenzymatic glucose sensing. Microchimica Acta 2008; 163(3-4): 305–311.
7. Li Y, Song Y, Yang C, *et al*. Hydrogen bubble dynamic template synthesis of porous gold for nonenzymatic electrochemical detection of glucose. Electrochemistry Communications 2007; 9(5): 981–988.
8. Wang J, Thomas DF, Chen A. Nonenzymatic electrochemical glucose sensor based on nanoporous PtPb networks. Analytical Chemistry 2008; 80(4): 997–1004.
9. Chen X, Pan H, Liu H, *et al*. Nonenzymatic glucose sensor based on flower-shaped Au@ Pd core–shell nanoparticles–ionic liquids composite film modified glassy carbon electrodes. Electrochimica Acta 2010; 56(2): 636–643.
10. Sattar M, Conway B. Electrochemistry of the nickel-oxide electrode—VI. Surface oxidation of nickel anodes in alkaline solution. Electrochimica Acta 1969; 14(8): 695–710.
11. Wang J, Zhang W. Fabrication of CuO nanoplatelets for highly sensitive enzyme-free determination of glucose. Electrochimica Acta 2011; 56(22): 7510–7516.
12. Chowdhury AD, Gangopadhyay R, De A. Highly sensitive electrochemical biosensor for glucose, DNA and protein using gold-polyaniline nanocomposites as a common matrix. Sensors and Actuators B: Chemical 2014; 190: 348–356.
13. Yavuz AG, Uygun A, Bhethanabotla VR. Preparation of substituted polyaniline/chitosan composites by in situ electropolymerization and their application to glucose sensing. Carbohydrate Polymers 2010; 81(3): 712–719.
14. Luo J, Jiang S, Zhang H, *et al*. A novel non-enzymatic glucose sensor based on Cu nanoparticle modified graphene sheets electrode. Analytica Chimica Acta 2012; 709: 47–53.
15. Adeloju S, Wallace G. Conducting polymers and the bioanalytical sciences: new tools for biomolecular communications. A review. Analyst 1996; 121(6): 699–703.
16. Kang Y, Kim SK, Lee C. Doping of polyaniline by thermal acid–base exchange reaction. Materials Science and Engineering: C 2004; 24(1-2): 39–41.
17. Pruneanu S, Veress E, Marian I, *et al*. Characterization of polyaniline by cyclic voltammetry and UV-Vis absorption spectroscopy. Journal of Materials Science 1999; 34(11): 2733–2739.
18. Wang X, Geng Y, Wang L, *et al*. Thermal behaviors of doped polyaniline. Synthetic Metals 1995; 69(1-3): 265–266.
19. Chiang JC, MacDiarmid AG. 'Polyaniline': protonic acid doping of the emeraldine form to the metallic regime. Synthetic Metals 1986; 13(1-3): 193–205.
20. Malile B. Exploring the potential of polyelectrolyte-aptamer films for use in optical and electrochemical sensing [Master's thesis]. York University: York University; 2015. p. 72.
21. Dhand C, Das M, Datta M, *et al*. Recent advances

in polyaniline based biosensors. Biosensors & Bioelectronics 2011; 26(6): 2811–2821.

22. Chen J, Deng S, Xu N, *et al*. Temperature dependence of field emission from cupric oxide nanobelt films. Applied Physics Letters 2003; 83(4): 746–748.

23. Meyer B, Polity A, Reppin D, *et al*. Binary copper oxide semiconductors: From materials towards devices. Physica Status Solidi B 2012; 249(8): 1487–1509.

24. Chowdhuri A, Gupta V, Sreenivas K, *et al*. Response speed of SnO_2-based H_2S gas sensors with CuO nanoparticles. Applied Physics Letters 2004; 84(7): 1180–1182.

25. Luque GL, Rodríguez MC, Rivas GA. Glucose biosensors based on the immobilization of copper oxide and glucose oxidase within a carbon paste matrix. Talanta 2005; 66(2): 467–471.

26. Zheng X, Xu C, Tomokiyo Y, *et al*. Observation of charge stripes in cupric oxide. Physical Review Letters 2000; 85(24): 5170–3.

27. Rai V, Jamuna B. Science against microbial pathogens: Communicating current research and technological advances. In: Mendez-Vilas A(editor). Karnataka, India: University of Mysore; 2011. p. 197.

28. Batchelor-McAuley C, Wildgoose GG, Compton RG, *et al*. Copper oxide nanoparticle impurities are responsible for the electroanalytical detection of glucose seen using multiwalled carbon nanotubes. Sensors and Actuators B: Chemical 2008; 132(1): 356–360.

29. Luo L, Zhu L, Wang Z. Nonenzymatic amperometric determination of glucose by CuO nanocubes–graphene nanocomposite modified electrode. Bioelectrochemistry 2012; 88: 156–163.

30. You T, Niwa O, Tomita M, *et al*. Characterization and electrochemical properties of highly dispersed copper oxide/hydroxide nanoparticles in graphite-like carbon films prepared by RF sputtering method. Electrochemistry Communications 2002; 4(5): 468–471.

31. Manjunath A, Irfan M, Anushree KP, *et al*. Synthesis and Characterization of CuO Nanoparticles and CuO Doped PVA Nanocomposites. Advances in Materials Physics and Chemistry 2016; 6(10): 263.

32. Taman R, Salem M, Ossman M, *et al*. Metal oxide nano-particles as an adsorbent for removal of heavy metals. Journal of Advanced Chemical Engineering 2015; 5(3): 1–8.

33. Jundale D, Navale ST, Khuspe GD, *et al*. Polyaniline–CuO hybrid nanocomposites: synthesis, structural, morphological, optical and electrical transport studies. Journal of Materials Science: Materials in Electronics 2013; 24(9): 3526–3535.

34. Kumar A, Kumar D, Pandey G. Characterisation of hydrothermally synthesised CuO nanoparticles at different pH. Journal of Technological Advances and Scientific Research 2016; 2(4): 166–169.

35. Godovsky DY, Varfolomeev AE, Zaretsky DF, *et al*. Preparation of nanocomposites of polyaniline and inorganic semiconductors. Journal of Materials Chemistry 2001; 11(10): 2465–2469.

ORIGINAL RESEARCH ARTICLE

Mixed mode oscillations in an electrochemical reactor

Zdzislaw Trzaska[*]

University of Ecology and Management, Warsaw 00-792, Poland. E-mail: zdzislawtrz@gmail.com

ABSTRACT

This paper subject focuses on modelling of electrochemical processes during a deposition of nanostructured materials on a metallic substrate. Fundamentals of electrocrystallization processes and parameters influenced the final quality of the resulting products are considered. To quantify the evolution of the electrochemical reactor processes with respect to time, an equivalent electric circuit has been established. Two types of periodic supplying currents were taken into consideration: bipolar pulse current and sinusoidal rectified current. Results of performed computer simulations of electrocrystallization processes with the focus on mixed mode oscillations (MMOs) as the dynamical switches between small amplitude oscillations (SAOs) and large amplitude oscillations (LAOs) are presented. The established circuit model can lead to methods for fast treating large quantities of electrocrystallizator data and extracting from them kinetic parameters importantly influenced the structure of the produced materials.

Keywords: Electrochemical Reactor; Redox Reactions; Mathematical Model; Circuit Model; Mixed Mode Oscillations

ARTICLE INFO

COPYRIGHT

1. Introduction

During the last twenty years, electrochemical processes have become the basis for techniques comprehensively, being relevant for the production of nanostructured materials or nanostructured surface layers, which are widely applied in many industries that use the top technologies. This has a bearing mainly to such industries as the aerospace, automotive, military, microelectronics, computers, energy, biotechnology and related others. Presently, challenges in relations to electrochemical processes used in the practice are becoming more and more expressive in terms of better adapting them to the special technological requirements with meeting the directives for reducing negative impact on the surrounding environment. It should be emphasized that electrochemical methods are receiving recently increasing attention in rapidly growing fields of science and technology, mainly in such domains as nanosciences (nanoelectrochemistry) and life sciences (organic and biological electrochemistry). Electrochemical processes not only represent interesting cases of phase formation and crystal growth, but are also powerful methods for various technological applications, because the driving force of the process can be easily controlled by the current density, the electrodes potential and composition of the bath solution. Characterization, modification, and understanding of various electrochemical interfaces or electrochemical processes at the nanoscale have led to a huge increase of scientific interest in electrochemical mechanisms as well as in application of electrochemical methods to novel technologies. It is worth pointing out that nowadays

nanomaterials are extensively used as important development factor in the fields of porous semiconductor, deposition into templates, electro-deposition of multilayers and superlattices, as well as self-organized growth of transition metal oxide nanotubes and to modify sensor surfaces, giving improved analytical characteristics[1]. The electro-crystallization method is exceptionally suitable for preparations of specific materials, mainly the protective layers, and in the near future, may be more effective than previously involved methods in surface modification technologies of known materials, as well as newly produced materials. These layers can be used together with their substrates or as separated from them.

It is well-known that an efficient way to produce nanocrystalline materials is the application of an electrochemical method based on electrocrystallization processes generated as a result of oxidation and reduction reactions which occur at the electrodes: anode and cathode, respectively, in accord to the relations:

$$Me^{ne+} \underset{(Oxidation)\ -ne^-}{\overset{+ne^-\ (Reduction)}{\rightleftharpoons}} Me \qquad (1)$$
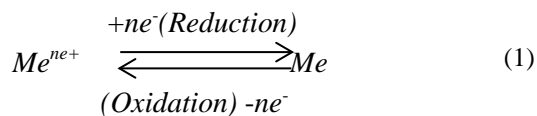
Oxidation-reduction reactions also known as redox reactions that describe all chemical processes in which there is a net change in atomic charge. In balanced redox reactions, the number of electrons lost by the reducing agent equals the number of electrons gained by the oxidizing agent. Electrocrystallizations are normally associated with a growth process where the nuclei formed on the electrode surface are highly dependent on the supplied current.

Taking into account the specificity of electrochemically produced materials, it is possible the formation of such structures of materials and their properties cannot be obtained by other technologies. The possibility of conscious control of the structures in the nanometric scale leads up to producing the useful materials with new properties and overcome previously insurmountable barriers to the development of technology. Nanomaterials possess at least one dimension sized from 1 to 100 nm[4,6] and not only unique geometric, mechanical,

electronic and chemical properties, but also properties different from macroscopic materials, such as quantum effect, surface effect, small size effect, etc. These properties have greatly prompted a broad range of applications of nanomaterials in medicine, electronics, biotechnologies, environmental science, energy production and biosensors. The nanostructures of the electrochemically produced materials can lead to novel properties, and hence to novel applications of conventional materials as well as new commercial applications, among other things, the graphene[7]. Because of such products as, for instance, sunscreens, cosmetics, clothing, upholstery, paint, bodywork of vehicles, computer components use nanotechnologies, it is not strange at present as well as in near future that the nanotechnology will infiltrate consumer products holistically. For these, among other reasons, the progress in science and engineering at the nanoscale appears now as a critical factor for society's security, prosperity of the economy, and enhancement of the quality of life. However, this advantage carries a price: electrochemical interfaces are more complex, because they include the solvent and ions. This poses a great problem for the modelling of these interfaces, since it is generally impossible to treat all active particles at an equivalent level[2].

In surface engineering, the electrocrystallization method is used to improve the useful properties of the metal products by deposition of appropriate metal layers on their surfaces protecting them against corrosion and wear. Moreover, appropriate realizations of electrodepositions give beneficial possibilities to isolate the product from the harmful effects of the external environment.

Generally, the manufacturing of nanostructures is too complicated for proper theory, so this has been the domain of computer simulations. It is worth underline that in the simulations of electrochemical nanostructures, we have to deal with a few hundreds of thousands or even of millions of atoms. This leads into the mathematics of their governing nonlinear differential equations, e.g., simple stability with the dynamic structure necessary for a system to exhibit nonmonotonic behavior.

This paper aims at mapping new frontiers in

emerging and developing electrochemical areas in the domain of nanomaterials manufacturing and innovation. Section 2 is devoted to presentation of fundamentals of electrocrystallization processes and parameters, influenced the final quality of resulting products. In Section 3, essential problems concerning the electrocrystallization process modelling with taking into account all major processes accompanied of nanostructured products are presented. Section 4 is aimed on presentations of results of performed computer simulations of electrocrystallization processes with the focus on mixed mode oscillations. Conclusions and final remarks are presented in Section 5.

2. Concise characterization of electrocrystallization processes

A simplified scheme of appliances being widely applied as electrochemical reactors and automated wafer processing equipment is presented in **Figure 1**. Electrodes charged by supplying generator are able to carry out chemical reactions for realizations of electrocrystallization processes. Technological importance of electrocrystallization also known as electroplating is of great interests and is widely used for production of different functional and decorative coatings. Each application-specific type of electrodeposition processing systems with their own specific requirements has been produced up-to-date. The advantage of electrodeposition lies in: (*i*) the low temperatures involved; (*ii*) the ability to coat geometrically complex or non-line-of-sight surfaces of porous products; (*iii*) the ability to effective control the thickness, composition, and microstructure of the deposit; (*iv*) the possible improvement of the substrate/coating bond strength; (*v*) the possibility of producing nanocomposites and nanostructured multilayer materials, and (*vi*) the easy availability and low cost of equipment.

Figure 1. Stand diagram with an electrocrystallization reactor**.**

Depending on conditions of the process realization, it is possible to produce thin layer materials with particular properties that influence importantly not only on research and modern fabrication intensifications, but also on numerous domains of the top microelectronics and bio-materials technologies. A variety of materials meeting the features in the art can be designed by choosing the type and composition of the electrolyte solution, and the process parameters, such as type and density of the current, temperature, and time duration of the process. One of the methods of modifying the useful properties of the products is the deposition on their surface of appropriate metal layer by electrodeposition method. The properties of electrodeposited layers can be formed by suitable selection of the electrolyte solution composition and by current parameters control.

Figure 2 shows current waveforms which are most often used in practice to supply the reactor. The electrodeposition with pulse periodic current is able to produce layers with more uniform particle distribution and better surface morphology than those obtained applying the direct current. This is common activity on rough parts or when a bright

20

finish is required. In certain processes, the management of electrolyte chemical concentrations is critical to ensure consistent results.

In order to optimize the operation of the electrocrystallization reactor in a specific application, it is important to understand its strengths and limitations because the same reactor does not work equally well for all depositions of nanostructured materials. Matching of periods of the supplying current is the best approach. All major process studies concentrate currently around the PPSRC electrodeposition technology and the general metal finishing products.

By electrocrystallization method, a variety of metals, metal alloys, and composite materials can be prepared, especially, great potential resides in shaping the properties of composite materials. Composite materials prepared by this method, can be formed with a metal matrix and a disperse phase may be constituted by different materials such as, other metal (W, Cu, Ni), ceramics (Al_2O_3, Cr_2O_3, Si_3N_4), polymer (PFE), or carbon (graphite, nanotubes, fullerenes, graphene). The combination of two different materials that are disperse phase and matrix metal allows the control of produced material properties in a fairly wide range, which enables the formation of a final material, satisfying efficiently various functions in practice.
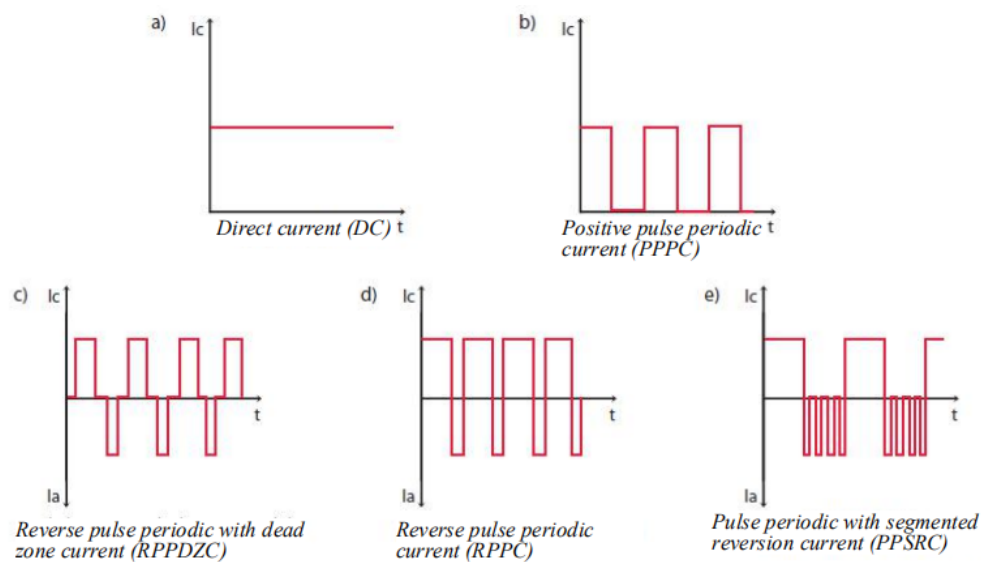
Figure 2. The time varying currents supplied to the electrocrystallization reactor.

The enormous potential for use in the development of new properties of the material lies in the possibility of conscious control of its structure at the nanometric scale. Presently, it is well-known that material properties, both mechanical, electrical, thermal and chemical are the results of the phenomena occurring in structures of nanometric size. Nanometric structure materials have particularly advantageous properties, and are an effective alternative to conventional materials.

To obtain a nanocrystalline structure, the deposition processes were carried out from a variety of electrolyte solutions. For instance, in the electrodeposition of nickel on a steel substrate, the electrolyte solution is usually composed of nickel(II) sulphate(VI), nickel chloride, boric acid and saccharin.

Prior to the deposition process of a surface layer, the substrate material is subjected to mechanical grinding, degreasing and activated to provide a good adhesion of the layer to the substrate. The process of electrocrystallization gives also possibilities to produce composite layers with nanocrystalline nickel matrix and dispersed phase in the form of graphene flakes[11].

Realization's efficiency of simultaneous deposition of metal and non-metallic disperse phase in the same process and the electrochemical reduction of the quality of the material will depend on such factors as: the nature and composition of the electrolyte solution, the process parameters (concentration, pH, temperature, stirring, current conditions), and the chemical nature of the grain

structure built in non-metallic disperse phase, chemical nature and content of various additives, as well as the quality of the substrate material and the quality of its surface. The low processing temperatures minimize crystallites interdiffusion, while the high selectivity of electrocrystallization process allows uniform modification of surfaces and structures with complicated profiles. All of these factors must be taken into account when designing a composite material, to be able properly (i.e., as expected) working under determined conditions. Such a large number of parameters, which affect the control of the electrocrystallization process and affect the quality of the manufactured material, provide, on the one hand, great flexibility in modifying the ability of the constitutive material, but on the other hand, provide a great challenge for appropriate and optimal selection. This requires a thorough diagnosis of the mechanisms of these complex processes, as well as their practical implementation of parameters. So, the set of the parameters of the implementation of such processes in the production environment and the relationships between these parameters and the structure and properties of the produced nanocrystalline material requires complex experimental research and in-depth analysis.

Taking into account potential applications of nano-crystalline materials, the pursuit of deposition uniformity, especially thickness uniformity, has been a technical imperative for suitable controlling every produced nanocrystalline material.

The most frequently studied electrocrystallization process is cathodic metal deposition on foreign and native substrates from electrolytes containing simple and/or complex metal ions[3,12]. Typical examples are the electrocrystallization of Ag from Ag^+ containing electrolytes[17], the cathodic deposition of Ag on n-Si from electrolytes containing $[Ag(CN)_2]^-$ ions[3], and the electrodeposition of $Cu^{[4]}$, which has recently becoming of significant technological importance for the fabrication of Cu interconnects on integrated circuit chips.

A process widely used for preparation of metallic alloys and semiconducting compounds is cathodic codeposition from multicomponent elec-trolytes[9]. Typical examples are the electrochemical formation of NiFe alloys by codeposition from Ni^{2+}- and Fe^{2+}- containing electrolytes and the electrodeposition of n-type CdTe from electrolytes containing Cd^{2+} and $HTeO^{2+}$ ions. Other important electrocrystallization processes are anodic deposition of metal oxides and anodic oxidation of metals and semiconductors. The first type of processes can be illustrated by the anodic deposition of PbO_2 from an aqueous Pb^{2+} solution. The second type are substrate consuming processes, which occur in aqueous solution and usually start with adsorption of OH^- ions and place exchange reactions with the substrate. Technologically important examples are the anodic oxidation of valve metals (Al, Nb, Ta, Ti) and $Si^{[2,9,10,17]}$.

This is much related to the principles of the so-called "green chemistry", where the use of low temperatures and mild conditions is specifically pursued in the synthesis of advanced materials.

Besides, the aforementioned ecological and economic benefits, the low-temperature processing has also opened the door to the incorporation of an increasing number of materials in technologically disruptive areas like flexible electronics and photovoltaic batteries[5].

Thin films of metal oxides are at the forefront of current and next-generation devices, where systems supported on low-cost, lightweight, and flexible substrates are expected to revolutionize the electronic industry by new applications, such as large-area displays, invulnerable sensors, smart textiles or electronic skin. Nowadays, the direct growth of metal oxide layers on low-melting-point flexible substrates (e.g. plastic, paper, or textile) is only possible at processing temperatures below the thermal degradation of the latter: around 350 °C in the most favourable case (i.e. polyimide foils). This constitutes a big challenge for the effective integration of multifunctional metal oxides since their crystallization temperatures (usually over 600 °C) are still several hundred degrees above the values that polymeric substrates can withstand. The strong electronic correlations imposed by the crystal lattice usually rule the behaviour of complex transition metal oxides. If crystallization is not achieved, most metal oxides lack of the physical property that

ultimately defines the functionality of the material. The processes leading to crystallization are in many ways governed by chemistry.

The demand ever increasing for low-cost and energy efficient manufacturing processes, together with the pressing need for new materials and devices in emerging technologies, are driving recent research efforts towards the near-room-temperature processing of metal oxide thin films using electrochemical methods.

3. The mathematical modelling of electrochemical reactors

To provide a foundation upon which we can derive an understanding of the matrix of mechanisms that affect the electrochemical deposition process and its variation a great help can be obtained by applying an effective tool of studies in the form of mathematical modelling. The modelling of the nucleation and material growth mechanism during the electrocrystallization process is extremely important due to its use in effective production of thin layers of pure metal or in the form of alloys and nanostructured composites with a high degree of precision. During the thin layer metal electrodeposition, the complex reactions of charge transfer with intermediate adsorption takes place at least in two elementary steps: reagent adsorption is the first and product desorption is the second. It has been observed especially in the case of multicomponent electrolytes that beside the electron diffusion and counter ion transport very often, hydrogen ions also participate in the charge transport and charge transfer processes in the course of redox transformation of these electrolytes, i.e. a model describing this case may be also essential. In general, models should allow us the activity to try and isolate the contribution of a few key parameters from the batch process in an attempt to predict the dominant effects as well as the variation of the process. Experimentation, particularly at the expensive pilot plant stage, can be minimized and development costs significantly reduced. Development of a reaction model is an essential first step to obtaining a reactor model, which in turn is a suitable tool for process optimizations. It has to be noted that the electrochemical deposition process appears as a competition between nucleation and grain growth of the produced materials. In charging and discharging of a pulse ion flux, especially for short pulses, the double layer of the interface between electrolyte and cathode distorts the pulse current[10], and affects the over potential response acting on the electrolyte.

To better control the coupled effects of pulsed current between the electrodes with its own magnetic field and improve electrochemical depositing performance, the combined effects must be studied. The electrochemical impedance spectroscopy experimental results show that both the reactor current frequency and magnetic flux density are significant factors in the performance of electrochemical reactors. The Lorentz force acting on the electrolyte in the double layer at the electrode increases with higher current densities improving electrolyte flow and conductivity, which enhances electrochemical deposition performance in terms of accuracy and surface finish.

Usually, the energy distribution of the charged particle flow is limited in a small region near the working electrode and is constrained by its own magnetic field. It should be emphasized that there are several mechanisms by which self-magnetic fields can be generated in the double layer right at the working electrode space in various regimes of the reactor excitation, including the density gradient term, the curl of the thermal force, the ponderomotive force, the inverse Faraday effect, and instabilities[5].

The azimuth magnetic field associated with the axial flow of a large current through a cylindrical symmetric electrolyte creates a magnetic pressure ($J{\times}B$ or Lorentz force) that accelerates radially inward of the charged particle flow (**Figure 3**). When the supplying current is time varying, the charged particles are attracted to each other under the influence of the Lorentz force, which causes shrinkage of the charged particle flux, i.e., the pinch effect appears. The effect leads to increase the ion density and pressure. A current flowing through the electrolyte squeezes smaller cylinder, until the magnetic force does not balance the pressure. The detailed physics of this process is still largely open

to debate and speculations because little quantitative data have been accumulated on the deposit ablation process, especially close to the exploding baths.
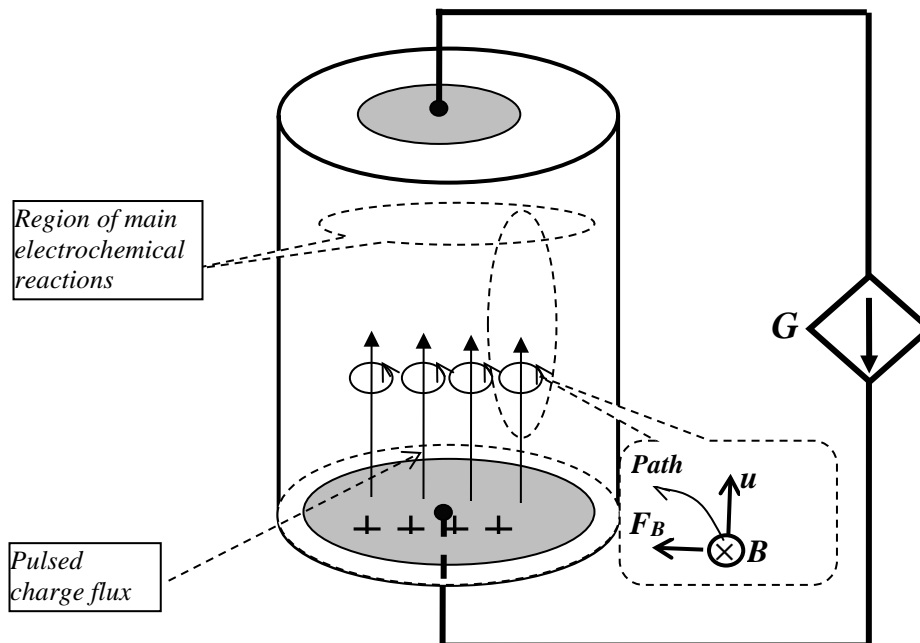
Figure 3. Coupled processes generated by pulsed current between electrodes: *G* - pulsed current generator, *u* - charge drift velocity, *B* - magnetic field density, *F$_B$* - Lorentz force.

The magnetic properties of electrolytes and the interactions of internally induced magnetic fields on electrolyte properties and ionic transport characteristics have significant influence on the form of the mathematical model of the processes occurring in the electrochemical reactor.

A well-founded model of electrochemical processes occurring in the reactor should be based on the questions of change for mass, energy and momentum. The instantaneous state of an electrochemical reactor usually depends on several variables and is described by one or several state functions of one or several variables. For instance, considering the electrode variables, we must take into account the kind of the material, surface area, geometry and surface conditions. Such factors as mode transfer (diffusion, convection, migration, etc), surface concentrations and adsorptions have influences on the mass transfer variables. The temperature, pressure and time appear as external variables. Moreover, there are electrical variables such as the charge, current and potential. As solution variables, we have the bulk concentrations of electroactive species, concentrations of other species and the kind of the solvent. It can be easily verified that the aspect of current distribution can have a major effect on the performance of electrochemical processes.

The electrodeposition process can be described by a mathematical model derived from the Maxwell equations and mass balance equations as follows. From the charge conservation principle, the equation for charge continuity takes the form:

$$\nabla J_c = -\frac{\partial \rho_q}{\partial t} \tag{2}$$

Where, J_c and ρ_q denote the current density vector and charge volume density, respectively.

The general electric field intensity *E* is governed by the Maxwell-Faraday equation:

$$E = -\nabla V - \frac{\partial A}{\partial t} \tag{3}$$

Where, *V* is the scalar electric potential, and *A* is the magnetic vector potential. The magnetic vector potential *A* is defined, so that the magnetic field density *B* is given by:

$$B = \nabla \times A \tag{4}$$

In the presence of a current distribution as a source for the magnetic field, the magnetic field density can be found from the Biot-Savart law:

$$B = \frac{\mu}{4\pi} \int \frac{J_c(p) \times (r-p)}{|r-p|^2} dv \tag{5}$$

Where, the integral extends over all space v. Generally, the Biot-Savart law is difficult to apply. It is often easier to first calculate the magnetic

vector potential for which we need to derive a differential equation. Taking into considerations time dependent sources, i.e., charge and current distributions that vary in time we can somewhat artificially divide electric current into two components: "external" current that generates electromagnetic field and "induced" current caused by electromagnetic field.

Substituting (3) and (4) into Maxwell's equations yields:

$$\nabla^2 A - \mu\varepsilon\frac{\partial^2 A}{\partial t^2} = -\mu\varepsilon J_c \qquad (6)$$

This is the wave equation for the vector potential A.

Following a similar procedure and starting by taking into account the curl of the magnetic field strength H, we obtain the wave equation for the magnetic field, namely:

$$\nabla^2 H - \mu\varepsilon\frac{\partial^2 H}{\partial t^2} = -\nabla \times J_c \qquad (7)$$

For the electric field, we find that the wave equation in the presence of source takes the form:

$$\nabla^2 E - \mu\varepsilon\frac{\partial^2 E}{\partial t^2} = \mu\frac{\partial J_c}{\partial t} + \nabla(\rho_q/\varepsilon) \qquad (8)$$

It is easily seen that the wave equation for the magnetic field has only a source term dependent on the electric current J_c, whereas the wave equation for the electric field includes a source term for the electric charge ρ_q. This is a consequence that there are no magnetic monopoles.

According to the Lorentz force, the induced current J_{in} from the electrolyte velocity u and the magnetic field B is determined by:

$$J_{in} = \sigma u \times B \qquad (9)$$

Where, σ denotes the electrolyte conductivity.

The total current density is then:

$$J = J_c + J_{in} \qquad (10)$$

The continuous form of the Lorentz force is[19]:

$$F = \rho_q E + J \times B \qquad (11)$$

Where, ρ_q is the charge density, J is the total current density, and B is the magnetic field density.

The Lorentz force per unit volume F can be applied as an external force in the Navier-Stokes equations. Thus, the second step in solving this electrochemical reactor problem is to determine the electrolyte velocity using the Navier-Stokes equations for laminar incompressible flow:

$$\rho_f\frac{\partial u}{\partial t} + \rho_f(u\cdot\nabla)u = \nabla\cdot[-\delta I + \vartheta(\nabla u + (\nabla u)^T)] + F \qquad (12)$$

Where, ρ_f is the fluid density, ϑ is the dynamic viscosity, δ is the pressure, and I is the identity matrix. Equations (9) and (12) are coupled in u and require a simultaneous solution. We assume that the flow of charged particles is incompressible, so the flow continuity equation simplifies to:

$$\rho_f\nabla\cdot u = 0 \qquad (13)$$

It is now obvious that the solution for the ions velocity u and pressure δ can be evaluated under various conditions.

An interesting point related to the presented studies is that the problems of the nature of charge carriers, the coupling of their motion, and the contribution of migration to the ions flux, respectively, could be analyzed in detail. Owing to the potential dependence of nucleation, growth, and roughness evolution processes, thus the deposit morphology can vary with radial position and can adversely affect product quality. It is worth noticing that the exact solution of the above set of equations for real multi-component electrolytes is rather complicated.

Therefore, by imposing appropriate restrictions which are satisfied under corresponding electroplating conditions, it is possible elaborate models which lead to satisfied results when matching them with experimental data. Such models have a twofold purpose: first, they can account all the facts discovered experimentally, and second, they can be able to predict the system behaviour under various conditions. Starting from this general imperative, the elaboration of a model for the interface phenomena can be performed by making a certain number of hypotheses which generally simplify the governing equations (2) and (13).

4. Computer simulations of mixed mode oscillations

At present, the derivation of a model from the basic equation is an error prone and time-consuming task normally requiring specific expertise. Fortunately, at the same time, computer simulation techniques are gaining more importance in the industry practice. This leads to an increasing gap between supply and demand of well-defined, consistent models. A relatively simple model (if it is appropriate) enables us to select the variables that

govern performance. However, due to mathematical difficulties in solution of diffusion-migration transport equations, different simplifications are necessary. Very often, some uncertainty in the numerical values of the model constants is not usually important and methodology commonly used in many engineering practice today gives enough support for the researcher in the task of deriving a specific model.

Moreover, when the computational analysis is combined with the electrochemical impedance spectroscopy, the results may suggest operating parameters that differ from either of the assumed individual results. While these findings indicate an operating regime of higher electrolyte velocities, whether that translates into increased depositing performance, will require pulse current validation corrections. The electrochemical impedance spectroscopy is used to determine the impedance of an electrochemical reactor at different sinusoidal frequencies under given conditions - in this case, a range of supplying current magnitudes and frequencies. The response of the reactor to a sinusoidal input could give insights relevant to pulse current frequency[8].

Generally, the manufacturing of nanostructures is too complicated for proper theory, so this has been the domain of computer simulations. We will start by considering simulations of electrochemical nanostructure depositions, and will then turn toward current-voltage relations to gain insights into the charge – electrolyte concentration and coupling mechanisms ultimately responsible for different pattern of the reactor output quantities and to identify the relationship between them. It should be emphasized that the circuit modelling not only aids semiconductor manufacturers in immediate returns on investment like increased yield and decreased consumable costs, but models are essential to understand the mechanisms that enable of material and cause process variation, which affects device performance and process efficiency. The equivalent circuit model predicts the capacitive and Faradic currents of the process, and with the same average and peak current density, the ramp up waveform has higher instantaneous peak current to charge

transfer, which results in an improvement in the microstructure of the nanocomposite.

Nonlinear interactions between these quantities may permit the emergence of highly characteristic oscillatory behaviour known as quasi-periodicity and mixed mode dynamics, in addition to chaos. The investigation of the involved circuit gives information also on the structure of relationships expected in special cases. To quantify the evolution of the electrochemical reactor processes with respect to time, the equivalent circuit was used. It is depicted in **Figure 4**.
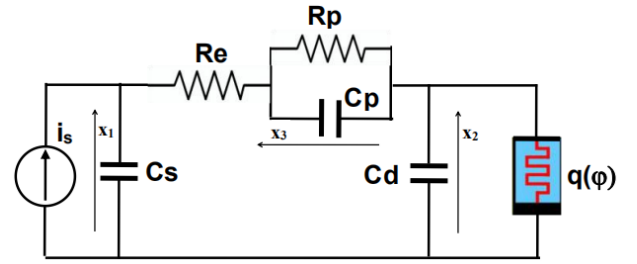
Figure 4. Circuit model of electrochemical deposition processes.

Applying circuit laws, we can establish the mathematical description of the above model and obtain:

$$\dot{x}_1 = k_1 \left(\frac{x_2 + x_3 - x_1}{R_e} + i_s \right),$$
$$\dot{x}_2 = k_2 \left(-\frac{x_2 + x_3 - x_1}{R_e} - (a + 3bx_4^2)x_2 \right),$$
$$\dot{x}_3 = k_3 \left(-\frac{x_2 + x_3 - x_1}{R_e} - \frac{x_3}{R_p} \right),$$
$$\dot{x}_4 = x_2. \tag{14}$$

Where, $k_1 = 1/C_s$, $k_2 = 1/C_d$, $k_3 = 1/C_p$ and $x_4 = \varphi$. The dot is taken as a symbol for differentiation with respect to time.

Due to the complex form of the established system of equations, the determination of their analytical solution is not an easy task and therefore, to examine the effect of various system parameters on the electrocrystallization process, we can perform numerical calculations applying a computer program MATLAB with using effective numerical integration procedures.

We will start by considering the following quantities: $i_s = I = 15$ A for $0 < t < T/2$ and $i_s = -I = -15$ A for $T/2 < t < T$ with $i_s(t) = i_s(t + T)$, $R_e = 0.5$ Ω, $R_p = 5$ kΩ, $C_s = 0.01$ F, $C_d = 0.278$ F, $C_p = 0.05$ F. The charge - magnetic characteristic of the memristive element representing the relation be-

tween the current and its own magnetic field takes the form: $q(\varphi) = a\varphi + b\varphi^3$, where a and b denote constant parameters.

Applying the mentioned numerical procedure implemented in MATLAB, we get the solutions shown in **Figure 5** and **Figure 6** for different time varying i_s. We solved (14) with the variable step ODE45 procedure from MATLAB with RelEr = AbsEr = 10^{-6} and $0 \leq t \leq 20$s and zero initial conditions. The steady-state response of the large amplitude oscillations were identified in the interval $2s \leq t \leq 20$s. Note also that the type of the supplying current i_s exhibits very different system responses, in particular with regard to changes in time of the magnetic flux and voltage - current characteristics of the reactor.

(a)

(b)

(c)

(d)
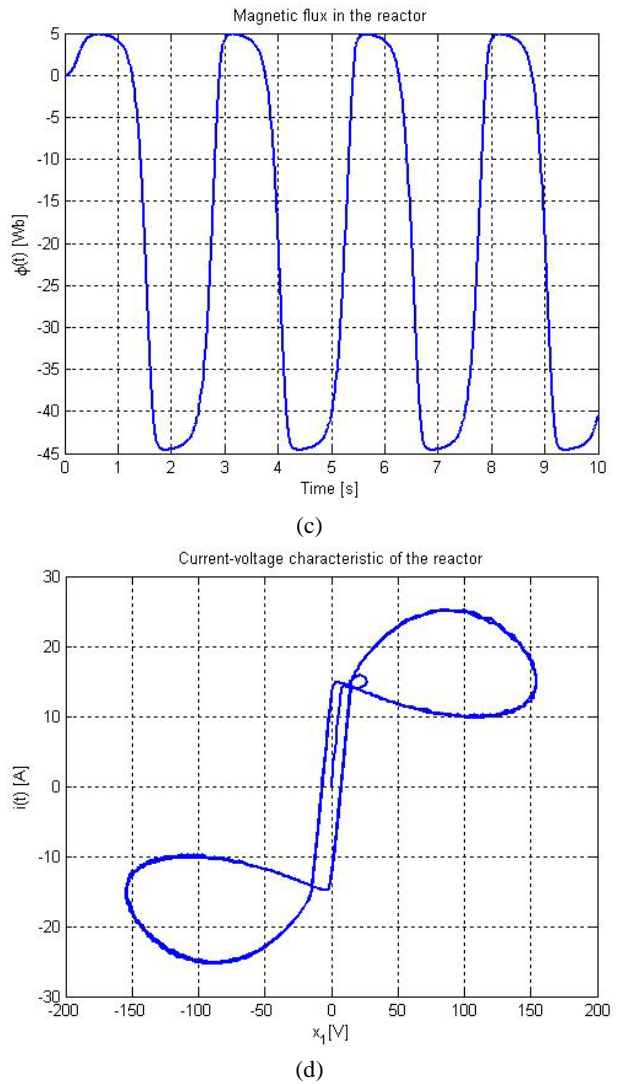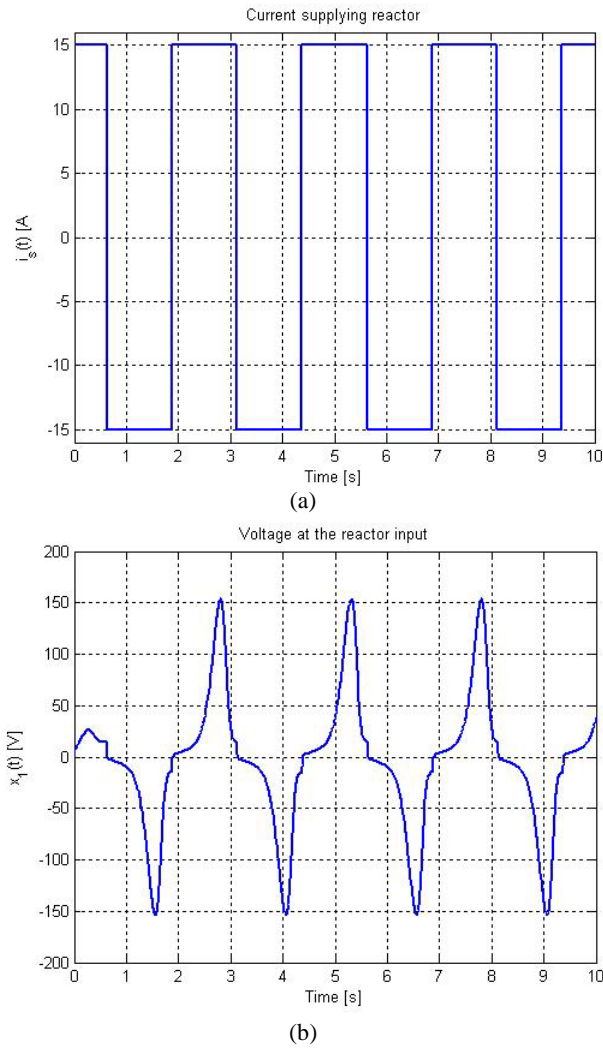
Figure 5. Changes in time of supplying current (**a**), voltage (**b**) and magnetic flux (**c**) in the reactor and voltage - current characteristic (**d**) of the reactor.

The important point to note here lies in the fact that in the case of supplying the system from a straight sinusoidal current rectifier, the current flowing through the reactor takes similar course in time to the supplying current and a significantly different nature of the magnetic flux waveform is exhibited and, with the over time, it tends to a constant value. However, in the case of supplying the reactor with periodic bipolar current, the current flowing through the reactor takes very different course from it in time. Moreover, the steady-state voltage-current characteristics of the reactor in these two cases of supplying currents take considerably different shapes, which appear as a result from the influence of a significant constant in time component which is contained in the rectified sinusoidal current. Although simple topologically, the system

27

can exhibit complex dynamical responses and its dynamical properties can be characterized through Farey arithmetic and fractal dimensions of their devil's staircases. Several interesting properties of the circuits can be identified through bifurcation diagrams, phase plane and time series responses[16].
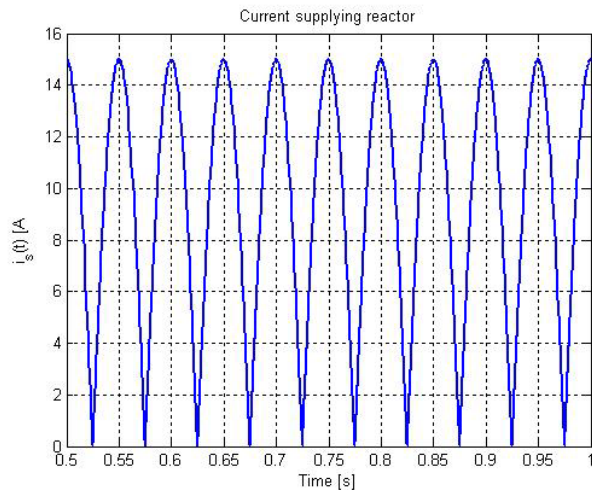
(a)
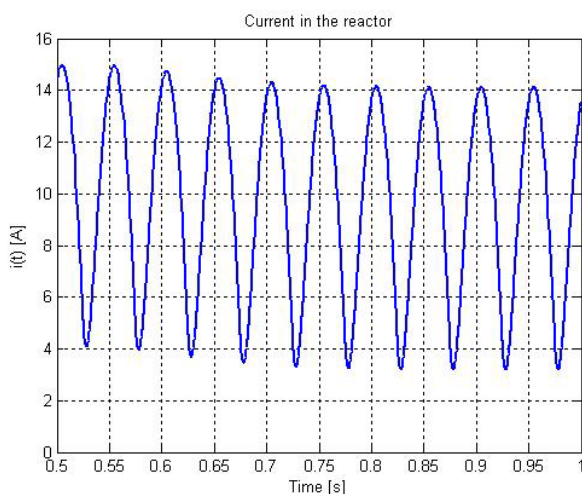
(b)
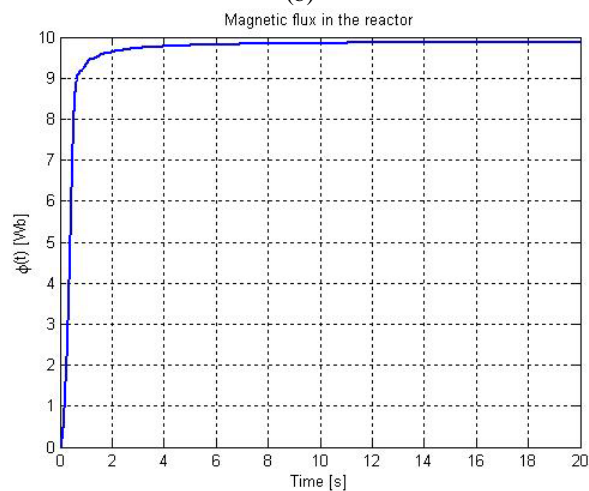
(c)
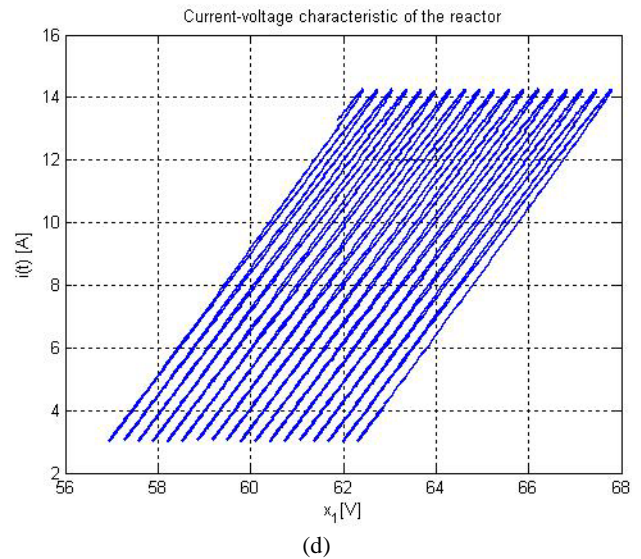
(d)

Figure 6. Varying in time: **(a)** supplying rectified sinusoidal current, **(b)**, **(c)** current and magnetic flux in the reactor, **(d)** voltage - current characteristic of the reactor.

From the extensive set of solutions, we will focus in what follows our attention on the particular type of voltage and current waveforms that can be accordingly transformed on the effects of the electrochemical processes. It has to be noted that the aspect of circuit variables distribution can have a major effect on the reactor performance. A detailed analysis is outside the scope of this article, although it may give a qualitative view of the effect due to its significance in design of electrochemical reactors for industrial processes.

In such a case as that above-mentioned, one of the important problems is concerned with mixed mode oscillations (MMOs), which have not been investigated so far in relation to electrochemical reactors. No results on memristive electrochemical reactors with mixed-mode oscillation responses have been published yet. Those interesting periodic oscillatory responses have been reported in resistive nonlinear circuits (usually having cubic current–voltage characteristics) and in the tunnel diode and Bonhoeffer-van der Pol oscillators, the Hudgkin-Huxley model of neuron dynamics, Belousov-Zhabotinskii chemical reaction, Taylor-Couette flow, surface oxidation and autocatalytic reactions, human heart arrhythmias and in epileptic brain neuron activity[17].

28

(a)

(d)
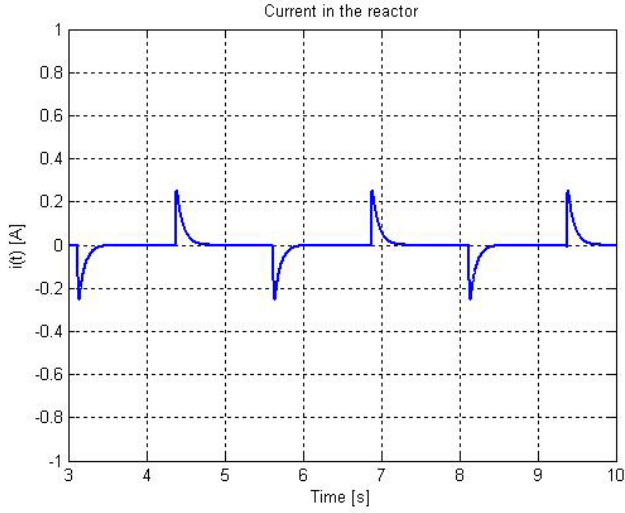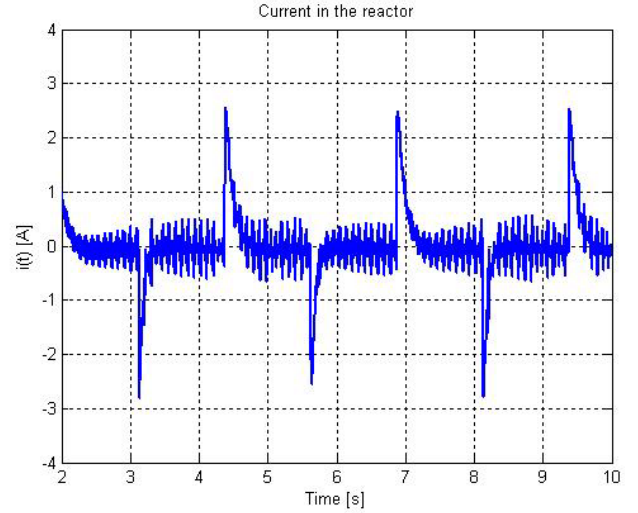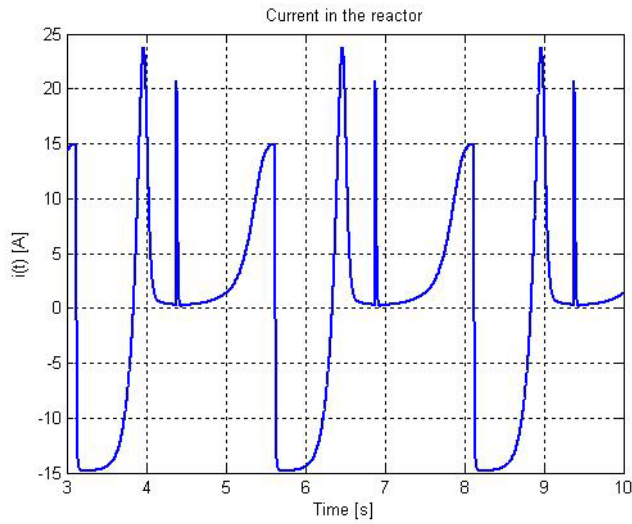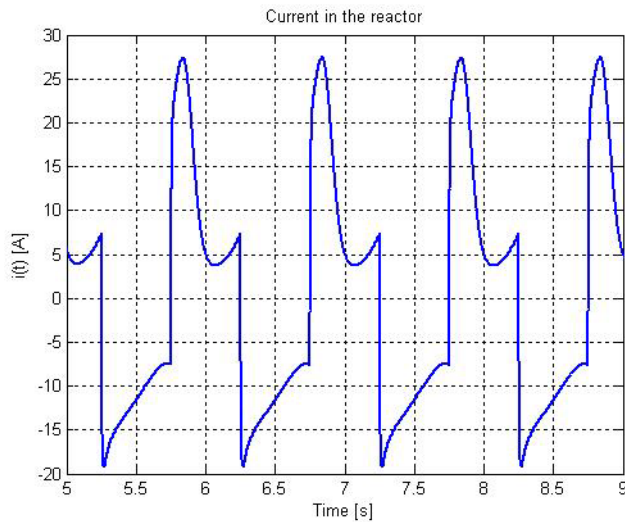
Figure 7. Solutions of (14) for various sets of parameters I and b with unchanged other parameters: **(a)** SAO at $I = 0.15$ A, $a = -1.75$ and $b = 0.15$, **(b)** LAO at $I = 15$ A, $a = -2.75$ and $b = 0.15$, **(c)** LAO at $I = 15$ A, $a = -1.25$ and $b = 0.15$, **(d)** MMO at $I = 1.5$ A, $a = -1.75$, $b = 0.15$ and $T = 2.5$ s.

(b)

(c)

Generally, to MMOs, we refer complex patterns that arise in dynamical systems, exhibiting oscillations with different amplitudes that are interspersed. These amplitude regimes differ roughly by an order of magnitude. By changing appropriate variables or parameters of a system, MMOs may occur in larger regions as the dynamical switches between small amplitude oscillations (SAOs) and large amplitude oscillations (LAOs) by changing appropriate variables or parameters of a system. As the control parameter is varied, MMOs exhibiting alternation between SAOs and LAOs can arise. The system can be considered as a coupling of two oscillators: linear and nonlinear ones. In our analysis, we use the letters L and s in L^s to describe the number of local maximum values of steady-state LAOs and SAOs, respectively, and not the number of LAOs and SAOs. It is worth pointing out that the MMOs of type L^s are not the only possible dynamical characterization of such systems. In fact, all parameters (T, I, R_e, R_p, C_p, C_s, C_d, a and b) in (14) may be considered as bifurcation parameters. We will analyze local maximum values of LAOs and SAOs and show that, by slowly changing, any of the above parameters, we can obtain local maximum values of the charges, magnetic fluxes, currents and voltages that can form appropriate sequences. We emphasize that a numerical technique addressing this coupled phenomenon for all ranges

29

of parameters will open the possibilities for value-added electrochemical processes and producing new materials.
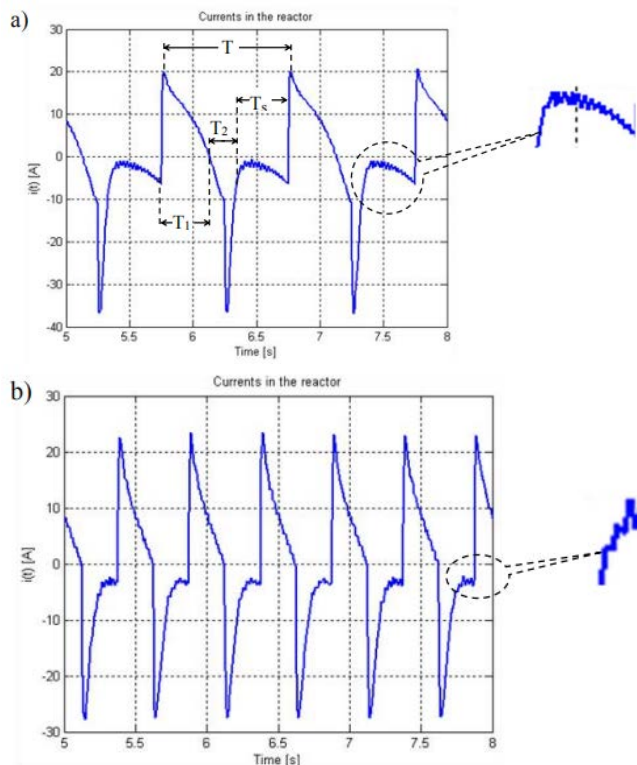
Figure 8. MMOs: a) 1^{18} for $T = 1$ s, b) 1^7 for $T = 0.5$ s.

The three basic modes of operation are illu-strated in **Figure 7**, which shows the solutions of (14) with $I \, \epsilon \, \{0.15, 1.5, 15\}$A, $a \, \epsilon \, \{-1.25, -1.75, -2.75\}$, $b = 0.15$ and $T \, \epsilon \, \{1, 2.5\}s$. In the SAOs only case, the small amplitude oscillations around the origin (0, 0, 0) are due to Hopf bifurcation for $a = 0$. In the LAOs only case, a trajectory passing close to the origin bypasses the region of small amplitude oscillations. The MMOs case is in some sense a combination of the previous two cases. The mechanism in which SAOs and LAOs occur is quite complex and has been the topics of recent papers Brons M *et al.* and Marszalek W *et al.* In the MMOs case, a series of SAOs around the origin (considered canard solutions) undergoes a rapid canard explosion yielding an LAO, which, through a special return mechanism brings back the system into the vicinity of the origin. The canard explosion described in detail in reference 13[13] is triggered when a trajectory leaves a fold point of a cubic nonlinearity, ending a series of SAOs and entering the relaxation mode with one or more LAOs. This explosion occurs, for example, in **Figure 7**, bottom right part, when two or four SAOs transform into an LAO. Depending on the parameters, the system may continue with one (or more) LAOs, or may go through a new series of SAOs after which trajectory leaves again the vicinity of the origin (a fold) and the phenomenon repeats.

Each period of MMOs can be divided into intervals of various nature: intervals with a sequence of SAOs and intervals of LAOs. One period of LAOs can be estimated as $T_L = T_1 + T_2$ (as shown in **Figure 8**) and one period of SAOs can be determined as whole duration interval T_s divided by s, indicating the number of local maximum values of steady state SAOs. Thus, the total period of one MMOs oscillation is $T = T_L + T_s$. The corresponding expressions specifying the individual components of the period T are presented in reference 14[14] and can easily be adapted to the case under examination.

Taking into account a small amount of perturbation in the characteristic $q(\varphi)$, it is possible to get MMOs exhibiting in each period a train of SAOs separated by a large amplitude pulse (**Figure 9(a)**). Varying pairs of control parameters, one can observe how the dynamical behaviour of the system changes and map out "dynamical phase diagrams", showing regions of the parameter space in which qualitatively different MMOs occurs, or, by varying a single parameter, one can trace out hysteresis loops of the sort shown in **Figure 9(b)**. This type of time-varying electric currents and magnetic fields are most probably generated by an electric double layer within individual particles and a temporal excess of ion carriers within the sample. Perhaps the shape and magnitude of the induced temporal signals depend on the reaction zone propagation mode, reaction mechanism, and reactant properties. It is worth noticing that the exact solution of the above set of equations for real multi-component electrolytes is rather complicated. Therefore, by im-posing appropriate restrictions, which are satisfied under corresponding electroplating conditions, it is possible to elaborate models, which lead to satisfied results when matching them with experimental data.

(a)

(b)
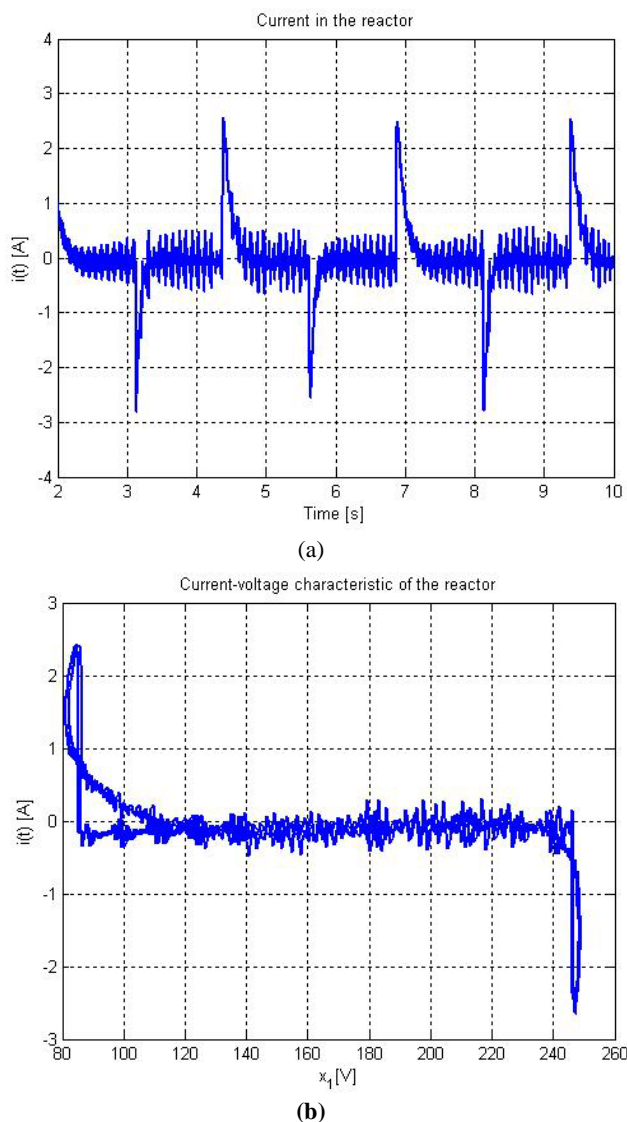
Figure 9. MMO at I = 1.5A (bipolar pulse), b = 0.5 and T = 2.5: **(a)** reactor current, **(b)** voltage-current characteristic of the reactor**.**

5. Conclusions

Electrocrystallization method gives the ability to control internal structure of the deposits, which has a great potential for use in the development of new material properties. This method is exceptionally suitable for preparations of specific materials, mainly the protective layers, and in the near future may be more effective than previously involved methods in surface modification technologies of known materials, as well as newly produced materials. These layers can be used together with their grounds or separated from them. Taking into account the specificity of materials electrollytically produced, it is possible the formation of such a structure of the material and its properties that

cannot be obtained by other technologies. The possibility of conscious control of the structures in the nanometric areas leads up to producing the useful materials with new properties and overcomes previously insurmountable barriers to the development of technology.

The problem of obtaining smooth, uniform layers can be solved by a combination of clever electrode design, electrolyte flow control and judicious use of the chemical additives that could lead to results desired. Significant improvement of the results can be achieved by appropriate modelling of processes occurring in the electrocrystallizator and taking into account the influence of its own magnetic field in the double layer near the working electrode. Circuit models can lead to methods for fast treating large quantities of electrocrystallizator data and extracting from them kinetic parameters importantly influenced the structure of the produced materials. Particular attention should be paid to the problem of the generation of processes with mixed mode oscillations, because they can favourably affect the quality of the material produced in electrochemical processes. This is of great importance in the case of nanostructured materials, whose final structure is very sensitive to rapid changes in the conditions of the manufacturing process. A particularly interesting context is that of current waveforms supplying the electrocrystallizator, because their influences on mixed mode oscillations seem most important for the efficiency of realized processes.

Conflict of interest

No conflict of interest was reported by the author.

References

1. Silberberg M. Chemistry - The molecular nature of matter and change. New York: McGraw-Hill Science/Engineering/Math; 2008.
2. Epstein IR, Pojman JA. An introduction to nonlinear chemical dynamics: Oscillations, waves, patterns, and chaos. New York: Oxford University Press; 1998.
3. Laganà A, Gregory AP. Chemical reactions. Basic theory and computing. New Yok:Springer; 2018.
4. Trzaska M, Trzaska Z. Nanomaterials produced by electrocrystallization method. In: Aliofkhazraei M,

31

Makhlouf A (editors). Handbook of nanoelectrochemistry. New York: Springer, Cham; 2016. p. 135–167.

5. Lona F, Maria L. Step by step approach to the modeling of chemical engineering processes. Using Excel for simulation. New Yok: Springer; 2018.

6. Kreysa G, Ota Ken-ichiro, Savinell RF. (editors). Encyclopedia of applied electrochemistry. New York: Springer; 2014.

7. Cieślak G, Trzaska M. Tribological properties of nanocomposite Ni/graphene coatings produced by electrochemical reduction method. Composites: Theory and Practice 2016; 2: 79–83.

8. Trzaska M, Trzaska Z. Electrochemical impedance spectroscopy in materials engineering. Warsaw: Publisher Office of the Warsaw University of Technology; 2010.

9. Sangeetha S, Kalaignan GP, Anthuvan JT. Pulse electrodeposition of self-lubricating Ni–W/PTFE nanocomposite coatings on mild steel surface. Applied Surface Science 2015; 359: 412–419.

10. Kamnerdkhag P, Free ML, Shah A, *et al.* The effects of duty cycles on pulsed current electrodeposition of ZneNieAl$_2$O$_3$ composite on steel substrate: Microstructures, hardness and corrosion resistance". International Journal of Hydrogen Energy 2017; 42: 20783–20790.

11. Jabbar A, Ghulam Y, Waheed QK, *et al.* Electrochemical deposition of nickel graphene composite coatings: Effect of deposition temperature on its surface morphology and corrosion resistance. The Royal Society of Chemistry 2017; 7: 31100–31109.

12. Djokić SS. Electrodeposition: theory and practice. New York: Springer; 2010.

13. Brons M, Kaper TJ, Rotstein HG. Introduction to focus issue: Mixed-mode oscillations: experiment, computation, and analysis. Chaos: An Interdisciplinary Journal of Nonlinear Science 2008; 18(1).

14. Marszalek W, Trzaska ZW. Mixed-mode oscillations in a modified Chua's circuit. Circuits, Systems and Signal Processing 2010; 29(6): 1075–1087.

15. Marszalek W, Trzaska ZW. Properties of memristive circuits with mixed-mode oscillations. Electronics Letters 2015; 51(2): 140–141.

16. Beardmore RE, Laister R. The flow of a differential-algebraic equation near a singular equilibrium. SIAM Journal on Matrix Analysis & Applications 2002; 24(1): 106–120.

17. Sagués F, Epstein IR. Nonlinear chemical dynamics. Dalton Transactions 2003; 7: 1201–1217.

ORIGINAL RESEARCH ARTICLE

Convective flow boiling heat transfer in an annular space: N-heptane/water case in a bubbly sub-cooled flow

M. M. Sarafraz[1*], H. Arya[2]

[1] *Faculty of Chemical, Petroleum and Gas Engineering, Semnan University, Semnan, Iran. E-mail: mohamadmohsensarafraz@gmail.com*

[2] *Center for Energy Resource Engineering, Technical University of Denmark, Denmark*

ABSTRACT

The subcooled flow boiling heat transfer characteristics of n-heptane and water is conducted for an upward flow inside the vertical annulus with an inner gap of 30 mm, in different heat fluxes up to 132kW.m^{-2}, subcooling max.:30C, flow rate: 1.5 to 3.5lit.min^{-1} under the atmospheric pressure. The measured data indicate that the subcooled flow boiling heat transfer coefficient significantly increases with increasing liquid flow rate and heat flux and slightly decreases with decreasing the subcooling level. Although results demonstrate that subcooling is the most effective operation parameter on onset of nucleate boiling such that with decreasing the subcooling level, the inception heat flux significantly decreases. Besides, recorded results from the visualization of flow show that the mean diameter of the bubbles departing from the heating surface decreases slightly with increasing the flow rate and slightly decreases with decreasing the subcooling level. Meanwhile, comparisons of the present heat transfer data for n-heptane and water in the same annulus and with some existing correlations are investigated. Results of comparisons reveal an excellent agreement between experimental data and those of calculated by Chen Type model and Gungor–Winterton predicting correlation.

Keywords: Annular Flow; Nucleate Flow Boiling; Subcooled; Pure Liquid; Convective; Heat Transfer

ARTICLE INFO

COPYRIGHT

1. Introduction

Flow boiling has long played a major role in many technological applications due to its superior heat transfer performance. The complexities encountered in the boiling process have stimulated numerous investigators to conduct extensive research in this field. Because of unknown properties which are hidden inside of boiling phenomenon, many investigators have conducted large number of experiments on different substances. This complexity is due to the heterogeneous nature of heat transfer medium. Boiling of liquid mixtures is furthermore integrated with simultaneous heat and mass transfer between vapor inside the bubble and the vapor/liquid interface, which makes the phenomenon much more complicated. So far, the boiling phenomenon has not been modeled through any simple theoretical model. Flow boiling heat transfer is also one of the major interests to designers of water liquid cooled nuclear reactors. One source of concern is reactor behavior following a hypothetical loss-of-flow accident or cooling flow was unable to provide the sufficient heat transfer. In this particular case, exceeding the heat flux up to critical heat flux can lead to irrecoverable damages to the reactor and industrial installations. Subcooled boiling is characterized by the

generation of vapour bubbles at the heater surface, while the bulk temperature of the liquid is still below the saturation temperature. Bubbles detaching from the heat transfer surface collapse and condense in the subcooled liquid bulk, while this situation basically occurs in almost every reactor or high temperature surfaces. It is particularly significant in nuclear reactors and even around the rod fuel pools. Many researchers have been performed several experiments to investigate the effects of various parameters on the subcooled flow boiling heat transfer. On the basis of the coolant fluid component(s), conducted researches may be sorted in terms of investigation on the subcooled flow boiling heat transfer to either pure liquids or mixtures, although the main object of this experimental study is to investigate the first group of test fluids.

2. Literature review

As an example of conducted researches, Zeitoun[1] performed a subcooled boiling test in a high heat flux condition. However, the test section for the boiling heat transfer was short in length and local bubble parameters were not provided. Early visualization experiments carried out by Hewitt *et al*.[2] showed that the bubbles affect the nucleation activity. The presence of moving bubbles leads to the wave-induced nucleation phenomenon observed by Barbosa *et al*.[3]. He conducted experiments in a vertical annulus in which heat was applied to the inner surface of the tube. A dominance of nucleate boiling was observed at low qualities. At high qualities, nucleate boiling was partly or totally suppressed and forced convection became the dominant mechanism. Thus, one may conclude that in internal flow boiling, the heat transfer coefficient is a combination of two mechanisms: nucleate boiling and forced convection. The heat transfer coefficient might remain constant, decrease or increase depending on the contribution of these two mechanisms during forced saturation boiling. You *et al*.[4] conducted experiments on subcooled flow boiling heat transfer of water-sugar mixture to show the effects of heat flux, fluid velocity, and subcooling on the enhancement

of nucleate boiling heat transfer in the partial flow boiling regime, where both forced convection and nucleate boiling heat transfer occurred. They found that increasing the sugar concentration led to a significant drop in the observed heat transfer coefficient because of a mixture effect, which resulted in a local rise in the saturation temperature of sugar solution at the vapor-liquid interface. Peyghambarzadeh *et al*.[5] performed a large number of experiments to measure the heat transfer reduction and fouling resistance of $CaSO_4$ aqueous solutions and pure water in a vertical upward annulus under subcooled flow boiling condition. Experiments are designed so that the effects of different parameters such as solution concentration, wall temperatures, and heat flux as well as flow velocity on flow boiling heat transfer coefficient would be clarified. Ahmady *et al*.[6] conducted the experimental study of onset of subcooled annular flow boiling and surveyed the effect of pressure, mass flux, and inlet temperature of annulus on the inception heat flux. They illustrated that inlet temperature directly influences on the inception heat flux. For an extensive literature survey of flow boiling in conventional-size channels, the interested readers are referred to Kew and Cornwell[7] and Lin *et al*.,[8] or for small-diameter channels to Kandlikar and Grande[9] and Kandlikar[10], or Chen[11] and Bergles *et al*.[12] In general, all existing approaches are either the empirical fits to the experimental data, or form an attempt to combine two major influences to heat transfer, namely, the convective flow boiling without bubble generation, and the nucleate boiling. Generally, that is done in a linear or nonlinear manner. Alternatively, there is a group of modern approaches based on models that start from modeling a specific flow structure and in such a way postulate more accurate flow boiling models, usually pertinent to slug and annular flows. One of the first major works in this area was that of Celata *et al*.[13] who reported data for binary mixtures in forced convection zone. They compared their data with other correlations such as Guerrieri and Talty[14], but in each case, found considerable scatter. They then proposed their own correlation. Chang

and Kim[15] presented a survey of performance and heat transfer characteristics of hydrocarbon refrigerants and their mixtures (R290, R600, R600a, R290/R600and R290/R600) in a heat pump system. Sivagnanam et al.[16] studied subcooled flow boiling of binary mixtures on a long platinum wire and proposed correlations for the partial boiling and fully developed boiling. Ose and Kunigu[17] conducted the experiments in order to clarify the heat transfer characteristics of the subcooled pool boiling and to discuss the effect of various parameters on the flow boiling heat transfer. A boiling and condensation model for numerical simulation of subcooled boiling phenomenon was developed too. Lima et al.[18] presented flow boiling heat transfer results of R-134a flowing inside a 13.84 mm internal diameter, smooth horizontal copper tube. They investigated the effect of types of flow on the flow boiling heat transfer mechanism and presented that a local minimum heat transfer coefficient systematically occurs within slug flow pattern or near the slug-to-intermittent flow pattern transition. The vapor quality at which the local minimum occurs seems to be primarily sensitive to mass velocity and heat flux. Thus, it is influenced by the competition between nucleate and convective boiling mechanisms that control the flow boiling. Hou et al.[19] investigated the boiling heat transfer in small diameter tubes using R134a as the working fluid. The heat transfer experiments were conducted with two stainless steel tubes of internal diameter 4.26 and 2.01 mm. They also conducted the flow visualization experiments using the same experimental facility with Pyrex glass tubes. A flow pattern map was obtained at a system pressure of 10 bar and tube diameter of 4.26 mm and the effects of different operating parameters on the flow boiling heat transfer coefficient have been experimentally investigated. Celata et al.[20] presented the results of the flow boiling patterns of FC-72 in a micro-tube inside the pyrex glass tube in order to obtain the visualization of the flow pattern along the heated channel. Different types of flow pattern were observed. The experiments represented various data at related heat fluxes and low sub-cooling levels. They showed different flow patterns in the presence of flow instabilities

in bubbly/slug flow and slug/annular flow. Orian et al.[21] conducted experimental study on the flow boiling of binary organic solution in a horizontal tube. An organic mixture of miscible fluids, chlorodifluoromethane (R22)–dimethyl-lacetamide (DMAC) was circulated through the experimental system. The influence of the heat source, flow rate, solution concentration, and operating pressure on the flow characteristics and the heat transfer coefficient was examined experimentally. Based on the experimental observation, an appropriate flow pattern map was constructed. Hetsroni et al.[22] studied the influence of concentration of surfactants on augmentation of heat transfer coefficient of mixtures inside the annulus and compared the results to that of pure water. They also reported that the addition of surfactant to the water produced a large number of bubbles of small diameter, which, at high heat fluxes, tend to cover the entire heater surface with a vapor blanket. Similarly, Inoue and Monde[23] investigated the effect of surfactant on the enhancement of the heat transfer coefficient in deionized water and ammonia/water mixtures. More relevant studies may also be found in the literature[24–27].

The objective of this study is to identify the effect of operation parameters on subcooled flow boiling and comparing the experimental data with existing correlations. Several experiments were conducted covering different ranges of flow rate, inlet temperature (subcooling effect) and heat flux inside the vertical annulus. On the contrary, to similar earlier works, moreover than investigating on the effect of these operation parameters on flow boiling heat transfer coefficient, influence of operation parameters on the visualized mean bubble diameter size have simultaneously been surveyed. Then after, comparisons between some well-known predicting correlations (Chen type model and Gungor-Winterton) and experimental data were comparatively performed. For these models, results reveal the fair agreement between experimental data and those of calculated by correlations.

3. Experimental

3.1. Experimental apparatus

35

Figure 1 shows the test apparatus used for the present investigation. The liquid flows in a closed loop consisting of temperature controlled storage tank, centrifugal pump and the annular test section. The flow velocity of the fluid was measured with a calibrated vertical rotameter (manufactured by Sarir-teb Co.). The fluid temperature was measured by two PT-100 thermometers installed in two thermo-well located just before and after the annular section. The complete cylinder was made from stainless steel 316a. Thermometer voltages, current and voltage drop from the test heater were all measured and processed with a data acquisition system in conjunction with a PID temperature controller. The test section shown in **Figure 2** consists of an electrically heated cylindrical DC bolt heater (manufactured by Cetal Co.) with a stainless steel surface, which is mounted concentrically within the surrounding pipe. The dimensions of the test section are: diameter of heating rod, 20 mm; annular gap diameter (hydraulic diameter), 30 mm; the length of the pyrex tube, 500 mm; the length of stainless steel rod, 350 mm; the length of heated section, 150 mm which means that just the first 150 mm of stainless steel is heated uniformly and radially by the heater. The axial heat transfer thorough the rod can be ignored according to the insulation of the both ends of the heater. The heat flux and wall temperature can be as high as 132,000 W.m^{-2} and 150°C, respectively. The local wall temperatures have been measured with four stainless steel sheathed K-type thermocouples which have been installed close to the heat transfer surface. The temperature drop between the thermocouples location and the heat transfer surface can be calculated from:

$$T_w = T_{th} - \dot{q}\frac{s}{\lambda_w} \qquad (1)$$

The ratio between the distance of the thermometers from the surface and the thermal conductivity of the tube material (s/λ_w) was determined for each K-type thermocouple by calibration using Wilson plot technique[28]. The average temperature difference for each test section was the arithmetic average of the four thermometers readings around the rod circumference. The average of 10 voltage readings was used to determine the

difference between the wall and bulk temperature for each thermometer. All the K-type thermocouples were thoroughly calibrated using a constant temperature water bath, and their accuracy has been estimated to ±0.3K. The local heat transfer coefficient α is then calculated from:

$$\alpha = \frac{\dot{q}}{\left(T_w - T_b\right)_{ave.}} \qquad (2)$$

To minimize the thermal contact resistance, high quality silicone paste was injected into the thermocouple wells. To avoid possible heat loss, main tank circumferences were heavily insulated using industrial glass wool. To control the fluctuations due to the alternative current, a regular DC power supply was also employed to supply the needed voltage to central heater. Likewise, to visualize the flow and boiling phenomenon and record the proper images, annulus was made of the pyrex glass. More details of the test section and apparatus are given in **Figures (1-2)**.
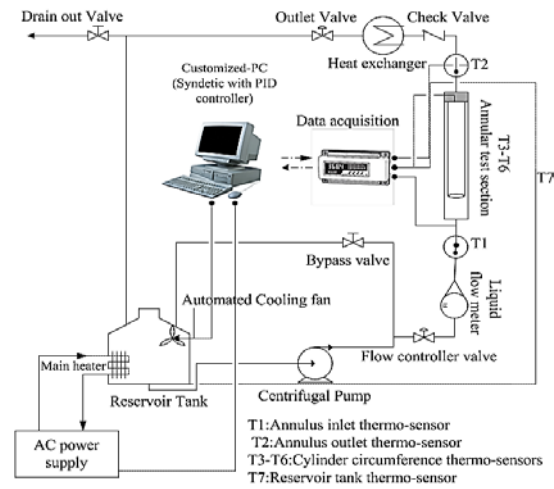
Figure 1. A scheme of the experimental apparatus.
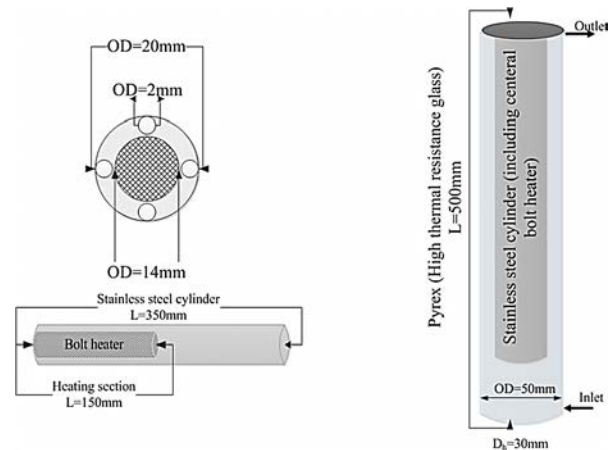
Figure 2. Details of the annular space and the heating section.

36

3.2 Experiment procedure

Prior to commencing a test run, test heater, reservoir tanks and pipes were acid washed and were cleaned to remove any scale from previous experiments. Once the system was cleaned, the test solution and the cleaning agent were introduced to the reservoir tanks. Following this, the tank heater was switched on and the temperature of the system increased. When the fluid had reached the desired temperature, the pump was started and the rig allowed to be stabilized at the desired bulk temperature and velocity. Then, the power was supplied to the test heater and kept at a pre-determined value. The data acquisition system was switched on and temperatures, pressure and heat flux were recorded.

3.3 Error analysis

The uncertainties of the experimental results are analyzed by the procedures proposed by Kline and McClintock[29]. The method is based on careful specifications of the uncertainties in the various primary experimental measurements. The heat transfer coefficient can be obtained using Eq. (3):

$$\alpha = \frac{\rho V C p (T_{out} - T_{in})}{(T_w - T_b)_{av.}} \qquad (3)$$

As seen from Eq. (3), the uncertainty in the measurement of the heat transfer coefficient can be related to the errors in the measurements of volume flow rate, hydraulic diameter, and all the temperatures as follows.

$$\alpha = f \{V, A_h, (T_{out} - T_{in}), (T_w - T_b)\} \qquad (4)$$

$$\partial\alpha =$$

$$\sqrt{\left[\left(\frac{\partial\alpha}{\partial V}\right).\delta V\right]^2 + \left[\left(\frac{\partial\alpha}{\partial A}\right).\delta A\right]^2 + \left[\left(\frac{\partial\alpha}{\partial(Tout - Tin)}\right).\delta(Tout - Tin)\right]^2}$$

$$+ \left[\left(\frac{\partial\alpha}{\partial(Tw - Tb)}\right).\delta(Tw - Tb)\right]^2 \qquad (5)$$

According to the above uncertainty analysis, the uncertainty in the measurement of the heat transfer coefficient is 16.23%. The detailed results from the present uncertainty analysis for the experiments conducted here are summarized in **Table 1**. The main source of uncertainty is due to the temperature measurement and its related

devices.

Table 1. Summary of the uncertainty analysis

Parameter	Uncertainty
Length, width and thickness, (m)	± 0.0005
Temperature, (K)	$\pm 0.3 K$
Water flow rate, (lit. min^{-1})	$\pm 1.5\%$ of readings
Voltage, (V)	$\pm 1\%$ of readings
Current, (A)	$\pm 0.02\%$ of readings
Cylinder side area, (m^2)	$\pm 4\times10^{-8}$
Flow boiling heat transfer coefficient, (W/m^2.K)	$\pm 16.23\%$

3.4 Operation parameters

The experimental apparatus provides the particular conditions to investigate the influence of heat fluxes, flow velocity, subcooling, and even concentration of mixture on flow boiling heat transfer coefficient (if binary or multi-component mixture is existed). Many experiments have been performed to investigate the effects of the operation parameters and subsequently, different values of parameters have been recorded. **Table 2** expresses the operation parameter conditions for water and n-heptane test fluids.

Table 2. Operation parameter values and experimental data

Parameter	Heat flux	Flow rate	Subcooling
Unit (SI)	kW/m^2	Lit/min	℃
range	5-132	1.5-3.5	10-30
Pressure	**Reynolds number**	**Data points**	**Heat transfer coefficient**
kPa	[ ]	[ ]	W/m^2. K
101.325	1970-3890	176	1052-7023

3.5 Physical properties of tested mixture

Water and n-heptane has been used as the test solution. The reported numerical values of physical properties are found to be inconsistent from different sources. In this investigation, all the physical properties have been calculated using standard correlations with known values of maximum expected uncertainty. The critical constants have been calculated using Joback method[30]. Expected uncertainty is reported equal to 7 K (~1%) for Tc; 2 bar (~5%). Liquid density for mixtures has been calculated by Spencer and Danner[31] method with the maximum expected uncertainty of 7%. Liquid thermal conductivities for liquids had been predicted by methods summarized by Bruce *et al*.[32]. The expected uncertainties are reported less than 10% for pure

liquids and up to 8% for liquid mixtures. Heat capacities for liquids have been calculated using Ruziicka and Domalski[33] method, with the expected uncertainty less than 4%. The heat capacities of liquid mixtures are estimated by mole fraction averages of the pure component values.

3.6 Calibrating the test heater

For the calibration of the test heater the well-known Wilson plot[34] was used which is explained here briefly. **Figure 3** shows a simple demonstration of the test heater and the locations of the thermocouples in it.
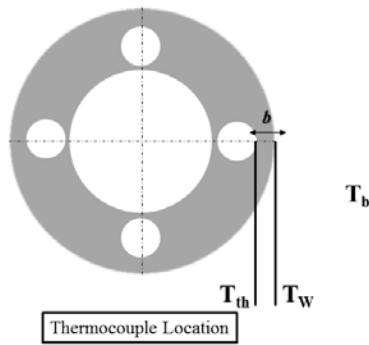
Figure 3. Thermocouple locations and calibration parameters.

As shown in **Figure 3**, the temperature shown by the thermocouple (T_{th}) is not exactly equal but it is slightly higher than the actual temperature of the heat transfer surface (T_w). This temperature difference is because of the conduction resistance of the heater material which is mounted between these two points. These temperatures can be related according to the energy balance under steady state condition:

$$q = U\left(T_{th} - T_b\right) = \alpha\left(T_w - T_b\right) = \frac{\lambda}{s}\left(T_{th} - T_w\right)$$ (6)

This relation can be simplified as follows:

$$\frac{1}{U} = \frac{1}{\alpha} + \frac{s}{\lambda}$$ (7)

If α can be calculated using some characteristics of the system like velocity, estimation would be obtained for s/λ using Eq. (4). For this purpose, the below relation is used:

$$\alpha \propto f.N_{Re}$$ (8)

For the plain tubes, friction factor is related to Reynolds number according to Blasius relation as follows:

$$f \propto \frac{1}{N_{Re}^{0.25}}$$ (9)

Having combinedtheequations 8 and 9, the following relation for heat transfer coefficient is obtained:

$$\alpha \propto N_{Re}^{0.75}$$ (10)

Since the bulk temperature is constant in each experiment, Reynolds number is proportional to the fluid velocity. Considering this point and unifying all the constants as "β", the following equation will be obtained:

$$\frac{1}{U} = \frac{\beta}{V^{0.75}} + \frac{s}{\lambda}$$ (11)

Eq. (11) shows that the plot of $1/U$ versus $1/V^{0.75}$ for each thermocouple gives the values of s/λ as the intercept of the line. **Figure 4** shows the calibration plot of the different thermocouples used in the test heater[35].
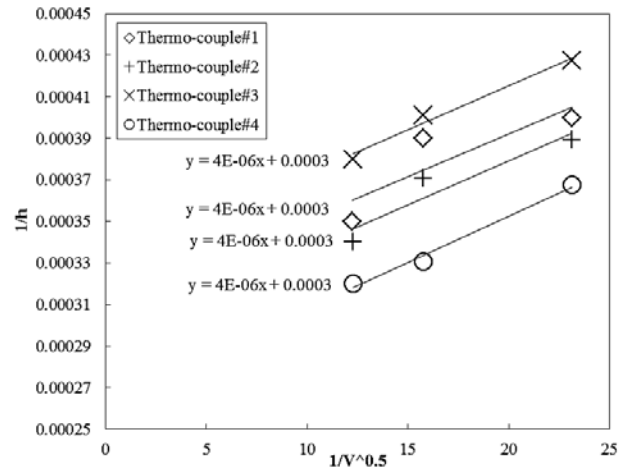
Figure 4. Calibration results for used K-type thermocouples.

This data were also taken under forced convective heat transfer to water at constant heat flux 8kW/m^2. As demonstrated in **Figure 4**, the values of s/λ for the thermocouples #1-4 are respectively equal to: 2.97×10^{-4}, 2.96×10^{-4}, 2.85×10^{-4}, 3.09×10^{-4} m^{2}K.W^{-1}. Performing the experiments again at other heat fluxes gives the value of 3×10^{-4}m^{2}K.W^{-1}as an average value of s/λ for all the thermocouples. This value was then used for the calibration of the surface thermocouples using Eq. (6).

4. Results and discussions

When we published our previous work[35], we

paid less attention to the effect of operating parameters on the generated bubbled diameters. Therefore, we were determined to investigate the effect of operating parameter on heat transfer coefficient, the bubble formation and size of mean bubble diameter separately.

4.1. Effect of heat flux

4.1.1 Effect of heat flux on flow boiling heat transfer coefficient

It is more convenient to show the effect of heat fluxon the flow boiling heat transfer coefficient in explicit terms of heat flux versus flow boiling heat transfer coefficient. **Figures (5-6)** show typical measured flow boiling heattransfer coefficients as a function of heat flux for pure n-heptane and deionized water, respectively, over a wide range of fluid velocity. Two distinct regimes can be observed: 1) at low heat fluxes, heat transfer occurs by convection mechanism and the heat transfer coefficient is almost independent of the heat flux and slightly changes can be observed with increasing the heat flux. It is because of the superimposed natural convection currents and due to changes in the physical properties of the fluids such as density, heat capacity and even viscosity of fluid, all as a result of the increased wall superheat. It must be Considered that natural convection is a result of density differences and is, therefore, most prominent at higher heat fluxes and low velocities.
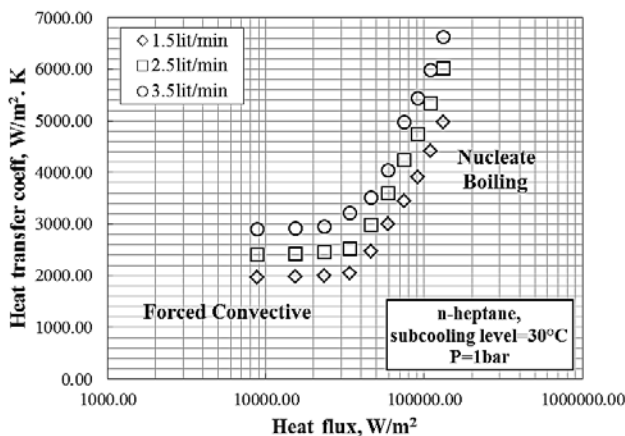
Figure 5. Forced convective and flow boiling heat transfer coefficient of n-heptane**.**
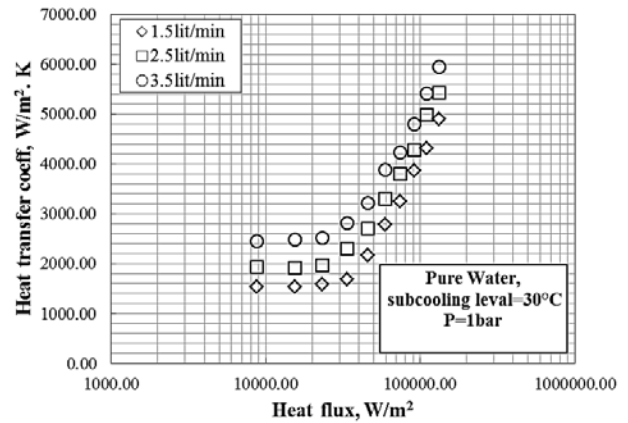
Figure 6. Forced convective and flow boiling heat transfer coefficient of water**.**

4.1.2 Effect of heat flux on visual bubble size

Many experiments have been performed to investigate the effect of heat flux on the bubble diameter. Visual recorded imagesdemonstrated that with increasing the heat flux (particularly at higher heat fluxes); the departure bubble diameter significantly increases over the different flow rates. In result of local vaporization inside the flow, amount of vapor that is captured inside the generated bubbles dramatically increases and subsequently, apparent size of bubbles increases. **Figures 7 (A-F)** depict the effect of heat flux on rate of bubble formation as well as the bubble diameter for n-heptane at different heat fluxes.

A   B

39
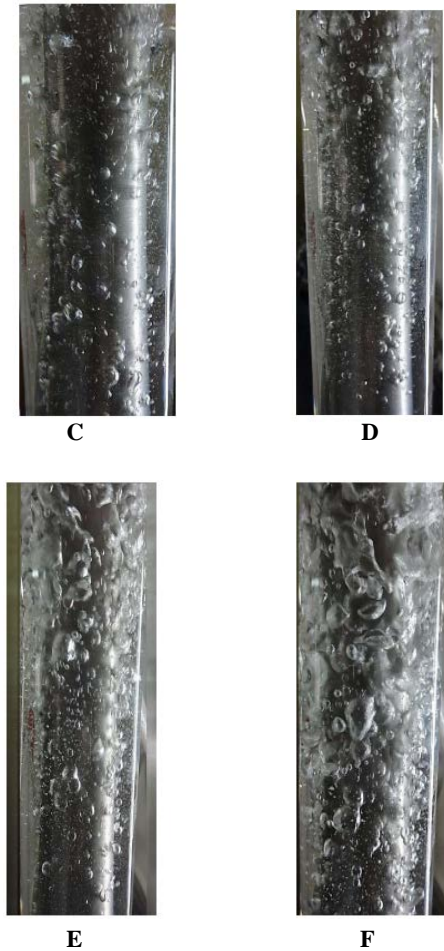
Figure 7. A: bubble formation at heat flux 45 kW/m²;
B: bubble formation at heat flux 54 kW/m²; **C:** bubble
formation at heat flux 63 kW/m²; **D:** bubble formation at heat
flux 91 kW/m²; **E:** bubble formation at heat flux 110 kW/m²;
F: bubble formation at heat flux 132 kW/m².

4.2 Effect of fluid flow rate

4.2.1 Effect of liquid flow rate on heat transfer coefficient

Liquid flow rate may be considered as a one of the most effective parameter on flow boiling heat transfer coefficient so that with increasing the flow rate of fluid, the flow boiling heat transfer coefficient dramatically increases for both of n-heptane and pure water at any conditions, although flow rate has insignificant influence on the Forced convective heat transfer but in contrast, significant effect of flow rate is clearly seen on the flow boiling heat transfer mechanism and subsequently flow boiling heat transfer coefficient. **Figure 8** indicates the influence of flow rate on the Forced convective and flow boiling heat transfer coefficient for n-heptane. As can be seen, the higher flow rate, the higher flow boiling heat transfer

coefficient is seen. Similar to n-heptane, for pure water the same condition can be seen and with increase of flow rate, higher flow boiling heat transfer coefficient is observed.
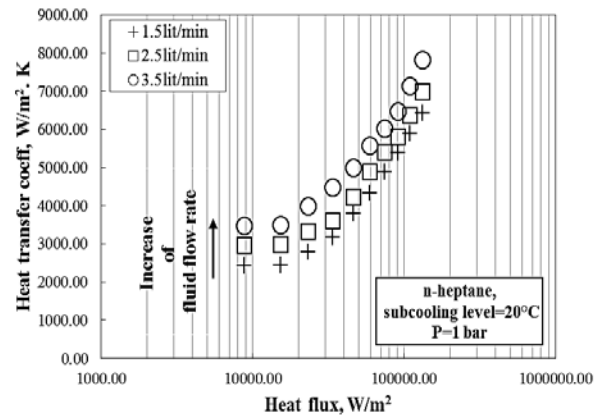
Figure 8. Effect of flow rate on flow boiling heat transfer coefficient of n-heptane (fordeionized water, similar condition is seen)**.**

4.2.2 Effect of fluid flow rate on bubble diameter

As can be seen in **Figure 9**, at lower flow rate, larger bubbles are observed at constant heat fluxes. It maybe occur due to the fact that the time needed for the growth of bubbles reduces at higher flow rates; therefore, bubbles are smaller than those observed at higher flow rates. Also, it is found that bubble diameter in water is smaller than that of n-heptane and frequency of bubble generation in water is greater than that of n-heptane. This point may lead to the postulation of lower boiling point for water than n-heptane which leads to more water turns to the vapor in comparison with n-heptane at particular, constant temperature.
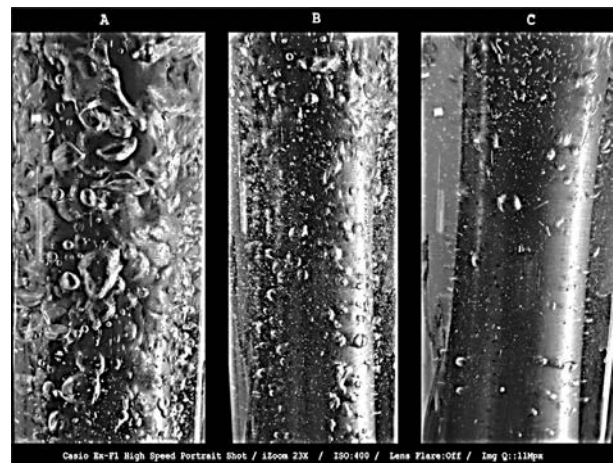
Figure 9. Effect of fluid flow rate on the bubble diameter in flow boiling of n-heptane at heat flux 85kW.m⁻²: A: Q=1.5lit/min, B: Q=2.5lit/min, C: Q=3.5lit/min**.**

4.3 Effect of subcooling level (inlet temperature)

4.3.1 Effect of subcooling level on the flow boiling heat transfer coefficient

Figure 10 demonstrates the effect of liquid subcooling on the heat transfer coefficients of water and n-heptane at constant flow rate. Results show that the subcooled flow boiling heat transfer coefficient of both fluids increases as the subcooling increases. This increase in heat transfer coefficient manifests itself especially at higher heat fluxes. Conversely, under forced convective heat transfer regime, the subcooling temperature does not have strong influences on the heat transfer coefficient[35].
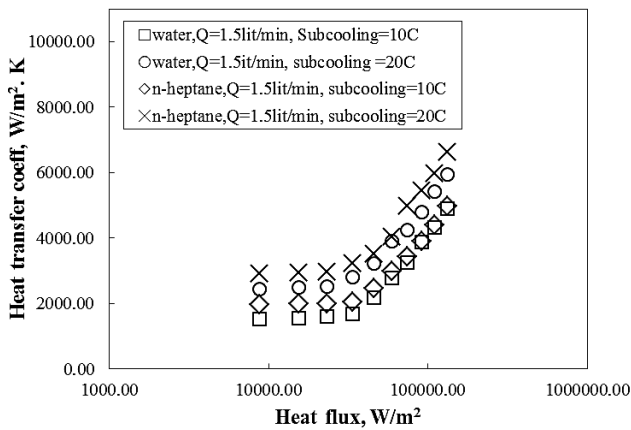
Figure 10. Comparison between heat transfer coefficient of flow boiling of n-heptane and water.

4.3.3 Effect of subcooling level on the bubble diameter

Many experiments were performed to find any correlation or rational relation between bubble diameter and subcooling level but they did not show any particular relationship between subcooling level and size of bubbles, however, more studies indicated that the only effect of subcooling level may be seen on the onset of nucleate boiling (ONB)

where the first bubble arises from the heating section. In fact, the boundary between forced convective and nucleate boiling zone is ONB. Experiments show that the higher subcooling level causes that ONB point moved forward toward the higher heat flux, which means that at higher heat flux the first bubble is formed and seen. Briefly speaking, the lower subcooling level, the lower inception heat flux may be seen. **Figure 11** shows the effect of subcooling level on inception heat flux and ONB for both water and n-heptane test fluids.
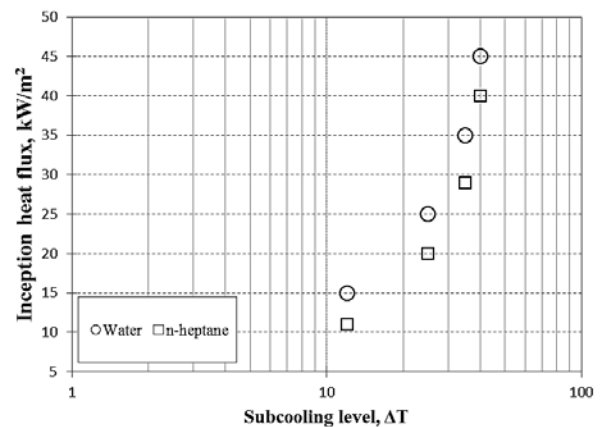
Figure 11. Influence of subcooling level on bubble characteristics.

4.4 Comparison of results with existing correlations

The obtained results may be used for engineering purposes[37-49]; therefore, these results must be compared with some well-known correlation to see how accurately these results are experimentally measured. The Chen model and Gungor-Winterton correlation are the ones of the most common used correlations used for predicting the flow boiling heat transfer coefficient. These correlations are given in **Table 3**.

41

No.	Author	Correlation
		$$\alpha_{fb} = S.\alpha_{nb} + F.\alpha_{fc}$$
1	Chen(1966)	$$F = \begin{cases} 1 & \text{if } \dfrac{1}{X_{tt}} \le 0.1 \\ 2.35\left(\dfrac{1}{X_{tt}} + 0.213\right)^{0.736} & \text{if } \dfrac{1}{X_{tt}} \ge 0.1 \end{cases}$$ $$S = \frac{1}{1 + 2.53 ? 0^{-6}N_{Re_{tp}}^{1.17}}$$ $$X_{tt} = \left(\frac{1-\dot{x}}{\dot{x}}\right)^{0.9}\left(\frac{\rho_v}{\rho_l}\right)^{0.5}\left(\frac{\mu_l}{\mu_v}\right)^{0.1}$$ $$\dot{x} = N_{Ph} - N_{Ph_n}\exp\left(\frac{N_{Ph}}{N_{Ph_n}} - 1\right)$$ $$N_{Ph} = \frac{h_v - h_{l,sat}}{h_{fg}}$$ $$N_{Ph_n} = \frac{-N_{Bo}}{\sqrt{\left(\dfrac{455}{N_{Pe_l}}\right)^2 + 0.0065^2}}$$
2	Gungor and Winterton(1986)	$$\alpha_{fb} = S.\alpha_{nb} + F.\alpha_{fc}$$ $$F = 1 + 24000N_{BO}^{1.16} + 1.23\left(\frac{1}{x_{tt}}\right)^{0.86}$$ $$\alpha_{nb} = 55P_r^{0.55}(-\log P_r)^{-0.55}M^{-0.5}q^{0.67}$$ The forced convective coefficient is calculated byDittus-Boelter

Figures (12-13) demonstrate the predicted results of flow boiling heat transfer coefficient of water and n-heptane using the Chen type model and Gungor-Winterton correlation. As can be seen, similar to our earlier work[38], results of Chen model are more reasonable when compared to Gungor-Winterton correlation. Besides, a deep look inside the both of figures demonstrates that for higher heat fluxes, both of correlations are unable to represent the good agreement between experimental results and those of obtained by the correlations. As seen, for Chen type model the Absolute Average Deviation of 20% is reported while it is about 30% for Gungor-Winterton correlation. Noticeably, Absolute Average Deviation is calculated using Eq. (12):

$$AAD\% = \frac{\alpha_{calculated} - \alpha_{experimental}}{\alpha_{experimental}} \times 100 \qquad (12)$$
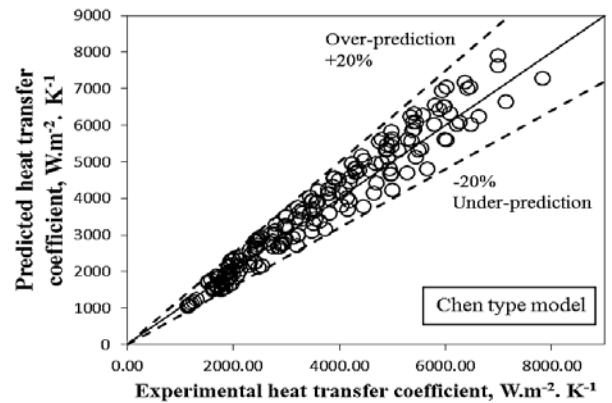
Figure 12. Results of comparison between experimental data and Chen type model.

42
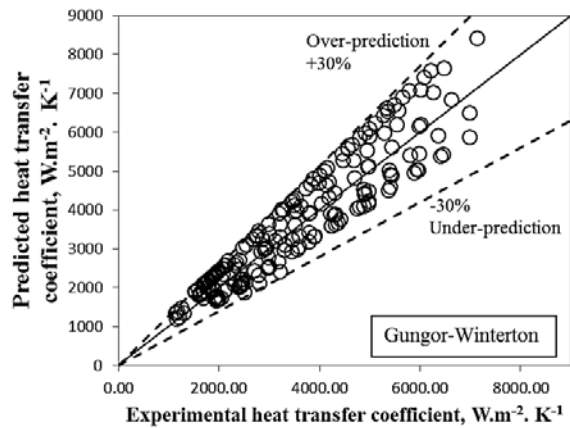
Figure 13. Results of comparison between experimental data and Gungor-Winterton correlation**.**

5. Conclusions

Experimental studies on flow boiling heat transfer coefficient of n-heptane and deionized-water were conducted. n-heptane after experiments is a plausible coolant almost identical to water. Investigations on the operating parameters showed that:

- Heat flux has an indispensible effect on the forced convective and nucleate flow boiling heat transfer regions such that with increasing the heat flux, heat transfer coefficient slightly, dramatically increases for forced convective, nucleate boiling regions respectively. Also with increasing the heat flux, rate of generated bubbles considerably increases.

- Flow rate of flow is also the other important operating parameters that with increasing the flow rate, heat transfer coefficient for forced convective and nucleate boiling regions dramatically increases. Also with increasing the flow rate, smaller bubbles are seen due to reduction of resident time of bubbles near the heating surface. Also increase of flow rate creates a chaotic flow which lead to bubbles to be collapsed near the surface and improve the convection currents which consequently enhances the heat transfer coefficient in nucleate boiling region.

- A rough comparison between results and available correlations showed that Chen type model predicts the experimental data with reasonable deviation of 20% which is 30% for Gungor-Winterton correlation.

Nomenclatures

A area, m^2

b distance, m

Bo boiling number

C_p heat capacity, $J.kg^{-1}.^{o}C^{-1}$

d_b bubble departing diameter, m

d_h hydraulic diameter, m

f fanning friction number

F enhancement factor

h enthalpy, $J. kg^{-1}$

ΔH_v heat of vaporization, $J.kg^{-1}$

k thermal conductivity, $W.m^{-1}.^{o}C^{-1}$

l_{th} heated length, m

L heater length, m

ΔL characteristic length in Eq. (15), m

Nu Nusselt number

Pe Peclet number

Ph phase change number

Pr reduced pressure

Pr Prandtl number

P pressure, Pa

q heat, W

Re Reynolds number

R_a roughness, m

s distance between thermometer location and heat transfer surface, m

S suppression factor

T temperature, K

x liquid mass or mole fraction

$\dot{x}$ vapour mass fraction

X_{tt} Martinelli parameter

y vapor mass or mole fraction

Subscripts-Superscripts

b bulk

c critical

fb flow boiling

in   inlet

out   outlet

l liquid

m mixture

n number of components

nb nucleate boiling

r reduced

Sat   saturated

th   thermometers

v   vapor

w   Wall

43

Greek symbols

α heat transfer coefficient, $W.m^{-2}.K^{-1}$

ρ density, $kg.m^{-3}$

μ viscosity, $kg.m^{-1}.s^{-1}$

Conflict of interest

The authors declare that they have no conflict of interest.

References

1. Zeitoun O. Subcooled flow boiling and condensation (Ph.D. Thesis). Canada: McMaster University; 1994.

2. Hewitt GF, Kersey HA, Lacey PMC, *et al*. Burnout and nucleation in climbing film flow. International Journal of Heat and Mass Transfer 1965; 8: 793–814.

3. Barbosa JR, Hewitt GF, Richardson SM. High-speed visualization of nucleate boiling in vertical annular flow. International Journal of Heat and Mass Transfer 2003; 46: 5153–5160.

4. You H, Sheikholeslami R, Doherty WOS. Flow boiling heat transfer of water and sugar solutions in an Annulus. Wiley Inter Science 2004; 50(6): 1119-1128.

5. Peyghambarzadeh SM, Vatani A, Jamialahmadi M. Application of asymptotic model for the prediction of fouling rate of calcium sulfate under sub-cooled flow boiling. Applied Thermal Engineering 2012; 39: 105-113.

6. Ahmadi R, Nouri-Borujerdi A, Jafari J, *et al*. Experimental study of onset of subcooled annular flow boiling. Progress in Nuclear Energy 2009; 51: 361–365.

7. Kew PA, Cornwell K. Correlations for the prediction of boiling heat transfer in small-diameter channels. Applied Thermal Engineering 1997; 17: 705–715.

8. Lin S, Kew PA, Cornwell K. Two-phase heat transfer to a refrigerant in a 1 mm diameter tube. International Journal of Refrigeration 2001; 24(1): 51–56.

9. Kandlikar SG, Grande WJ. Evolution of micro channel flow passages–Thermo hydraulic performance and fabrication technology. Heat Transfer Engineering 2003; 24(1): 3–17.

10. Kandlikar SG. Boiling heat transfer with binary mixtures; low boiling in plain tubes. Journal of Heat Transfer 1998; 120: 388–394.

11. Chen JC. A correlation for boiling heat transfer to saturated fluids inconvective flow. Industrial & Engineering Chemistry Process Design and Development 1966; 5(3): 322-329.

12. Bergles AE, Lienhard VJH, Kendall GE, *et al*. Boiling and evaporation in small diameter channels. Heat Transfer Engineering 2003; 24: 18–40.

13. Celata GP, Cumo M, Setaro T. Forced convective boiling in binary mixtures. International Journal of Heat and Mass Transfer 1993; 36(13): 3299–3309.

14. Guerrieri SA, Talty RD. Proposed correlation of data for two-phasecomponent flow in pipes. Chemical Engineering Progress Symposium Series 1956; 52: 69–77.

15. Chang YS, Kim MS. Performance and heat transfer characteristics of hydrocarbon refrigerants in a heat pump system. International Journal of Refrigeration 2000; 23: 232–242.

16. Sivagnanam P, Balakrishnan AR, Varma YBG. On the mechanism of subcooled flow boiling of binary mixtures. International Journal of Heat and Mass Transfer 1994; 37: 681–689.

17. Ose Y, Kunugi T. Development of a boiling and condensation model on subcooled boiling phenomena. Energy Procedia 2011; 9: 605–618.

18. Lima RJ, Quibén JM, Thome JR. Flow boiling in horizontal smooth tubes: New heat transfer results for R-134a at three saturation temperatures. Applied Thermal Engineering 2009; 29: 1289–1298.

19. Huo X, Chen L, Tian YS, *et al*. Flow boiling and flow regimes in small diameter tubes. Applied Thermal Engineering 2004; 24: 1225–1239.

20. Salari E, Peyghambarzadeh SM, Sarafraz MM, *et al*. Boiling thermal performance of TiO_2 aqueous nanofluids as a coolant on a disc copper block, Periodica Polytechnica. Chemical Engineering 2016; 60(2): 106.

21. Sarafraz MM. Nucleate pool boiling of aqueous solution of citric acid on a smoothed horizontal cylinder. Heat and Mass Transfer 2012; 48(4): 611–619.

22. Nakhjavani M, Nikkhah V, Sarafraz MM, *et al*. Green synthesis of silver nanoparticles using green tea leaves: Experimental study on the morphological, rheological and antibacterial behavior. Heat and Mass Transfer 2017; 53(10): 3201–3209.

23. Sarafraz M, Peyghambarzadeh S, Alavi Fazel S, *et al*. Nucleate pool boiling heat transfer of binary nano mixtures under atmospheric pressure around a smooth horizontal cylinder. Periodica Polytechnica: Chemical Engineering

2013; 57(1-2):71–77

24. Pourmehran O, Gorji TB, Gorji-Bandpy M, *et al*. Magnetic drug targeting through a realistic model of human tracheobronchial airways using computational fluid and particle dynamics. Biomechanics and Modeling in Mechanobiology 2016; 15(5): 1355–1374.

25. Zou X, Gong MQ, Chen GF, *et al*. Experimental study on saturated flow boiling heat transfer of R170/R290 mixtures in a horizontal tube. International Journal of Refrigeration 2010; 33: 371–380.

26. Lin PH, Fu BR, Chin Pan. Critical heat flux on flow boiling of methanol-water mixtures in a diverging micro-channel with artificial cavities. International Journal of Heat and Mass Transfer 2011; 54: 3156–3166.

27. Táboas F, Vallčs M, Bourouis M, *et al*. Assessment of boiling heat transfer and pressure drop correlations of ammonia/water mixture in a plate heat exchanger. International Journal of Refrigeration 2012; 35: 633–644.

28. Fernandez Seara J, Uhia FJ, Sieres J. Laboratory practices with the Wilson plot method. Experimental Heat Transfer 2007; 20: 123-135.

29. Kline SJ, McClintock FA. Describing uncertainties in single-sample experiments. Mechanical Engineering 1953; 75 (1): 3–12.

30. Joback KG. A unified approach to physical property estimation using multivariate statistical techniques (M.S. Thesis). Cambridge: Massachusetts Institute of Technology; 1984.

31. Spencer CF, Danner RP. Improved equation for prediction of saturated liquid density. Journal of Chemical & Engineering Data 1972; 17(2): 236–241.

32. Bruce E, Poling J, Prausnitz M, *et al*. The properties of gases and liquids, 5th ed. New York: The McGraw-Hill Companies; 2004. p. 10-11, 10-70.

33. Ruzicka V, Domalski ES. Estimation of the heat capacities of organic liquids as a function of temperature using group additives. Compounds of carbon, hydrogen, halogens, nitrogen, oxygen, and sulfur. Journal of Physical and Chemical Reference Data 1993; 22: 619–657.

34. Fernández-Seara J, Uhía FJ, Sieres J. Laboratory practices with the Wilsonplot method. Experimental Heat Transfer 2007; 20: 123–135.

35. Peyghambarzadeh SM, Sarafraz MM, Vaeli N, *et al*. Forced convective and subcooled flow boiling heat transfer to pure water and n-heptane in an annular heat exchanger. Annals of Nuclear Energy 2013; 53: 401–410.

36. Sarafraz MM, Peyghambarzadeh SM, Vaeli N. Subcooled flow boiling heat transfer of ethanol aqueous solutions in vertical annulus space. Chemical Industry & Chemical Engineering Quarterly 2012; 18(2): 315−327.

37. Sarafraz MM, Peyghambarzadeh SM. Experimental study on subcooled flow boiling heat transfer to water–diethylene glycol mixtures as a coolant inside a vertical annulus. Experimental Thermal and Fluid Science 2013; 50: 154–162.

38. Sarafraz MM, Peyghambarzadeh SM. Influence of thermodynamic models on the prediction of pool boiling heat transfer coefficient of dilute binary mixtures. International Communications in Heat and Mass Transfer 2012; 39(8): 1303–1310.

39. Biglarian M, Gorji MR, Pourmehran O, *et al*. H_2O based different nanofluids with unsteady condition and an external magnetic field on permeable channel heat transfer. International Journal of Hydrogen Energy 2017; 42 (34): 22005–22014.

40. Tabassum R, Mehmood R, Pourmehran O, *et al*. Impact of viscosity variation on oblique flow of Cu–H_2O nanofluid. Proceedings of the Institution of Mechanical Engineers, Part E: Journal of Process Mechanical Engineering 2017; 232(5): 622–631.

41. Sarafraz MM, Peyghambarzadeh SM, Nucleate pool boiling heat transfer to Al_2O_3-water and TiO2-water nanofluids on horizontal smooth tubes with dissimilar homogeneous materials. Chemical and Biochemical Engineering Quarterly 2012; 26 (3): 199-206.

42. Sarafraz MM, Peyghambarzadeh SM, Alavifazel SA. Enhancement of nucleate pool boiling heat transfer to dilute binary mixtures using endothermic chemical reactions around the smoothed horizontal cylinder. Heat and Mass Transfer 2012; 48 (10): 1755–1765.

43. Sarafraz MM, Hormozi F. Forced convective and nucleate flow boiling heat transfer to alumnia nanofluids. Periodica Polytechnica Chemical Engineering 2014; 58 (1): 37–46.

44. Sarafraz MM, Hormozi F, Silakhori M. *et al*. On the fouling formation of functionalized and non-functionalized carbon nanotube nano-fluids under pool boiling condition. Applied Thermal Engineering 2016; 95: 433–444.

45. Sarafraz MM. Experimental investigation on pool boiling heat transfer to formic acid, propanol and 2-butanol pure liquids under the atmospheric pressure. Journal of Applied Fluid

Mechanics 2013; 6 (1): 73–79.

46. Nakhjavani M, Nikkhah V, Sarafraz MM *et al*. Green synthesis of silver nanoparticles using green tea leaves: Experimental study on the morphological, rheological and antibacterial behavior. Heat and Mass Transfer 2017; 53 (10): 3201–3209.

47. Sarafraz MM, Nikkhah V, Madani SA, *et al*. Low-frequency vibration for fouling mitigation and intensification of thermal performance of a plate heat exchanger working with CuO/water nanofluid. Applied Thermal Engineering 2017; 121: 388–399.

48. Sarafraz MM, Hormozi F. Application of thermodynamic models to estimating the convective flow boiling heat transfer coefficient of mixtures. Experimental Thermal and Fluid Science 2014; 53: 70–85.

49. Sarafraz MM, Arya A, Nikkhah V. *et al*. Thermal performance and viscosity of biologically produced silver/coconut oil. Nanofluids Chemical and Biochemical Engineering Quarterly 2017; 30 (4): 489–500.

Original Research Article

Synthesis and characterization of nickel oxide and evaluation of its catalytic activities for degradation of methyl orange in aqueous medium

Muhammad Saeed[*], **Muhammad Amjed, Attaulhaq, Muhammad Usman, Shahid Adeel**

Department of Chemistry, Government College University Faisalabad, Faisalabad Pakistan. E-mail: msaeed@gcuf. edu.pk

ABSTRACT

This study focuses on synthesis of nickel oxide catalyst and exploration of its catalytic activities for degradation of methyl orange in aqueous medium. Nickel oxide was prepared sole-gel method using nickel nitrate haxahydrate and citric acid as precursor materials. X-ray diffractometry and scanning electron microscopy were used for characterization of prepared nickel oxide particles. The prepared particles were used as the catalysts for the degradation of Methyl Orange in aqueous medium. The effects of different parameters on degradation of methyl orange were investigated. The degradation of methyl orange followed the Eley-Rideal (E-R) mechanism. The apparent activation energies for degradation of methyl orange determined was found as 36.4 kJ/mol.

Keywords: Nickel Oxide; Methyl Orange; Degradation; Eley-Rideal Mechanism

1. Introduction

Metal based oxides have been investigated for several years, because these materials are widely used in many technological applications, such as electrochemistry, optical fibers, sensors, coating, and catalysis. Nickel is higher in abundance, economically feasible and suitable for a number of applications as compared to other metals. It exists in different form of oxides[1]. Oxides of nickel have gained much attention since these materials are important for many electrochemical systems especially alkaline systems like fuel cells, electrolyzers and batteries. These materials are also important due to low price, good stabilities and appreciable catalytic activities. These oxides are oxygen rich species in which Ni can exist in various oxidation states in addition to its normal oxidation state of 2+. NiO, $Ni(OH)_2$, $NiOOH$, NiO_2, Ni_2O_3 are different types of oxides of nickel[2,3]. NiO and $Ni(OH)_2$ have been used as an important electrode material in the field of energy storage, especially in super capacitors and lithium ion batteries. The energy storage capability is due to redox process occurring at the electrode/electrolyte interface. P-type and semiconductor nickel oxide thin films have been investigated for gas sensor, light emitting diodes (LED) and electrochromic devices[4–8]. These oxides can also be used as catalysts for different processes. In 1962, Nakagawa *et al.*,[9] reported the use of nickel oxides as useful oxidizing agent for oxidation of alcohols, amines, nitriles, phenols and sulfur compounds.

Konaka *et al.*[10] used nickel peroxide as catalyst for oxidation of diphenylacetonitrile and benzyl alcohol. Nickel peroxide was prepared from nickel sulfate and sodium hypochlorite. Similarly, in 1970s, Fleischmann and co-workers investigated the electrochemical oxidation of some organic compounds like carboxylic acids, ketones, amines, alcohols and nitriles at Ni anode in alkaline solution[11]. In present study nickel oxide particles prepared by sol-gel method were employed as catalysts for degradation of methyl orange in aqueous medium effectively.

2. Experimental

2.1 Preparation of nickel oxide

A solution of citric acid was prepared by dissolving 4.2 g of citric acid in 100 mL distilled water. Another solution of nickel nitrate hexahydrate, was prepared by dissolving 5.8 g of nickel nitrate hexahydrate in 100 mL distilled water. The solution of nickel nitrate hexahydrate was added dropwise into the solution of citric acid under constant stirring. Then, the mixture was heated up to 343 K until water evaporates which resulted in green gel. Finally, the gel was calcined at 673 K for 4 hours. After calcination black powder of nickel oxide was stored for further study.

2.2 Characterization

XRD analysis was carried out on X-Ray Diffractometer, JEOL (JDX-3532) Japan. SEM analysis was carried out with JSM-5910 Japan Scanning Electron Microscope.

2.3 Catalytic experiment

Nickel oxide catalyzed degradation experiments of methyl orange was carried out in a Prex glass beaker as batch reactor. For a typical run, the reactor was charged with 50 mL solution of known concentration. The temperature of the reaction mixture was kept constant at a desired value using hot plate while stirring the solution continuously. After stirring the solution for 30 minutes at desired temperature, 0.5 mL sample was taken to observe any variation in concentration of methyl orange during heating and stirring period. Then pre-determined amount of nickel catalyst was added

to reaction mixture and stirred continuously. At appropriate time intervals, 0.5 mL samples were taken from reactor. UV-Visible spectrophotometer (Shimadzu UV-160A, Japan) was used for analyses of reaction mixture. Percent degradation of dye was calculated using following equation.

$$Degradation(\%) = \frac{(R)_o - (R)_t}{(R)_o} (\times)100 \qquad \text{(Eq. 1)}$$

where $(R)_0$ and $(R)_t$ represent initial concentration and concentration of dye at various time intervals respectively.

3. Results and discussions

3.1 Characterization

Figure 1 shows XRD pattern of prepared nickel oxide. The XRD is dominated with intense and sharp peaks which shows the purity and crystallinity of prepared nickel oxide particles. Peaks appeared at $2\theta = 27°$, $40°$, $45°$, $53°$ and $57°$ are indexed to face-centered cubic structure (fcc) of NiO in accordance with the standard spectrum[12].
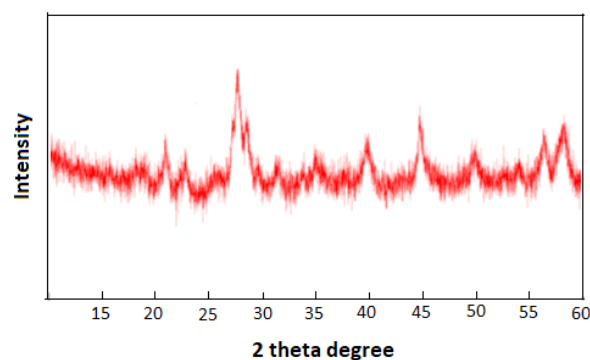
Figure 1. XRD pattern of prepared nickel oxide.
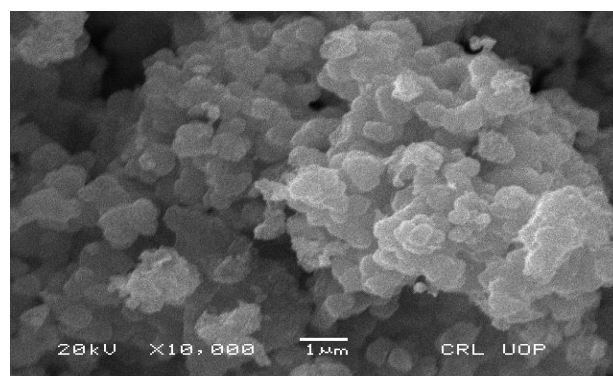
Figure 2. Scanning electron micrograph of prepared nickel oxide.

48

Figure 2 shows the scanning electron micrographs of prepared nickel oxide particles. The micrograph shows that particles are regular in morphology with spherical shape. It can also be concluded that particles are non-agglomerated and dispersed.

3.2 Catalytic degradation of methyl orange

To investigate the temperature effect on the degradation of methyl orange, reaction was carried out with initial concentration of methyl orange of 200 mg/L solution at temperature 313, 323 and 333 K separately. This effect was investigated by suspending 0.05 g of nickel oxide catalyst in 50 mL solution of methyl orange. Reaction mixture was stirred at speed of 500 rpm. 1 mL sample from the reaction mixture was withdrawn at regular intervals of 15, 30, 45, 60, 75, 90, 105 and 120 minutes. UV-visible spectrum of each sample was recorded. These absorbance values were used to determine the methyl orange concentration in reaction mixture at different time intervals using previously prepared calibration plot. The results revealed that degradation of methyl orange increases with temperature as given in **Figure 3**. It was noted that approximately 8, 10 and 15% of 200 mg/L methyl orange degraded in 15 minutes at 313, 323 and 333 K respectively. The degradation gradually increased to 45, 57 and 72% after 120 minutes of reaction time at 313, 323 and 333 K respectively.

Similarly, the effect of initial concentration of methyl orange was also investigated. For this purpose, separate experiments were performed at 323 K over 0.05 g of nickel oxide as catalyst with 100, 200 and 300 mg/L as initial concentration of methyl orange. Analysis of reaction samples taken from reactor at various interval of times confirmed that percent degradation of methyl orange decreases with increase in concentration as given in **Figure 4**. It was noted that approximately 7, 10 and 17% of methyl orange degraded in 15 minutes at with 300, 200 and 100 mg/L as initial concentration respectively. The degradation gradually increased to 55, 68 and 85% after 120 minutes of reaction time with 300, 200 and 100 mg/L as initial concentration respectively.

3.3 Kinetics analysis

For kinetics investigation, all the kinetics models were applied to time profile data for degradation of methyl orange as described in our previous study[13-17]. It was found that degradation of methyl orange follows pseudo 1st order kinetics expression according to Eley-Rideal (E-R)
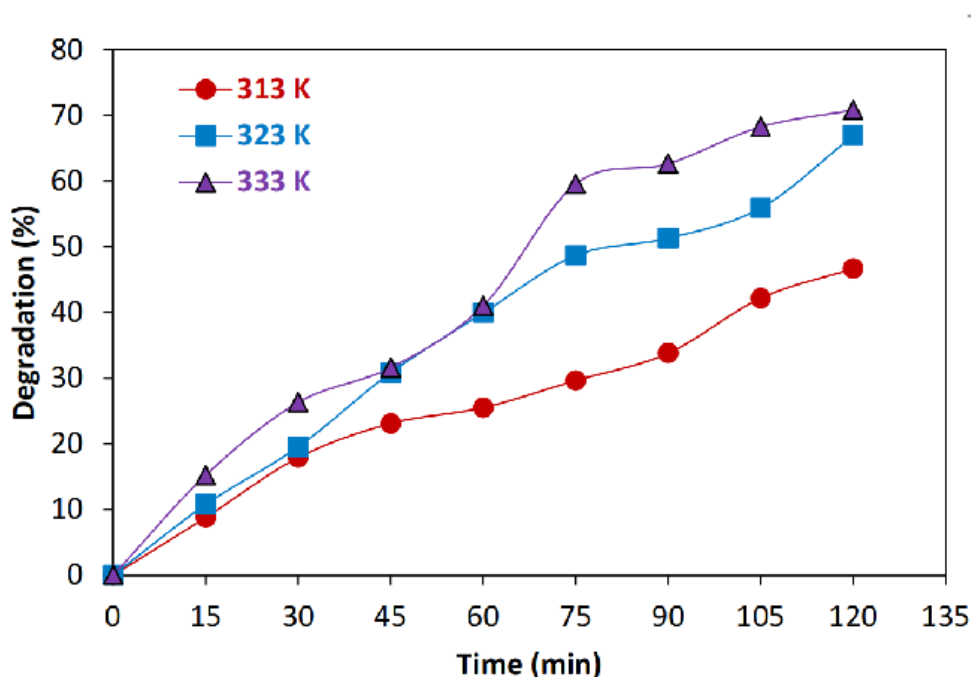
Figure 3. Time profile data of nickel oxide catalyzed degradation of methyl orange at various temperatures.
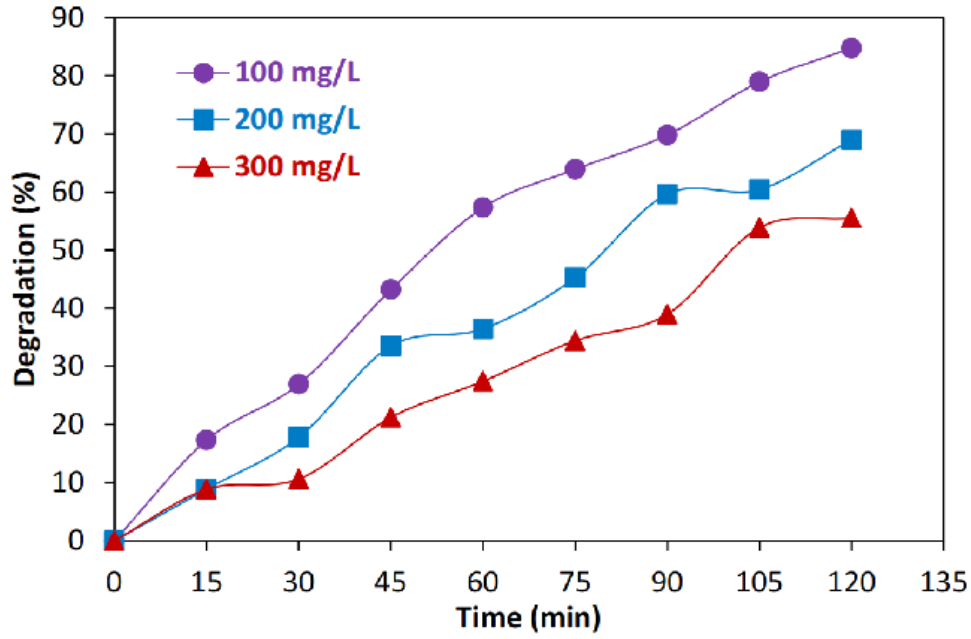
Figure 4. Time profile data of nickel oxide catalyzed degradation of methyl orange with various initial concentration.
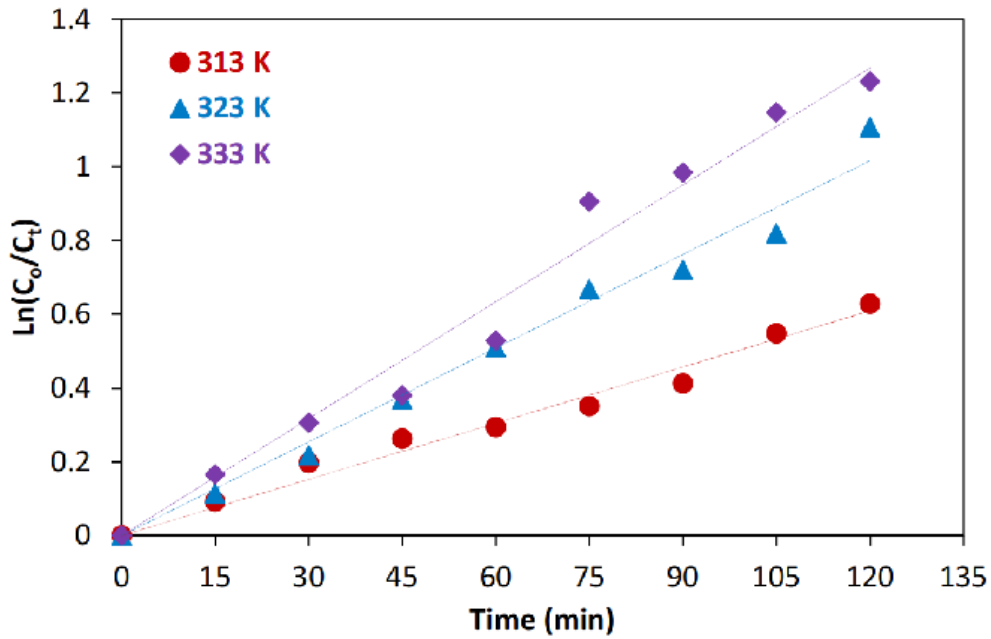
Figure 5. Application of kinetic expression (Eq. 4) to time profile data at various temperatures.

mechanism.

According to Eley-Rideal (E-R) mechanism, the rate expression can be given by Eq. 2.

$$-\frac{dC}{dt} = k_r \theta_{O2} [C] \qquad \text{(Eq. 2)}$$

where k_r, θ_{O2} and C represent the rate constant, surface of catalyst covered by oxygen and concentration of methyl orange respectively. As the

oxygen is constant, Eq.2 changes to Wq. 3 as below.

$$-\frac{dC}{dt} = k_{Ap} [C] \qquad \text{(Eq. 3)}$$

where k_{Ap} is apparent rate constant. On integration, Eq. 3 changes to Eq. 4, a straight-line equation.

$$ln \frac{C_o}{C_t} = k_{Ap} t \qquad \text{(Eq. 4)}$$

50

where C_o and C_t represent the initial concentration of methyl orange, concentration after time t respectively.

Eq. 4 was applied to time profile data at various temperatures as given in **Figure 5**. The slops of straight lines in **Figure 5** gives the apparent rate constants. The apparent rate constants were found as 0.0046, 0.0075 and 0.0105 per minute at 313, 323 and 333 K respectively. For determination of energy of activation, Arrhenius equation was applied to apparent rate constant at various temperatures. The energy of activation was calculated as 36.4 kJ/mol.

4. Conclusions

Nickel oxide which is eco-friendly as compared to commonly used catalysts was successfully synthesized and employed as effective catalyst for degradation of methyl orange in aqueous medium. About 71% of methyl orange solution was degraded in 120 minutes under ambient experimental conditions. The catalyst was heterogeneous in nature which could easily separate from reaction mixture. Catalytic degradation of methyl orange in present investigation followed Eley-Rideal mechanism. The apparent rate constants were found as 0.0046, 0.0075 and 0.0105 per minute at 313, 323 and 333 K respectively. The energy of activation was calculated as 36.4 kJ/mol.

Conflict of interest

The authors declare that they have no conflict of interest.

References

1. Jankovi´c B, Yevi´c A, Mentus S. The kinetic study of temperature-programmed reduction of nickel oxide in hydrogen atmosphere. Chemical Engineering Science 2008; 63: 567–575.
2. Ilyas M, Saeed M. Oxidation of benzyl alcohol in liquid phase catalyzed by oxides of nickel. Journal of the Chemical Society of Pakistan 2009; 31(4): 526–533.
3. Pacchioni G. Ab initio theory of point defects in oxide materials: Structure, properties, chemical reactivity. Solid State Sciences 2000; 2: 161–179.
4. Liang K, Tang X, Hu W. High-performance three-dimensional nanoporous NiO film as a supercapacitor electrode. Journal of Material Chemistry 2012; 22: 11062–11067.
5. Li X, Dhanabalan A, Wang C. Enhanced electrochemical performance of porous NiO–Ni nanocomposite anode for lithium ion batteries. Journal of Power Sources 2011; 196: 9625–9630.
6. Jena A, Munichandraiah N, Shivashankar SA. Carbonaceous nickel oxide nano-composites: As electrode materials in electrochemical capacitor applications. Journal of Power Sources 2013; 237: 156–166.
7. Fu X, Zhu Y, Xu Q, *et al.* Nickel oxyhydroxides with various oxidation states prepared by chemical oxidation of spherical β-Ni(OH)$_2$. Solid State Ionics 2007; 178: 987–993.
8. Soleimanpour AM, Jayatissa AH. Preparation of nanocrystalline nickel oxide thin films by sol–gel process for hydrogen sensor applications. Materials Science and Engineering C 2012; 32: 2230–2234.
9. Nakagawa K, Konaka R, Nakata T. Oxidation with nickel peroxide. I. oxidation of alcohols. Journal of Organic Chemistry 1962; 27(5): 1597–1601.
10. Konaka R, Terabe S, Kuruma K. Mechanism of the oxidation reaction with nickel peroxide. Journal of Organic Chemistry 1969; 34(5): 1334–1337.
11. Fleischmann M, Korinek K, Pletcher D. The kinetics and mechanism of the oxidation of amines and alcohols at oxide-covered nickel, silver, copper, and cobalt electrodes. Journal of Chemical Society PerkinTransaction 1972; 2: 1396–1403.
12. Atiq S, Javid M, Riaz S, *et al.* Magnetic phase transition in nickel oxide. Materials Today: Proceedings 2015; 2(10): 5262–5267.
13. Saeed M, Ilyas M, Siddique M. Kinetics of lab prepared manganese oxide catalyzed oxidation of benzyl alcohol in the liquid phase. International Journal of Chemical Kinetics 2015; 47(7): 447–460.
14. Saeed M, Ilyas M. Oxidative removal of phenol from water catalyzed by lab prepared nickel hydroxide. Applied Catalysis B Environmental

2013; 129(1): 247–254.

15. Saeed M, Ilyas M, Siddique M. Oxidative degradation of oxalic acid in aqueous medium using manganese oxide as catalyst at ambient temperature and pressure. Arabian Journal for Science & Engineering 2013; 38: 1739–1748.

16. Saeed M, Ilyas M, Siddique M. Oxidative degradation of phenol in aqueous medium catalyzed by lab prepared cobalt oxide. Journal of the Chemical Society of Pakistan 2012; 34(3): 626–633.

17. Saeed M, Adeel S, Ilyas M, *et al.* Oxidative degradation of methyl orange catalyzed by lab prepared nickel hydroxide in aqueous medium. Desalination and Water Treatment 2016; 57(27): 12804–12813.

Review Article

Ion-specific effects on equilibrium adsorption layers of ionic surfactants

Stoyan I. Karakashev

Department of Physical Chemistry, Sofia University, Sofia 1164, Bulgaria. E-mail: fhsk@chem.uni-sofia.bg

ABSTRACT

This review article reports the effect of the counter-ions on the ionic surfactant adsorption layer and its relation to the stability of foams and emulsions. The adsorption theory of Davies about the ionic surfactant monolayer was revisited and it is shown how to account for the type of the counter-ions. The experimental validation of this theory on thin liquid films was shown as well, thus explaining the effect of Hofmeister. However, their effect on foams and emulsions is more complex. Furthermore, it is shown how the counter-ions affect in complex way the stability of foams and emulsions via the surfactant adsorption layer in the light of the newest theory. To elucidate the nature of this effect, further investigation is called for.

Keywords: Ionic Surfactants; Ion Specific Effects; Effect of Hofmeister

1. Introduction

Hofmeister was the first to report how the solubility of the proteins depends on the added salt[1-7]. Hence, he established that some salts are stronger precipitators than other ones. He found out that both cations and anions act together but the effect of the anions is stronger. Thus, the anions and cations were ordered according to their precipitation ability:

Cations: $Li^+ < Na^+ < NH_4^+ < K^+ < Cs^+$

Anions: $OH^- < F^- < CH_3COO^- < Cl^- < Br^- < NO_3^- < I^- < ClO_4^-$

The ion sequence in the above series is independent of the protein, but their precipitation strength depends on the sign of the protein's net charge as well. Since that time, it was established that the salts precipitate in the same manner surfactants, colloidal particles and other more complex systems[8]. Evidently, the difference between the ionic parameters (size, polarizability, and ionization potential)[9] make them act differently on proteins, surfactants, colloidal particles, etc. A more detailed analysis on the effect of Hofmeister reveals that the ions adsorb on the surfaces of the colloids on different levels, thus affecting differently the interaction between the colloids (protein molecules, solid particles, surfactants, bubbles, oil droplet, etc.). For example, Ninham *et al.*[10-12] accounted for the van der Waals in teraction between inorganic ions and the bubble, thus determing concentration profiles of the different ions, but further met difficulties[13-15]. Tavares *et al.*[16] studied theoretically the Hofmeister effect on the interaction of charged proteins and established that van der Waals interaction causes strong attraction between the molecules. Warszynski *et al.*[17-19] and

Aratono *et al.*[20-22] clearly showed experimentally the specific effect of the counter-ions on the state of the adsorption layer of ionic surfactants, but Davies[23,24] and Borwankar and Wasan[25] showed the way for their theoretical interpretation. Later on Ivanov *et al.*[26-28], combined the approaches of Ninham[10-12] and Davies[23,24] to produce a relatively simple theory on the specific adsorption of counter-ions within adsorption layer of ionic surfactant. This theory accounts for KCl major factors controlling the ion specific adsorption: the ion polarizability and ionization potential, the radius of the hydrated ion and the possible deformation of the hydration shell upon ion adsorption at the interface. Ref.[29] successfully applied this theory to model disjoining pressure of thin liquid films, and emulsion stability between the film surface. We will present here after the basis of this theory along with its attempt to predict the foam and emulsion stability.

2. Ion-specific effects on the adsorption layers of ionic surfactants from dilute solutions

2.1. Adsorption in the absence of ion specific effects

It is well-known that adsorption Γ_{0s} of nonionic surfactant with concentration C_s in scarce adsorption layer is described by Henry adsorption isotherm:

$$\Gamma_{0s} = K_s C_s \tag{1}$$

Accordingly, the Henry equation of state is as following:

$$\sigma = \sigma_0 - RT\Gamma_{0s} \tag{2}$$

Where, σ and σ_0 are the surface tensions of the surfactant solution and the solvent, R and T are the gas constant and temperature.

If we assume that the adsorption layer becomes ionized equation (1) gets the form:

$$\Gamma_{0s} = K_s C_s exp\left(-\frac{F\Psi_{0s}}{RT}\right) \tag{3}$$

Where, F and ψ_{0s} are the Farady constant and the surface potential of the adsorption layer with excluded counter-ions.

Next, we regard the Poisson-Boltzmann equation in rectangular reference of state along the axis z:

$$\varepsilon\varepsilon_0 \frac{d^2\Psi_{0s}}{dz^2} = -\sum_i z_i F C_{0i} exp\left(\frac{-z_i F\Psi}{RT}\right) \tag{4}$$

Where, z_i is valency of the ion of species i, and ε and ε_0 are dielectric permitivities of the aqueous medium and the free space, while C_{0i} is the electrolyte concentration of type i.

In this equation, the variables Ψ and $d\Psi/dz = -E$ (electric field) can be separated, by using the identity $2d^2\Psi/dz^2 = d(E^2)/d\Psi$. This leads to:

$$d(E^2) = -\frac{2}{\varepsilon\varepsilon_0}\sum_i F z_i C_{0i} exp\left(\frac{-z_i F\Psi}{RT}\right)d\Psi \tag{5}$$

A first integral of the Poisson-Boltzmann equation is obtained by integrating equation (5) in limits $z = \infty$ to z, using as a first boundary condition $E = 0$ and $\Psi = 0$ at $z = \infty$:

$$E(z^2) = \frac{2RT}{\varepsilon\varepsilon_0}\sum_i C_{0i}\left[exp\left(\frac{-z_i F\Psi}{RT}\right) - 1\right] \tag{6}$$

The second boundary condition (at $z = 0$) is the electro neutrality condition:

$$\varepsilon\varepsilon_0 E|_{s=0} = F\Gamma_{0s} \tag{7}$$

We will denote the surface potential $\Psi(0)$ by Ψ_{0s}. Setting $z = 0$, Ψ and Ψ_{0s} into equation (6), and eliminating $E(z = 0)$ from the electroneutrality condition (7), the Gouy equation is obtained:

$$\frac{k_0^2}{4}\Gamma_{0s}^2 = \sum_i C_{0i}\left[exp\left(\frac{-z_i F\Psi_{0s}}{RT} - 1\right)\right] \tag{8}$$

Here,

$$k_0^2 \equiv \frac{2F^2}{\varepsilon\varepsilon_0 RT} \tag{9}$$

Equation (9) is the concentration independent part of Debye parameter: $k^2 = k_0^2 C_t$. In the case of 1:1 electrolyte, Gouy's equation (7) simplifies to:

$$\frac{k_0}{4}\Gamma_{0s} = \sqrt{C_t}sinh\left(\frac{\Phi_{0s}}{2}\right) \tag{10}$$

Here, C_t is the total electrolyte concentration (in units [m^{-3}]) and

$$\Phi_{0s} = \frac{F\Psi_{0s}}{RT} \tag{11}$$

is the dimensionless positively defined surface potential. At high surface potentials ($\Phi_s \gg 1$), a good approximation of Gouy equation (10) is:

$$\Gamma_{0s} = \frac{2}{k_0}\sqrt{C_t}exp\left(\frac{\Phi_{0s}}{2}\right) \tag{12}$$

The ion distribution in the electrical double layer depends on the local potential $\Phi(z)$. Hence, the ion adsorption Γ_i^{DL} of any ion i in the diffuse layer can be calculated by using Gibbs definition of adsorption as an excess:

$$\Gamma_i^{DL} \equiv C_{0i}\int_0^\infty[exp(-z_i\Phi(z)) - 1]dz \tag{13}$$

Where, the superscript "*DL*" indicates counter-ions, co-ions and surfactant ions in the diffuse layer only. Generally, the total surfactant adsorption

is a sum of Γ_i^{DL} and the surface concentration Γ_s (adsorption in the adsorption layer). The surfactant ions in the diffuse layer are repelled by the interface since they have the same charge and the surface potential Φ_s is enough high. Hence, the surfactant concentration in the diffuse layer tends to zero and can be neglected. The same refers to the co-ions. Therefore, only the adsorption of the counter-ions in the diffuse layer is important. In order to calculate the integrals defined by equation (13), it is convenient to change the integration variable to Φ, by using the relation $dz = d\Phi/(d\Phi/dz)$, and neglecting the co-ions in DL, equation (13) can be reduced to:

$$\Gamma_i^{DL} \equiv C_{0i} \int_{\Phi_s}^0 \frac{[exp(\Phi(z))-1]}{d\Phi/dz} d\Phi \qquad (14)$$

By using Poisson-Boltzmann equation (4) to obtain expression for $d\Phi/dz$:

$$\frac{d\Phi(z)}{dz} = -k_0\sqrt{C_t}[exp(\Phi(z)) - exp(-\Phi(z))] \quad (15)$$

One can obtain explicit expression for the adsorptions Γ_i^{DL}:

$$\Gamma_i^{DL} = \frac{2C_{0i}}{k_0\sqrt{C_t}}\left[exp\left(\frac{\Phi_{0s}}{2}\right) - 1\right] \xrightarrow{\Phi_{0s}\to\infty} \frac{2C_{0i}}{k_0\sqrt{C_t}} exp\left(\frac{\Phi_{0s}}{2}\right) \qquad (16)$$

To calculate the surface tension, the Gibbs isotherm is used. If only one counterion of concentration C_{0i} is present in the system, and the bulk solution is assumed ideal, one has:

$$d\sigma = -RT\Gamma_s dlnC_s - RT\Gamma_i^{DL} dlnC_{0i} \qquad (17)$$

For high surface potential, one has $\Gamma_i^{DL} = \Gamma_s$. Then, the Gibbs isotherm (17) simplifies to:

$$d\sigma = -2RT\Gamma_s dlnC \qquad (18)$$

Where, C is the mean ionic activity of the surfactant[30,31], defined by:

$$C = C_s^{1/2} C_i^{1/2} \qquad (19)$$

If the solution is not ideal, the mean ionic activity C in equation (19) will include activity coefficient:

$$C = \gamma C_s^{1/2} C_i^{1/2} \qquad (20)$$

Meanwhile, the combination of equations (3) (Henry adsorption isotherm for ionic surfactants) and (12) (Gouy equation) produce the following important relation[23,28]:

$$3\Phi_{0s} = ln\frac{\kappa_0^2 K_s^2}{4} + ln\frac{C_s^2}{C_t} = 6ln\frac{\kappa_0 K_0}{2} + ln\frac{C_s^2}{C_t} \qquad (21)$$

Equation (21) shows that the surface potential Φ_s increases with C_s and K_s (due to the increased adsorption) and decreases with the total electrolyte concentration C_t (due to the additional screening effect of the electrolyte on the surface charge). Inserting back, the surface potential (21) into the isotherm (3), one obtains a generalization of Henry isotherm for adsorption of ionic surfactants:

$$\Gamma_{0s} = K_0 C^{2/3} \qquad (22)$$

Where, C is given by equation (19), and K_0 is adsorption constant of the ionic surfactant. It is related to Henry constant K_s:

$$K_0 = (4K_s/\kappa_0^2)^{1/3} \qquad (23)$$

The fact is that, according to equation (22), Γ_s depends only on the mean ionic activity. C is an explicit formulation of what is known as salting out effect on ionic surfactant adsorption[31]. Equation (22) has been first derived and confirmed by experimental data for $C_nH_{2n+1}SO_4Na$ at air/water interface by Davies[23]. We will refer to it as Davies isotherm. By using the procedure of Borwankar and Wasan[25], and Ivanov et al. derived equation (22) and obtained the explicit expression (23) for K_0. According to equation (23), K_0 should not depend on the electrolyte concentration, at least for moderate concentrations. Substituting equation (22) in the Gibbs isotherm (18) and integrating, one obtains Davies equation of state[32]:

$$\sigma = \sigma_0 - 3RTK_0 C^{2/3} \qquad (24)$$

Equation (24) does not account for the specific effect of the counter-ions. Hence, according to this equation, if the counter-ion of one ionic surfactant is replaced by another counter-ion, its surface activity will not change. The latter controversies to the experimental data[33]. For this reason, the real equilibrium adsorption constant K, in which the specific adsorption of counter-ions is accounted for, has been modelled[26] by the following relation:

$$K = K_0 exp\left(-\frac{u_0}{2k_BT}\right) \qquad (25)$$

Where, k_B is the Boltzmann constant, and u_0 is the specific adsorption energy of the surfactant's counter-ion.

2.2. Adsorption in the presence of ion-specific effects

To account for the specific adsorption of the counter-ions into the surfactant adsorption layer, one should account for the correction, which they cause to the electric potential in the Poisson-Boltzmann equation:

$$\varepsilon\varepsilon_0 \frac{d^2\Phi}{dz^2} = -\sum_i z_i F C_{0i} exp\left[-z_i\Phi(z) - \left(\frac{u_i(z)}{k_BT}\right)\right] \quad (26)$$

Where, $u_i(z)$ is the specific interaction between the ion and the interface[26,28] given by the relation:

$$u_i(z) = \frac{R_i^3}{(R_i+z)^3}u_{i0}. \quad (27)$$

Here, R_i is the ionic radius and u_{i0} is the van der Waals energy of an ion in the plane $z = 0$ situated at distance R_i from the interface as shown in **Figure 1**. This equation can be integrated by analogy with the derivation of Gouy equation (10), by using $2d^2\Phi/dz^2 = d(E^2)/d\Phi$ and Gauss condition (7):

$$F^2\Gamma_{0s}^2 = -2\varepsilon\varepsilon_0 \sum_i z_i F C_{0i} exp\left(-\frac{u_{i0}}{k_BT}\right)$$
$$\int_0^{\Phi_{0s}} exp[-z_i\Phi(z)]exp\left[-\frac{u_i(z)-u_{i0}}{k_BT}\right]d\Phi \quad (28)$$
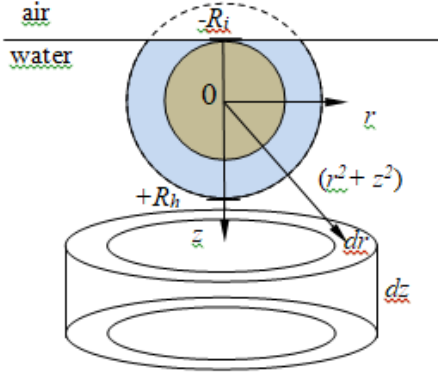
Figure 1. Illustration of the integration procedure applied to derive the energy of interaction of surface ion with the whole bulk of water[26].

At high surface potentials, only the counterions need to be taken into account in the sum in the right-hand side of this equation. This approximation is of crucial importance for this theory to simplify all following calculations. It can be used also in the case of ionized proteins and polymers as well, but not for the adsorption of simple electrolytes. In such a case, both cations and anions have comparable participation in the diffuse layer, whose local potential depends, in fact, on the small difference of their local concentrations. With this approximation, the integrals in the right hand side of equation (28) can be reduced to a generalized Gouy equation, accounting for the ion specific effect:

$$\Gamma_{0s}^2 = \frac{4}{k_0^2}\sum_i C_{0i} exp\left(-\frac{u_{i0}}{k_BT}\right)exp(\Phi_{0S}) \quad (29)$$

Where, k_0 is the Debye parameter which is given by equation (9), and Φ_{0s} is surface potential of adsorption layer situated on the phase boundary, not containing counter-ions. If only one counter-ion is

present in the system, equation (29) simplifies to:

$$\Gamma_{0s}^2 = \frac{4}{k_0^2} C_t exp\left(-\frac{u_{i0}}{k_BT}\right)exp(\Phi_{0S}) \quad (30)$$

Substituting here, the expression for Φ_{0s}, equation (23), one obtains expression of Davies adsorption isotherm (22), $\Gamma_{s0} = K_0C^{2/3}$, accounting for ion specific interactions:

$$\Gamma_{0s} = K_0 exp\left(-\frac{u_{i0}}{2k_BT}\right)C^{2/3} \equiv KC^{2/3} \quad (31)$$

Here, C is the mean activity. Therefore, one can obtain the following expression for the equilibrium adsorption constant accounting for the ion-specific effects:

$$K = K_0 exp\left(-\frac{u_{i0}}{2k_BT}\right) = \left(\frac{4K_s}{k_0^2}\right)^{1/3} exp\left(-\frac{u_{i0}}{2k_BT}\right) \quad (32)$$

This procedure allows also the determination of the first iteration for the real surface potential Φ_s. To do so, the equation of state (3) is used, with Γ_s given by equation (31). After solving the result with respect to Φ_s, one obtains:

$$\Phi_s = \frac{1}{3}ln\frac{k_0^2 K_s^2}{4} - \frac{1}{3}ln\frac{C_s^2}{C_t} + \frac{u_{i0}}{2k_BT} \quad (33)$$

Considering the above equations, one can obtain the following relations:

$$\Gamma_s = \Gamma_{0s}exp\left(-\frac{u_{i0}}{2k_BT}\right), \quad \Phi_s = \Phi_{0s}+\frac{u_{i0}}{2k_BT} \quad (34)$$

Where, Γ_s and Γ_{0s} are surfactant adsorption containing and not containing counter-ions, and Φ_s and Φ_{0s} dimensionless surface potentials containing and not containing correction from the adsorption of counter-ions. Hence, equation (24) gets the form:

$$\sigma = \sigma_0 - 3RTKC^{2/3} \quad (35)$$

Equation (35) is valid for liquid expanded state of the adsorption layer, which is medium term level of occupation of the latter. Moreover, the constant σ_0 is not anymore the surface tension of the solvent (water), but cohesion constant.

The next step is modelling the specific adsorption energy u_{i0} of the counter-ions onto the air/water interface.

2.3 Theory on adsorption of ions on the air/water interface

The adsorption of inorganic ion on the air/water interface may seem inappropriate at first glance due to the image repulsion[34], but one should account for the displaced surface water molecules by the adsorbed inorganic ion. The latter can make this adsorption energetically favorable. For this reason, the effect of Ray-Jones[35] appears at

small salt concentrations (up to 0.1 M).
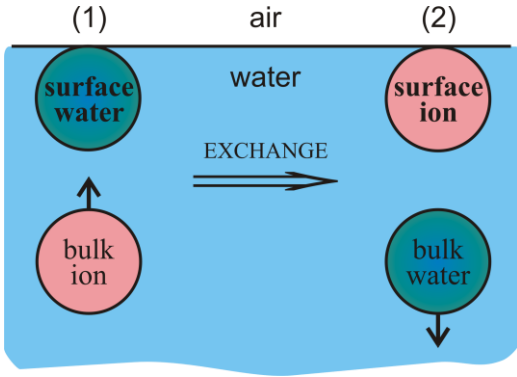
Figure 2. Energetical states prior and after the adsorption of ion on air/water interface.

We assume that one ion displaces N_w water molecules from the air/water interface, and the latter dive into the bulk. Shown in **Figure 2** are the energetical states 1 and 2 of the adsorption of inorganic ion on the air/water interface. Energetical state 1 consists of inorganic ion in the bulk and N_w water molecules at the air/water interface. Both of them interact with the whole bulk of water molecules. Energetical state 2 consists of inorganic ion at the air/water interface and the displaced N_w water molecules being already into the bulk. Again both of them interact with the whole bulk of water molecules. The energy of the very process is the difference between the energies of the two states:

$$u_0 = \left(u_{iw}^s + u_{ww}^b\right) - \left(u_{iw}^b + u_{ww}^s\right) = \Delta u_i - \Delta u_w \qquad (36)$$

Where, u_{iw}^s is the energy of interaction of the surface ion with the whole bulk of water, u_{ww}^b is the energy of interaction of N_w water molecules located in the bulk with the whole bulk of water molecules, u_{iw}^b is the energy of interaction of one inorganic ion located in the bulk with the whole bulk of water, u_{ww}^s is the energy of interaction of N_w water molecules located on the air/water interface with the whole bulk of water, Δu_i is the difference between energetical states of ion on the surface referred to the bulk, and finally Δu_i is the difference of the energetical states of N_w water molecules on the surface referred to the bulk. To calculate the specific energy of adsorption u_0 of one ion on the air/water interface, one needs to calculate each of the above mentioned quantities[26,28]. Moreover, a special accent[26,30] is put on the compressibility of the hydration shells – there are certain ions,

called kosmotrops[36,37] (or structure making, e.g. Li^+, Na^+, F^-), whose hydration shell does not deform upon their adsorption on the air/water interface, while the hydration shells of all the other ions called chaotrops[36,37] (or structure breaking, e.g. K^+, Cl^-, Br^-, NO_3^-, etc.), redistribute in such a way during their adsorption on the air/water interface that the upper part (toward air) of the ion becomes bare, while the lower part (toward the bulk) becomes over-occupied with hydrated water molecules (see **Figure 3**). The calculation of the energy u_{i0} was performed, using the London expression for the intermolecular potential u_{ij} between molecules of type i and j at a distance r_{ij}[34]:

$$u_{ij} = -L_{ij}/r_{ij}^6 \qquad (37)$$

Where, the London constant L_{ij} is related to the static polarizabilities $\alpha_{p,i}$ and $\alpha_{p,j}$ and the ionization potentials I_i and I_j of the interacting species:

$$L_{ij} = \frac{3\alpha_{p,i}\alpha_{p,j}}{2} \frac{I_i I_j}{I_i + I_j} \qquad (38)$$
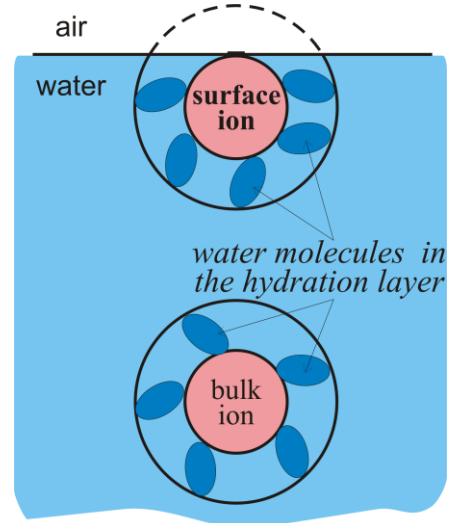
Figure 3. Redistribution of the hydration shell during the adsorption of ion on the air/water interface. Reprinted with permission from ref.[26]. Copyright 2007 Elsevier.

We will calculate first the energy of interaction u_i^s of the chaotropic type of ions situated on the air/water interface with the whole bulk of water. Toward this aim, the London potential (36) is integrated over the volume of the water phase excluding the hydration shell, with r_{ij} being the distance between the volume element dr and the ion positioned at $r = 0$, $z = 0$ (that is, the integration is over $z > -R_b$ and $r^2 + z^2 < R_h^2$). The integration is performed in cylindrical coordinates (see **Figure 1**):

$$u_i^S = -\int_{-R_b}^{R_h}\int_{\sqrt{R_h^2-z^2}}^{\infty}\frac{L_{iw}\rho_w 2\pi r dr dz}{(r^2+z^2)^3}$$

$$-\int_{R_h}^{\infty}\int_0^{\infty}\frac{L_{iw}\rho_w 2\pi r dr dz}{(r^2+z^2)^3} = -\frac{2\pi}{3}\frac{L_{iw}\rho_w}{R_h^3}\left(1+\frac{3}{4}\frac{R_b}{R_h}\right) \quad (39)$$

Here, ρ_w is the particle density of water. Similarly, the energy u_i^B of interaction of ion located in the bulk with the whole bulk of water (integration in spherical coordinates):

$$u_i^B = -\int_{R_h}^{\infty}\frac{L_{iw}}{r_w^6}\rho_w 4\pi r_{iw}^2 dr_{iw} = -\frac{4\pi}{3}\frac{L_{iw}\rho_w}{R_h^3} \quad (40)$$

The respective energies of the ensemble of water molecules (assumed a sphere of radius R_h, or a part of it) are:

$$u_w^S = -\frac{2\pi}{3}\frac{L_{ww}\rho_w}{R_h^3}\left(1+\frac{3}{4}\frac{R_b}{R_h}\right)$$

$$u_w^B = -\frac{4\pi}{3}\frac{L_{ww}\rho_w}{R_h^3} \quad (41)$$

Substituting equations (39)-(41) into the expression (34) for u_{i0}, one obtains an explicit relation of the adsorption energy of the chaotropic ions (called here ions of type I):

$$u_{i0} = \left(1-\frac{3}{4}\frac{R_b}{R_h}\right)\frac{2\pi}{3}\frac{\rho_w}{R_h^3}(L_{iw}-L_{ww}) \quad (42)$$

To calculate u_{i0} for the kosmotrops (called here ions of type II), one must set $R_h = R_b$ in equation, which simplifies the expression to:

$$u_{i0} = \frac{\pi}{6}\frac{\rho_w}{R_h^3}(L_{iw}-L_{ww}) \quad (43)$$
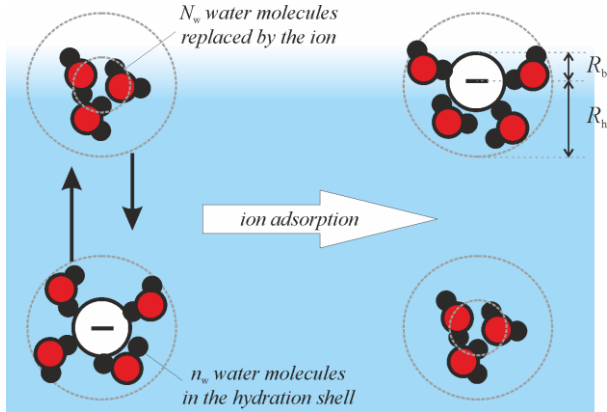
Figure 4. Scheme of the process of adsorption of a type I ion. Left: ion in the bulk. Right: ion at the surface. The n_w hydrating water molecules might be pushed away by the interface, so that the shortest distance of approach of the ion to the interface is the bare ion radius R_b. Upon adsorption, the ion replaces an ensemble of N_w water molecules. For type II ions, the shortest distance of approach of the ion to the interface is the hydrated ion radius R_h.

For monovalent ions, Marcus[38] found that the hydration number n_w of the ions can be represented by the empirical relation:

$$n_w = A_v/R_i \quad (44)$$

Where, $A_v = 3.6$ Å for all ions. He further as-

sumed that the hydrating n_w water molecules, considered as spheres with radius $R_w = 1.38$ Å and volume $v_w = 11$ Å^3, are squeezed around the ion, forming a layer of thickness $R_h - R_b$ and volume:

$$n_w v_w = \frac{4\pi}{3}\left(R_h^3 - R_b^3\right) \quad (45)$$

The last relation can be used to calculate R_h. The values of n_w and R_h calculated in this way[26,38,39] are shown in **Table 1**. Robinson and Stokes[30] used similar approach, but with water molecular volume $v_w = 30$ Å^3, which follows from the density of water. They also used different values of the hydration number n_w, which were calculated from the ion diffusivity.

The London constants L_{iw} for the interaction ion-water molecule, and L_{ww} for the interaction of N_w water molecules with a single water molecule are calculated directly from equation:

$$L_{iw} = \frac{3\alpha_{p,i}\alpha_{p,j}}{2}\frac{I_i I_w}{I_i+I_w}$$

$$L_{ww} = \frac{3}{4}N_w\alpha_{p,w}^2 I_w \quad (46)$$

For the calculation of L_{ww}, the ensemble of N_w water molecules is regarded as a sphere with polarizability $N_w\alpha_{p,w}$[26]. The number N_w was assumed equal to the ratio between the volume of the bare ion and the volume of one water molecule[40]:

$$N_w = R_b^3/R_w^3 \quad (47)$$

Where, R_w is the radius of the water molecule. For the value of R_w, two possibilities were tested in Ref.[26]: (i) the average volume per molecule (30 Å^3), based on the water density, yields $R_w = 1.93$ Å; and (ii) the proper volume of a water molecule, 11 Å^3, corresponds to $R_w = 1.38$ Å. Better agreement with the experimental data was obtained with the second option, $R_w = 1.38$ Å. The used value of the static polarizability of water was $\alpha_{p,w} = 1.48$ Å^3 and of the ionization potential was $I_w = 2.02\times10^{-18}$ J[41].

For the cations, we used the second ionization potential, since the first one corresponds to ionization of the respective atom, not ion. Since the anions have already accepted one extra electron, their ionization potential must be equal to the negative value of the electron affinity.

Table 1. Specific adsorption energies of the considered ions (T = 25°C)

cation	R_b [Å]	n_w Eq. (66)	R_h [Å] Eq. (67)	N_w Eq. (69)	L_{ww} Eq. (68) [m⁶J] ×10⁸⁰	$α_{p,i}$ [Å³]	I_i [J] ×10¹⁸	L_{wi} Eq. (68) [m⁶J] ×10⁸⁰	u_{i0}/k_BT type I Eq. (64)	u_{i0}/k_BT type II Eq. (65)
Li⁺	0.69[1]	5.22	2.41	0.13	41.5	0.03[1]	12.1[2]	11.5		–0.09
Na⁺	1.02[1]	3.53	2.18	0.40	134	0.15[3]	7.58[2]	53.1		–0.33
NH₄⁺	1.53[4]	2.35	2.14	1.36	453	1.64[1]	2.13[2]	378	–0.61	
K⁺	1.41[1]	2.55	2.12	1.07	354	0.79[3]	5.07[2]	253	–0.90	
Rb⁺	1.65[5]	2.18	2.17	1.71	568	1.4[1]	4.41[2]	431	–0.98	
NMe₄⁺	2.80[1]	1.29	2.94	8.36	2770	9.08[1]	2.43[2]	2220	–1.05	

anion	R_b [Å]	n_w	R_h [Å]	N_w	L_{ww} [m⁶J] ×10⁸⁰	$α_{p,i}$ [Å³]	I_i [J] ×10¹⁸	L_{wi} Eq. (68) [m⁶J] ×10⁸⁰	u_{i0}/k_BT type I	u_{i0}/k_BT type II
Ac⁻	1.65[1]	2.18	2.17	1.71	568	5.50[1]	0.544[1]	545		–0.185
OH⁻	1.33[1]	2.71	2.11	0.90	297	2.04[1]	0.345[1]	134		–0.736
F⁻	1.33[1]	2.71	2.11	0.90	297	1.04[2]	0.545[1]	99.1		–0.891
Cl⁻	1.64[1]	2.20	2.17	1.68	557	3.59[2]	0.580[1]	359	–1.43	
Br⁻	1.95[1]	1.85	2.31	2.82	937	5.07[2]	0.540[1]	480	–2.32	
NO₃⁻	2.00[1]	1.80	2.33	3.05	1010	3.93[1]	0.631[1]	420	–2.83	
N₃⁻	1.95[1]	1.85	2.31	2.82	937	4.45[1]	0.444[1]	360	–2.93	
ClO₄⁻	2.40[1]	1.50	2.61	5.26	1750	5.25[2]	0.758[1]	642	–3.28	
BF₄⁻	2.30[1]	1.57	2.53	4.63	1540	2.80[1]	0.902[1]	388	–3.84	

Note: R_b – bare ion radius; n_w – hydration number, Eq. (44); R_h – hydrated ion radius, Eq. (45); N_w – number of water molecules in the ensemble, replaced by the ion upon adsorption, Eq. (47); L_{ww} – London constant of this ensemble, Eq. (46); $α_{p,i}$ – polarizability of the ion; I_i – second ionization potential of the cations and negative electron affinity of the anions; u_{i0} – ion specific adsorption energy, Eq. (42) for type I ions (no deformation of the hydration shell) and Eq. (43) for type II ions (with deformation of the hydration shell). The ions in the Table are ordered by increasing absolute values of u_{i0}. The sequence of both cations and anions is the same as in Hofmeister series, but for the cations this order corresponds to increasing efficiency as opposite to the series. Source data: [1]Marcus[38]; [2]Nikolskij[41]; [3]Tavares[16]; [4]Dietrich[42]; [5]Lide[43]

3. Comparison with experiment

3.1. Experimental verification of the theory of K

Experiment on surface tension isotherms of 0.5 mM sodium dodecyl sulfate (SDS)[44] at varying excess concentration of LiCl, NaCl and KCl showed significant differences due to the specific adsorptions of Li⁺, Na⁺, and K⁺ counter-ions.
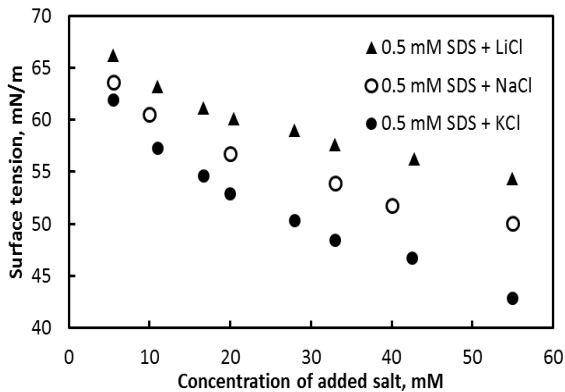
Figure 5. Surface tension isotherms of 0.5 mM SDS + added salts; The relative experimental error is ±0.2 mN/m.

The first experimental check will be the linearity of equation (35). We present hereafter the three adsorption isotherms in the scale of equation (35) and in CGS system. The concentration is converted in activity as well. The mean concentration is converted in mean activity.
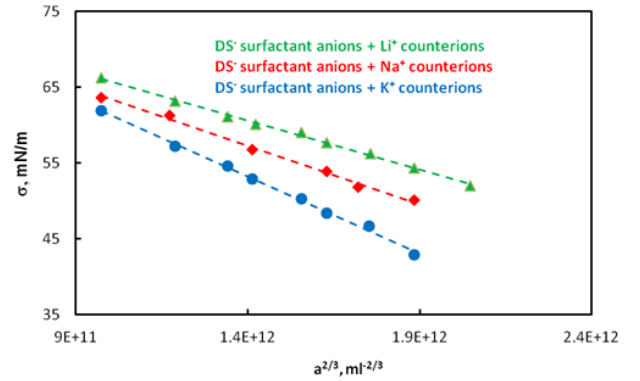
Figure 6. Surface tension isotherms of 0.5 mM SDS + added salts; The relative experimental error is ±0.2 mN/m.

One can see that **Figure 6** shows linear dependencies of the surface tension on the mean activity on 2/3 power ($a^{2/3}$). Therefore, equation (35) ($σ = σ_0 - 3RTKC^{2/3}$) is validated by the experiment. Moreover, one can calculate the equilibrium adsorption constants K for each of the cases from the slope (see equation (35)). Furthermore, equation (32) can be presented in the form:

$$lnK = lnK_0 - \frac{u_0}{2k_BT} \qquad (48)$$

As far as the equilibrium adsorption constant K can be obtained experimentally by means of equa-

tion (35) and experimental surface tension isotherm, and u_0/k_BT can be calculated independently by means of equations (42) and (43) (see **Table 1**), lnK can be presented as a function of u_0/k_BT. **Figure 7** shows that lnK depends linearly on the specific adsorption energy of the counterions u_0/k_BT and the slope is close to ½, which is of validation of equation (48).
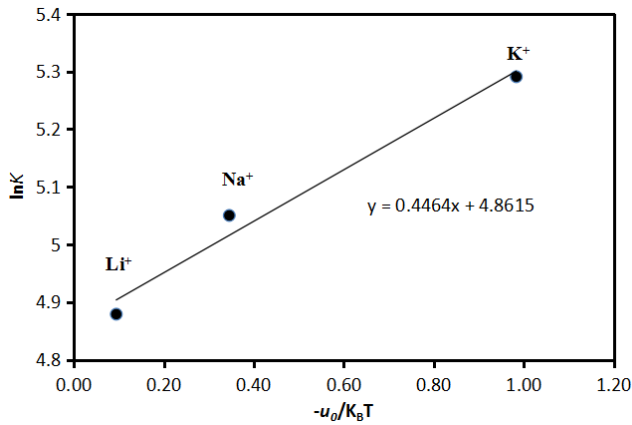
Figure 7. lnK as a function of $-u_0/k_BT$ for the cases SDS + LiCl, SDS + NaCl and SDS + KCl. In all of the cases the salt is added in great excess.
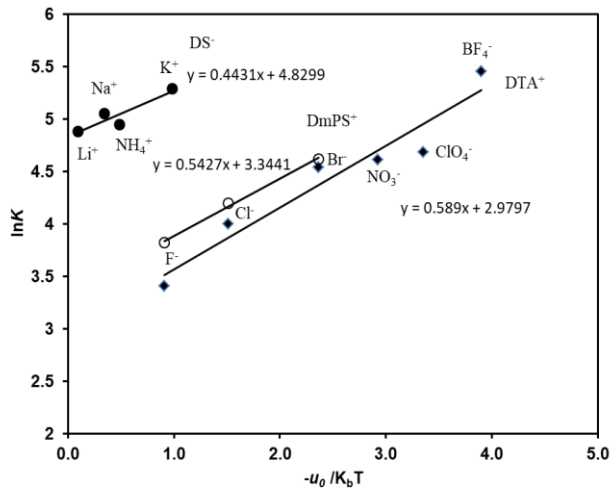
Figure 8. lnK as a function of $-u_0/k_BT$ for the cases (1) SDS + LiCl, SDS + NaCl, SDS + NH₄Cl, SDS + KCl; (2) DmPSCl + NaF, DmPSCl + NaCl, and DmPSCl + NaBr; and (3) DTAB + NaF, DTAB + NaCl, DTAB + NaNO₃, DTAB + NaClO₄, and DTABF₄ [28].

Shown in **Figure 8** is presented lnK vs. $-u_0/k_BT$ for three types of surface active ions in presence of different counter-ions. In all of the cases, the slope of the line is close to ½, which validates well the presented above theory. The main question remaining is if this theory can predict the stability of dispersed systems.

3.2 Ion-specific effects on the stability of dispersed systems and relation to state of the adsorption layer[29,44]

3.2.1 Ion-specific effects on thin films and emulsions

The ion-specific effects on the state of the adsorbed surfactant layer influence the stability of foams and emulsions. This section is devoted to the investigation of the type of the surfactants counter-ion on the stability of the dispersed systems. It presents the experimental data of Ref.[29] and such one conducted in the present work.

Ref.[29] presents experimental data on the disjoining pressure of water films in air (foam films) stabilized by 1 mM solutions of hexadecyltrimethylammonium bromide ($C_{16}H_{33}NMe_3Br$) and 9 mM added salt (NaF, NaCl, NaBr).

The disjoining pressure, stabilizing the films, was measured on a thin film pressure balance by using the Mysels-Jones porous plate technique (see **Figure 9**).
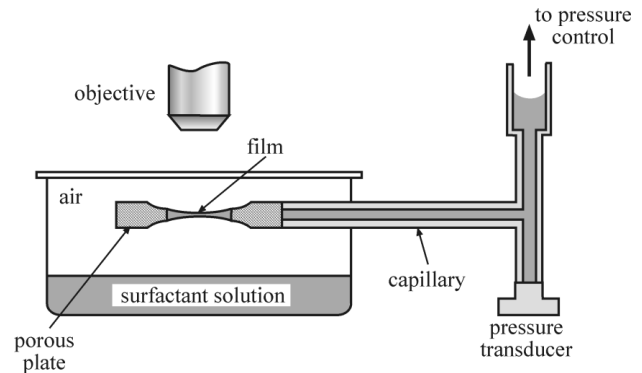
Figure 9. Schematic presentation of the porous plate cell.

The main question, which we raise, is how the type of the counter-ions affects the stability of foams and emulsions. We know from the previous sections that the counter-ions with a higher absolute value of the specific adsorption on air/water or oil/water interfaces are integrated onto the surfactant adsorption layer in larger degree and vice versa. Hence, at a higher level of counter-ion adsorption, the surface potential should be decreased more and vice versa. The theory of the electrostatic disjoining pressure has been developed by many authors, above all by Derjaguin and associates. Their results are summarized in the excellent book of Churaev *et al.*[45]. According to their theory (neglecting the ion specific effects), the electrostatic disjoining pres-

sure, Π_{el}, in a planar film of low surface potential or large thickness is given by the following expression:

$$\Pi_{el} = 64k_BTC_t\tanh^2\left(\frac{\Phi_{0S}}{4}\right)\exp(-\kappa h) = \Pi_0 exp(-\kappa h) \qquad (49)$$

Where, C_t is total salt concentration, κ is the Debye constant, $\kappa = \sqrt{2F^2C_1/RT\varepsilon\varepsilon_0}$ and h is the thicknss of the thin liquid film. Since during the derivation of equation (49) in Ref.[45], no other assumptions about the surface potential were done, we decided that in order to account for the specific effects, it should be sufficient merely to replace Φ_{0s} with Φ_s by means of the following equation:

$$\Phi_s = \Phi_{0s} + \frac{u_0}{2k_BT} \qquad (50)$$

Equation (49) suggests that the dependence of the experimental disjoining pressure Π on the thickness h should be close to linear in coordinating with $ln\,\Pi$ vs. h. **Figure 10** shows that indeed this is the case. Since the films are rather thick, one can disregard the contribution of the van der Waals disjoining pressure (direct numerical calculations confirmed this). This permits identifying Π with Π_{el} and using equation (49) for the calculation of Π, but with Φ_s replacing Φ_{s0}. The lines in **Figure 10** are almost parallel and obey the equation.

$$ln\Pi_{el} = ln\Pi_0 - \kappa h \qquad (51)$$

The obtained intercepts $ln\Pi_0$ and slopes κ are shown in **Table 2.**
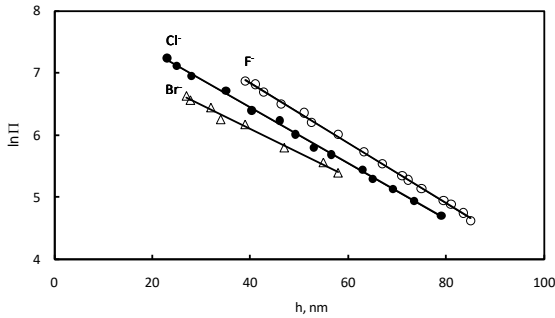
Figure 10. Plot of $ln\Pi$ vs. h for foam films stabilized with $C_{16}H_{33}NMe_3Br$ and NaX (X = F⁻, Cl⁻, Br⁻).

Table 2. Intercepts, $ln\Pi_0$, and slopes, κ, of the lines in **Figure 10**.

Ion	F⁻	Cl⁻	Br⁻
$ln\Pi_0$ [Pa]	8.79	8.25	7.65
κ [nm⁻¹]	0.0485	0.0451	0.0386

The almost parallel, but shifted, lines suggest that the specific ion interactions (if any) are affected

mostly the surface potential Φ_s. By means of equation (49), we calculated the experimental values of Φ_s from the obtained data for Π_0 (see **Table 3**) and plotted in **Figure 11** the results as Φ_s vs. $-u_0/k_BT$. The relatively good linearity and close value of the experimental slope, 0.4, to the theoretical one, ½, (cf. Equation (50)) seem to confirm the role of the ion specific effect.
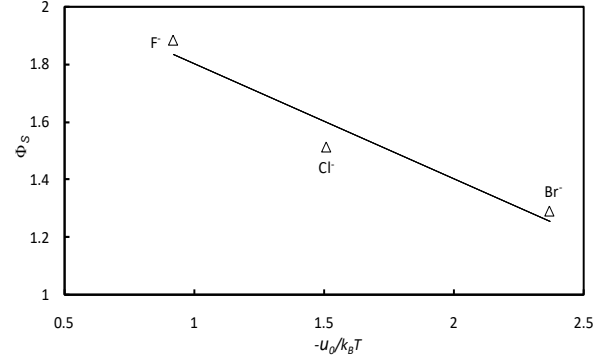
Figure 11. Combined surface potential Φ_s vs. $-u_0/k_BT$ for foam films stabilized with $C_{16}H_{33}NMe_3Br$ + NaX (X = F⁻, Cl⁻, Br⁻). The slope is –0.4.

The Hofmeister effect on the surface potential and the disjoining pressure, Π, is by no means negligible. To estimate it for films closer to reality, in **Figure 12,** we present the results (obtained in Ref.[26]) for the total disjoining pressure Π_{total} (including also the van der Waals contribution with Hamaker constant $A_H = 4\times10^{-20}$ J) of foam films with 0.5 mM of the halide counter-ions. The maxima of $\Pi(h)$ around $h = 5$ nm control the stability and the coalescence of the bubbles. The maximum is more than 4 times lower in the presence of only 0.5 mM Br than it would have been with the same electrolyte concentration if the ion specific effects were disregarded.
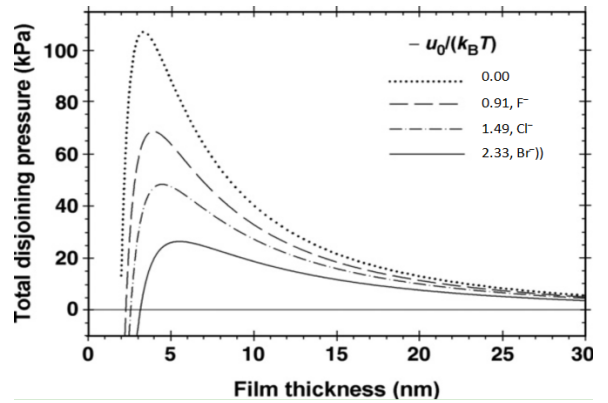
Figure 12. Total disjoining pressure Π_{total} calculated with Hamaker constant $A_H = 4\times10^{-20}$ J for 0.5 mM counterions F⁻, Cl⁻ and Br⁻ (from Ref.[26]).

Ref.[29] reports the emulsion stability measured by means of two types of techniques – Film Trapping Technique (FTT) and Centrifugation. They used the same surfactant ($C_{16}H_{33}NMe_3Br$) and salts (NaF, NaCl or NaBr). The concentrations of the surfactant and the added salts for FTT were the same as in the thin film studies described here above, but for the centrifugation, the emulsions with 1 mM salts were too unstable, so that the concentrations of the added salts were increased to 30 mM. Soybean oil, purified by passing it through a glass column filled with Silicagel 60 adsorbent, was used as oil phase.

The film trapping technique (FTT), developed in Refs.[46-49] is a useful method for determining the coalescence stability of single emulsion drops. The principle of the FTT is as following: A vertical capillary, partially filled with oil, is held at a small distance above the flat bottom of a glass vessel, **Figure 13**. The lower edge of the capillary is immersed in the working solution, which contains dispersed micron-size oil drops. The capillary is connected to a pressure control system, which allows one to vary and to measure precisely the difference, ΔP_A, between the air pressure in the capillary, P_A, and the atmospheric pressure, P_A^0. The pressure is measured by a pressure transducer connected to a personal computer. Upon the increase of P_A, the oil-water meniscus in the capillary moves downward against the substrate. When the distance between the oil-water meniscus and the glass substrate becomes smaller than the drop diameter, some of the drops remain entrapped in the formed glass-water-oil layer. The pressure P_A is increased until the coalescence of the entrapped oil drops with the upper oil phase is observed. The capillary pressure in the moment of drop coalescence, P_C^{CR}, represents the coalescence barrier and is called critical capillary pressure. It is related to ΔP_A in the moment of drop breakage and can be calculated from the equation:

$$P_C^{CR} = \Delta P_A - \Delta P_{OIL} - \rho g z \tag{52}$$

Where, ΔP_{OIL} is the pressure that jumps across the oil column in the capillary. It includes contributions from the hydrostatic pressure of the oil column and the capillary pressure of the air/oil meniscus. It is measured after filling the FTT capillary

with oil, but before immersing the capillary into the water pool. In the hydrostatic term, z is the depth of the water (see **Figure 13**), ρ is the water mass density and g is gravity acceleration. The trapped oil drops and the coalescence process were observed from above with an optical microscope.
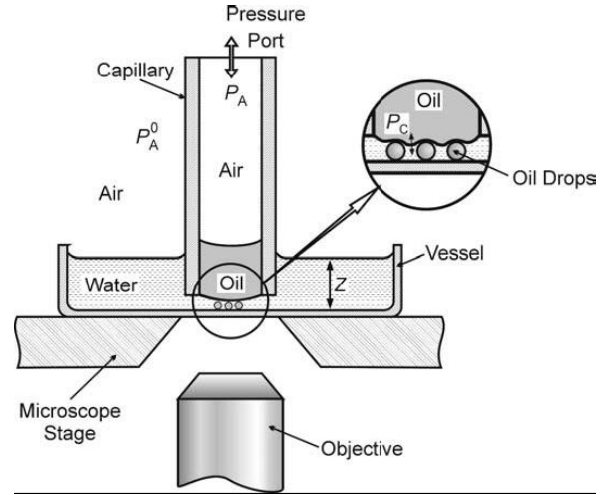
Figure 13. Scheme of the film trapping apparatus and of the droplets trapped between the oil-water and the substrate (see the magnification lens), from Ref.[49].

The test of the emulsion stability by means of centrifugation is described in details in Ref.[29]. Oil-in water emulsions were prepared by stirring for 4 min a mixture of 40 mL water phase and 10 mL soybean oil (20 vol. % SBO) with a rotor-stator homogenizer, Ultra Turrax T25 (Janke & Kunkel GmbH & Co, IKA-Labortechnik), operating at 13 500 rpm. The drop size d_{32} was determined by optical microscopy of specimens of the studied emulsions in transmitting light with a microscope. After 30 min storage, the fresh emulsions were transferred into several centrifugal tubes and centrifuged at 25 °C in 3K15 centrifuge. The emulsion stability is characterized by the critical osmotic pressure, P_{OSM}^{CR}, at which a continuous oil layer is released at the top of the emulsion cream in the centrifuge tube. P_{OSM}^{CR} is calculated from the experimental data by using the equation:

$$P_{OSM}^{CR} = \Delta \rho\, g_k (V^{OIL} - V^{REL})/A$$
$$= \Delta \rho g_k (H^{OIL} - H^{REL}) \tag{53}$$

Where, $\Delta \rho$ is the difference between the mass densities of the aqueous and the oil phases; g_k is the centrifugal acceleration ($g_k = L\omega^2$, where L is the distance between the axis of rotation and the center of the cream, ω is the angular velocity); V_{OIL} is the total volume of oil used for preparation of the

emulsion; V_{REL} is the volume of released oil at the end of centrifugation; and A is the cross-sectional area of the centrifuge test tube.

The results from both tests are presented in **Table 3** and **Figure 14**.

Table 3. Critical pressures and drop sizes of SBO-in-water emulsions, stabilized with 1 mM $C_{16}H_{33}NMe_3Br$ with added NaF, NaCl and NaBr

C_t [mM]	C_s [mM]	C_{el} [mM]	Electrolyte	d_{32} [m]	FTT, P_C^{CR} [Pa]	Centrifuge, P_{OSM}^{CR} [Pa]
10	1	9	NaF	25.2	360	-
10	1	9	NaCl	28.5	1100	-
10	1	9	NaBr	27.0	1320	-
31	1	30	NaF	20.7	-	360
31	1	30	NaCl	22.4	-	640
31	1	30	NaBr	21.5	-	917

The systems parameters and the measured values of the critical pressures P_C^{CR} and P_{OSM}^{CR} are tabulated in **Table 3** and plotted in **Figure 14** as P_C^{CR} (solid line) and P_{OSM}^{CR} (dashed line) vs. $-u_0/k_BT$. These critical pressures are proportional to Π and the higher their values are, the more stable the emulsions.

We do not dispose of enough information to carry out the same detailed analysis of these phenomena as we did with the electrostatic disjoining pressure. For example, we have no idea what the film thickness is; it is not quite clear whether a planar film forms or how much the disjoining pressure is affected by the curvature of the very small drops — these effects make problematic the calculation of the electrostatic disjoining pressure by means of equation (49). Still, some qualitative conclusions are possible. The linear dependence of P_C^{CR} and P_{OSM}^{CR} on $-u_0/k_BT$ confirms the presence of specific effects. However, instead of decreasing with the increase of $-u_0/k_BT$ (as the electrostatic disjoining pressure does), the critical pressures are increasing. Therefore, the electrostatic disjoining pressure Π_{all} is not the repulsive pressure to be overcome in order for the coalescence to occur. But then, what is the reason for the ion specific effect, demonstrated in **Figure 14**? It is not possible to answer with certitude this question without detailed studies of the phenomena accompanying the coalescence process. Nevertheless, we dare suggesting a hypothesis. The role of the specific effect of the counter-ions is twofold. On one side, it decreases the height of the

maxima of the disjoining pressure (see **Figure 15**), thus, making easier for the thin film to avoid the electrostatic repulsive pressure and from thin to thinner (metastable) Newton black film, where another, short range repulsive disjoining pressure (most probably steric or osmotic) might be operative.
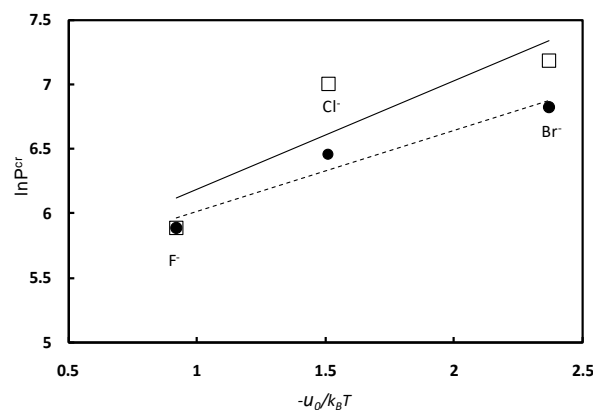
Figure 14. Critical pressures P_C^{CR} (by FTT, solid line) and P_{OSM}^{CR} (by centrifugation, dashed line) vs. $-u_0/k_BT$ of oil-in-water emulsions stabilized by $C_{16}H_{33}NMe_3Br$ + NaX (X = F$^-$, Cl$^-$, Br$^-$). ($\square$) P_{OSM}^{CR} of oil-in-water emulsion films stabilized by 10^{-3} M $C_{16}H_{33}NMe_3Br$ + 9×10^{-3} M NaX (X = F$^-$, Cl$^-$, Br$^-$) obtained by FTT (slope = 0.85); ($\bullet$) P_C^{CR} of oil-in-water emulsion films stabilized by 10^{-3} M $C_{16}H_{33}NMe_3Br$ + 3×10^{-2} M NaX (X = F$^-$, Cl$^-$, Br$^-$) obtained by centrifuge (slope = 0.63).
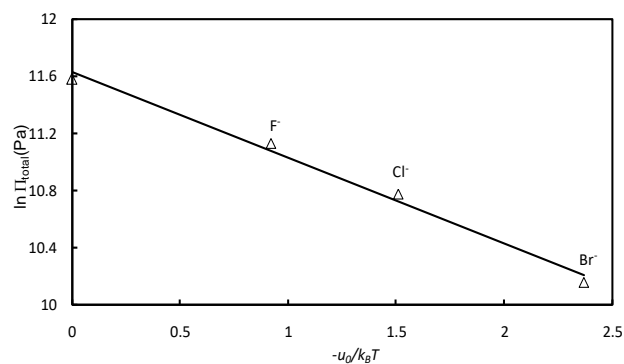
Figure 15. Total disjoining pressure Π_{total} in the maxima in **Figure 12** vs. $-u_0/k_BT$. This is in fact the coalescence barrier, according to DLVO theory.

It must be overcome for the thin film to rupture. On the other side, no matter what the nature of this disjoining pressure is, it must increase with the surfactant adsorption, Γ. However, unlike the electrostatic disjoining pressure, the surfactant adsorption, Γ, increases (for a given bulk surfactant concentration) with $-u_0/k_BT$. This brings us to the second role of the ion specific effects – it is to increase the short range repulsive pressure created by the surfactant, thus stabilizing the thin film. This ex-

plains why the slopes of the lines in **Figure 14** are positive. They should have been negative if only the electrostatic disjoining pressure Π_{el} were stabilizing the film. To support this opinion in **Figure 15**, we have plotted the maxima of Π_{total} from **Figure 12** (which are in fact the coalescence barriers), vs. $-u_0/k_B T$ indeed, the slope is negative. This means that the short range repulsive pressure involved in the stability of the emulsion drops is not directly related to ion specific effects. The theoretical and experimental verification of this hypothesis is feasible, but it is time consuming and beyond the scope of this paper.

3.2.2 Ion-specific effects on foams

We have established that the stability of the emulsions increases upon enhancing the specific adsorption energy of the counter-ions. This tendency was not expected.

For this reason, we were challenged to investigate this scientific "intrigue" deeper. We have chosen another system – foam stabilized by sodium dodecyl sulfate (SDS) and LiCl, NaCl and KCl as salts, which were meant to be added in an amount significantly exceeding this one of the surfactant.

We clearly showed hereafter that the electrostatic repulsion between the bubbles, which is controlled by the added counter-ions, is only one of the factors contributing to foam stabilization. The counter-ions strongly affect the level of surfactant adsorption as well. The latter appears to be decisive for the stabilization of the foam and the foam films. We show as well some new effects originating from the counter-ions, which have practical significance.

Sodium dodecyl sulfate (SDS) with molecular weight $M_w = 288.38$ Da, an anionic surfactant, lithium chloride (LiCl) with molecular weight $M_w = 42.29$ Da, sodium chloride (NaCl) with molecular weight $M_w = 58.44$ Da, and potassium chloride (KCl) with molecular weight $M_w = 74.55$ Da were purchased from Sigma Aldrich. The surfactant was purified by threefold recrystallization in ethanol.

SDS salt mixture solutions were prepared as follows. Initially, using SDS, 0.5 mM aqueous solution was prepared. Then, LiCl, NaCl and KCl, were added, thus forming salt solutions with concentrations in the range of 2.5 mM, to 50 mM. As far as the foaming ability of every surfactant solution is expressed in both the initial foam volume upon the very generation of foam and the lifetime of the latter, we chose to work with the ratio between the two values, called foam production[50]. The foam was produced by means of the Bartsch method expressed in energetical tenfold shaking of Bartsch column containing 50 ml of the surfactant solution. Each experiment was repeated at least 3 times for statistical certainty, the averaged initial foam volume and lifetimes were determined. Thus, the foam production for every particular case was calculated. The basic results are presented in **Figure 16**.

One can see that the foam production increases linearly upon the increase of the specific energy of counter-ions adsorption in the range of 2.5 mM to 11 mM added salt (see **Figure 16A**). Moreover, this linear dependence is violated by K^+ counter-ion at concentrations of added salt above 11 mM (see **Figure 16B**, **16C**, **16D**). The foam production decreases significantly abruptly at 25 mM KCl. This low value of the foam production remains at a larger concentration of KCl. They correspond to both low initial foam volume and fast foam decay.

This abnormal effect of KCl on the foam production is worthy of further investigation. Possible way for such an investigation to explore the properties of single foam films with the same contents as these ones was shown in **Figure 16**. Moreover, it is curious to know if the critical concentration at which the K^+ ion acts as defoamer depends on the method of foam generation.

The experimental data presented in **Figure 16A** are in line with the experimental data reported in Ref.[29]. The stability of the dispersed system increases upon the increase of the absolute value of the specific adsorption energy of the counter-ions on the air/water interface. Most possibly, this is due to the increased level of the surfactant adsorption when more counter-ions are integrated in the surfactant adsorption layer. However, to investigate this effect on deeper level further investigations are needed.
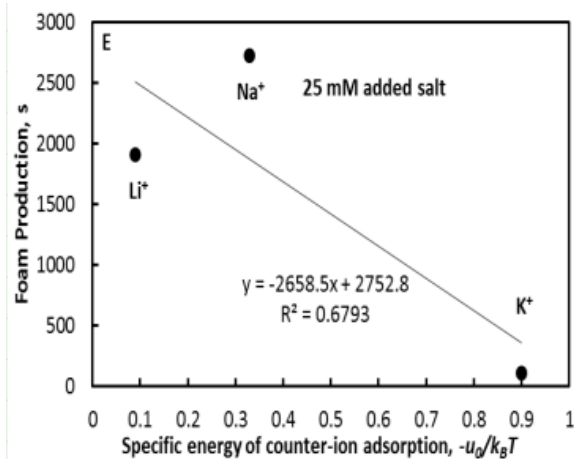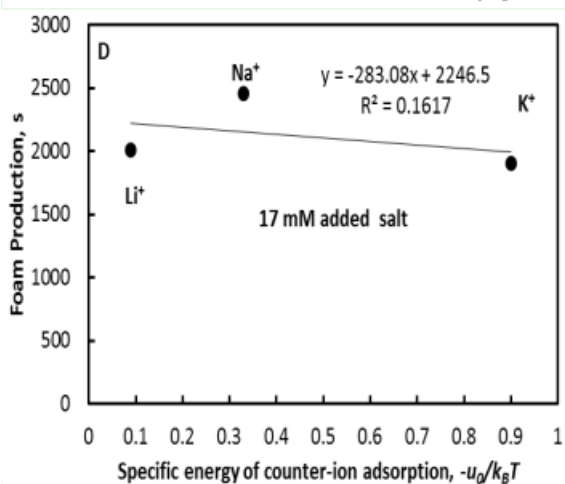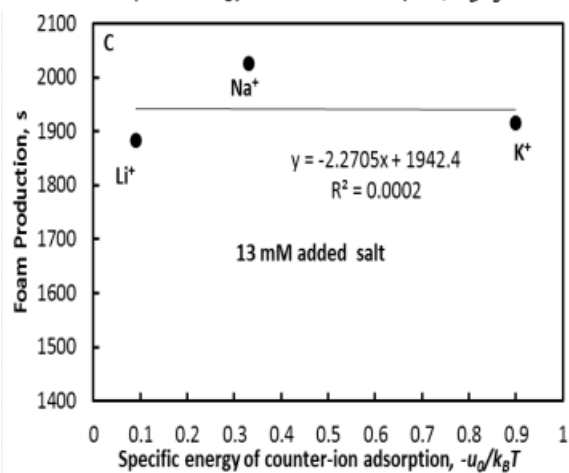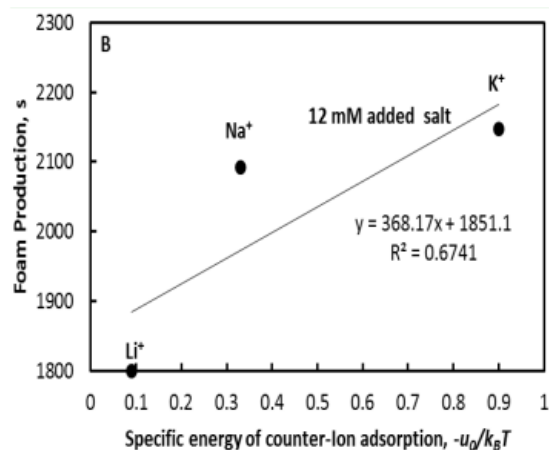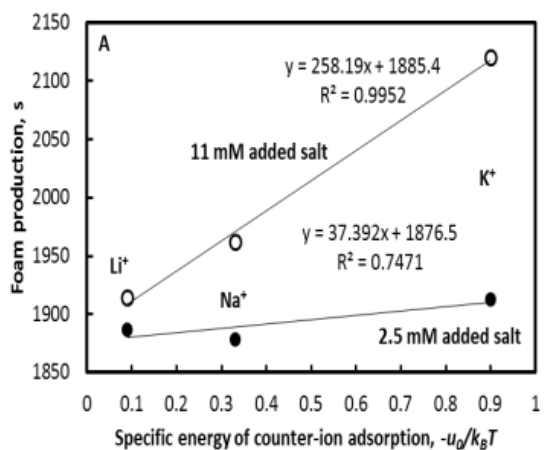
Figure 16. Foam production versus specific energy of counter-ion adsorption at concentrations of added salt in the range of 2.5 mM – 25 mM.

4. Conclusions

The ion-specific effects on the adsorption of ionic surfactants are known effect. There is a large body of literature on this topic, but it is spread out in many papers and books at present. It is known as well that the counter-ions affect the state of the adsorbed layers, which influences the stability of the colloidal dispersions, but the effect is not studied completely. This manuscript gathers together a detailed description of the theory on the ion-specific effects on the adsorption of ionic surfactants in its first approximation (Davies adsorption isotherm) and some initial experimental studies of the Hofmeister effect on the stability of foams and emulsions. Thus, we show the nature of the effect of the counter-ions on the state of the equilibrated surfactant adsorption layer, while we stress that their effect on the stability of colloidal dispersions can be non-equilibrated, thus giving an origin of new tendencies. It was shown that the counter-ions can have a dual effect on the stability of foams and emulsions, depending on the concentration of the added salt. We call for further investigations on this interesting effect, which might be used for controlling the stability of foams and emulsions for industrial needs.

Conflict of interest

No conflict of interest was reported by the author.

65

Acknowledgements

References

1   Lewith S. The behaviour of the proteins in the blood serum in the presence of salts. Archiv Fuer Experimentelle Pathologie und Pharmakologie 1887; XXIX: 1–16.

2   Hofmeister F. About regularities in the protein precipitating effects of salts and the relation of these effects with the physiological behaviour of salts. Archiv Fuer Experimentelle Pathologie und Pharmakologie 1887; XXIV: 247–60.

3   Hofmeister F. About the water withdrawing effect of the salts. Archiv Fuer Experimentelle Pathologie und Pharmakologie 1888; XXV: 1–30.

4   Limbeck Rv. About the diuretic effect of salts. Archiv Fuer Experimentelle Pathologie und Pharmakologie 1888; XXV: 69–86.

5   Hofmeister F. Investigations about the swelling process. Archiv Fuer Experimentelle Pathologie und Pharmakologie 1890; XVII: 395–413.

6   Hofmeister F. The contribution of dissolved components to swelling processes. Archiv Fuer Experimentelle Pathologie und Pharmakologie 1991; XXVIII: 210–38.

7   Muenzer E. The general effect of salts. Archiv Fuer experimentelle Pathologie und Pharmakologie 1898; XLI: 74–96.

8   Kunz W. Specific ion effects in colloidal and biological systems. Current Opinion in Colloid & Interface Science 2010; 15: 34–9.

9   Kunz W, Lo Nostro P, Ninham BW. The present state of affairs with Hofmeister effects. Current Opinion in Colloid & Interface Science 2004; 9: 1–18.

10 Ninham BW, Yaminsky V. Ion binding and ion specificity: The Hofmeister effect and Onsager and Lifshitz theories. Langmuir 1997; 13: 2097–108.

11 Bostrom M, Williams DRM, Ninham BW. Specific ion effects: Why DLVO theory fails for biology and colloid systems. Physical Review Letters 2001; 87.

12 Bostroem M, Williams DRM, Ninham BW. Surface tension of electrolytes: Specific ion effects explained by dispersion forces. Langmuir 2001; 17: 4475–8.

13 Bostrom M, Kunz W, Ninham BW. Hofmeister effects in surface tension of aqueous electrolyte solution. Langmuir 2005; 21: 2619–23.

14 Moreira LA, Bostrom M, Ninham BW, *et al*. Hofmeister effects: Why protein charge, pH titration and protein precipitation depend on the choice of background salt solution. Colloids and Surfaces A: Physicochemical and Engineering Aspects 2006; 282: 457–63.

15 Bostroem M, Ninham BW. Contributions from dispersion and born self-free energies to the solvation energies of salt solutions. The Journal of Physical Chemistry B 2004; 108: 12593–5.

16 Tavares FW, Bratko D, Blanch HW, *et al.* Ion-specific effects in the colloid-colloid or protein-protein potential of mean force: Role of salt-macroion van der Waals interactions. The Journal of Physical Chemistry B 2004; 108: 9228–35.

17 Warszynski P, Lunkenheimer K, Czichocki G. Effect of counterions on the adsorption of ionic surfactants at fluid-fluid interfaces. Langmuir 2002; 18: 2506–14.

18 Para G, Jarek E, Warszynski P. The Hofmeister series effect in adsorption of cationic surfactants - theoretical description and experimental results. Advances in Colloid and Interface Science 2006; 122: 39–55.

19 Para G, Jarek E, Warszynski P. The surface tension of aqueous solutions of cetyltrimethylammonium cationic surfactants in presence of bromide and chloride counterions. Colloids and Surfaces A: Physicochemical and Engineering Aspects 2005; 261: 65–73.

20 Li HH, Imai Y, Yamanaka M, *et al*. Specific counter-ion effect on the adsorbed film of cationic surfactant mixtures at the air/water interface. Journal of Colloid and Interface Science 2011; 359: 189–93.

21 Shimamoto K, Onohara A, Takumi H, W *et al*. Miscibility and distribution of counter-ions of imidazolium ionic liquid mixtures at the air/water surface. Langmuir 2009; 25: 9954–9.

22 Hayami Y, Ichikawa H, Someya A, *et al.* Thermodynamic study on the adsorption and micelle formation of long chain alkyltrimethylammonium chlorides. Colloid and Polymer Science 1998; 276: 595–600.

23 Davies JT. Adsorption of long-chain ions I. Proceedings of the Royal Society of London. Series A 1958; 245: 417–28.

24 Davies JT, Rideal EK. Interfacial Phenomena, 2nd ed. New York: Academic Press; 1963.

25 Borwankar RP, Wasan DT. Equilibrium and dynamics of adsorption of surfactants at fluid-fluid interfaces. Chemical Engineering Science 1988; 43: 1323–37.

26 Ivanov IB, Marinova KG, Danov KD, *et al*. Role of the counter-ions on the adsorption of ionic surfactants. Advances in Colloid and Interface Science 2007; 134-135: 105–24.

27 Ivanov IB, Ananthapadmanabhan KP, Lips A. Adsorption and structure of the adsorbed layer of ionic surfactants. Advances in Colloid and Interface Science 2006; 123-126: 189–212.

28 Slavchov RI, Karakashev SI, Ivanov IB. Ionic surfactants and ion-specific effects: Adsorption, micellization, thin liquid films. In: Romsted LS (editor). Surfactant science and technology: Retrospects and prospects. New York: Taylor & Francis Group; 2014. p. 593.

29 Ivanov IB, Slavchov RI, Basheva ES, *et al.* Hof-

meister effect on micellization, thin films and emulsion stability. Advances in Colloid and Interface Science 2011; 168: 93–104.

30 Robinson RA, Stokes RH. Electrolyte Solutions. 2nd ed. London: Butterworths Scientific Publications; 1959. p. 560.

31 Lucassen-Reynders EH. Surface equation of state for ionized surfactants. The Journal of Physical Chemistry 1966; 70: 1777–85.

32 Davies JT. Study of foam stabilizers using a new (\"viscous-traction\") surface viscometer. Proceedings of the Second International Congress of Surface Activity 1957: 220–4.

33 Lu JR, Marrocco A, Su T, *et al*. Adsorption of dodecyl sulfate surfactants with monovalent metal counter-ions at the air-water interface studied by neutron reflection and surface tension. Journal of Colloid and Interface Science 1993; 158: 303–16.

34 Israelachvili JN. Intermolecular and surface forces. New York: Academic Press; 1985.

35 Jones G, Ray WA. The surface tension of solutions of electrolytes as a function of the concentration. III. Sodium chloride. Journal of the American Chemical Society 1941; 63: 3262–3.

36 Collins KD. Charge density-dependent strength of hydration and biological structure. Biophysical Journal 1997; 72: 65–76.

37 Marcus Y. Effect of ions on the structure of water: Structure making and breaking. Chemical Reviews 2009; 109: 1346–70.

38 Marcus Y. Ion properties. New York: Marcel Dekker; 1997.

39 Marcus Y. Thermodynamics of ion hydration and its interpretation in terms of a common model. Pure and Applied Chemistry 1987; 59: 1093–101.

40 Kunz W, Belloni L, Bernard O, *et al.* Osmotic coefficients and surface tensions of aqueous electrolyte solutions: Role of dispersion forces. The Journal of Physical Chemistry B 2004; 108: 2398–404.

41 Nikolskij BP. Handbook of the Chemist (In Russian). Moscow: Khimia; 1966.

42 Dietrich B, Kintzinger JP, Lehn JM, *et al*. Stability, molecular-dynamics in solution, and X-Ray structure of the ammonium cryptate $[NH_4^+ \subset 2.2.2]PF_6^-$. Journal of Physical Chemistry 1987; 91: 6600–6.

43 Lide DR. CRC Handbook of chemistry and physics. 83rd ed. New York, London: CRC Press; 2002. p. 2664.

44 Sett S, Karakashev SI, Smoukov SK, *et al.* Ion-specific effects in foams. Advances in Colloid and Interface Science 2015; 225: 98–113.

45 Churaev NV, Derjagiun BV, Muller VM. Surface Forces. New York: Springer; 1987. p. 440.

46 Ivanov IB, Hadjiiski A, Denkov ND, *et al.* Energy of adhesion of human T cells to adsorption layers of monoclonal antibodies measured by a film trapping technique. Biophysical Journal 1998; 75: 545–56.

47 Hadjiiski A, Dimova R, Denkov ND, *et al.* Film trapping technique - Precise method for three-phase contact angle determination of solid and fluid particles of micrometer size. Langmuir 1996; 12: 6665–75.

48 Hadjiiski A, Tcholakova S, Ivanov IB, *et al.* Gentle film trapping technique with application to drop entry measurements. Langmuir 2002; 18: 127–38.

49 Tcholakova S, Denkov ND, Ivanov IB, *et al.* Coalescence in beta-lactoglobulin-stabilized emulsions: Effects of protein adsorption and drop size. Langmuir 2002; 18: 8960–71.

50 Karakashev SI, Georgiev P, Balashev K. Foam production — ratio between foaminess and rate of foam decay. Journal of Colloid and Interface Science 2012; 379: 144–7.

Case Report

A port-stream based equation oriented modelling of complex distillation column: A dividing wall column case study

R. Idris, N. Harun, MR. Othman[*]

Process Systems Engineering Research Group, FKKSA, Universiti Malaysia Pahang, Gambang 26300, Pahang, Malaysia. E-mail: rizza@ump.edu.my

ABSTRACT

Dividing wall column (DWC) offers higher degree of freedom in comparison with the conventional column. Furthermore, the different sections configurations within the column are highly interacting with several recycle loops. Facing with such complex unit operation, describing its behaviour encourages the focal point on the resolution of ideal modelling approaches. Equation oriented (EO) modelling of DWC has been studied by several researchers involving complex algorithm and methodology. In this work, a new approach for modelling of DWC is presented. The modelling methodology involves variables connectivity based on ports and streams that is admissible to equation-oriented flow sheet. To verify the functionality of the proposed method, the modelled DWC is validated with two case studies depicted from experimental literature data to separate alcohol mixture and fatty acid fractionation. The model development was performed in MOSAIC, a web-based modelling tool and run in gPROMS. The model shows good convergence and has less than 10% error when compared to the above mentioned case studies. To furthermore extend the model capability, relative gain array (RGA) analysis was conducted for the fatty acid fractionation to determine the best control configuration in DWC. Result shows that L-S-V and L-S-B configurations are the best control configurations. Our analysis also shows that reflux flowrate, side flowrate and vapor boilup are best to control distillate product, side product and bottom product, respectively.

Keywords: Dividing Wall Column; Process Modelling; Relative Gain Array

1. Introduction

Dividing wall column (DWC) is an intensified design of Petlyuk column which provides a good alternative to conventional distillation column due to possible saving in both energy and capital cost around 30%[1]. A DWC possesses a vertical partition that splits the column shell into a pre-fractionator and main column section as shown in **Figure 1**. Such configuration compensates the impurity of the side product from being mixed with the distillate and bottom products. For ternary mixtures, applying DWC is able to cut down a column, thus reducing the number of condenser and reboiler with reliable product quality achievement. Regardless of its potential advantages, industrial implementation of dividing wall columns was often restricted due to the design, control and operational concern.

Often modelling of DWC was done through sequential modular (SM) based model compared to equation oriented (EO) based model. In SM modelling, two or three column configurations were often used. Four column configurations, however, are more accurate to represent the four sections of DWC[2].
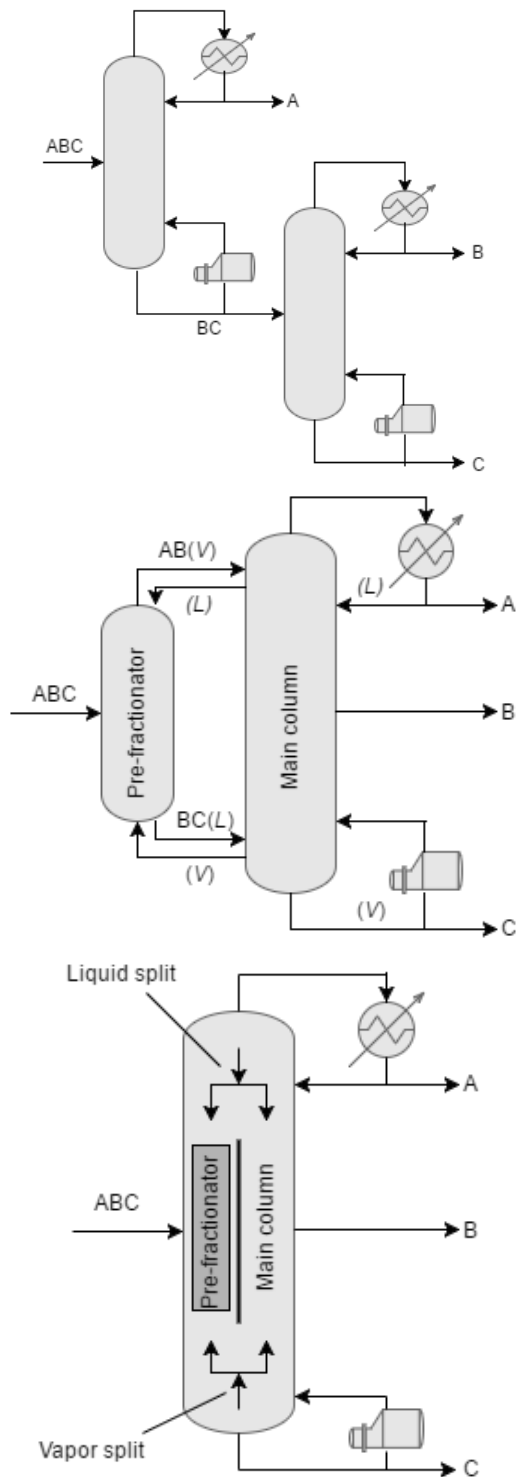
Figure 1. (Left) Conventional distillation column (Middle) Pet-lyuk column and (Right) Dividing wall column (DWC) configuration**.**

However, with the existence of internal recycle streams in DWC, due to the interconnecting stream, on all four column sections caused serious convergence problems. EO, on the other hand, offers good solution over SM, especially when dealing with design and optimization problems, solving heat integrated or recycled processes and model tuning

analysis. EO modelling compensates the convergence problem by accumulating all model equations together and solves them at the same time. Modelling of DWC via first principle EO modelling is not an easy task as it is considered as complex non-standard distillation column. One main reason is due to the interconnectivity of input/output variables, especially on the pre-fractionator section and main column section.

Work on EO modelling of DWC is however limited due to its modelling complexity. Dunnebier and Pantelides had considered the modelling of DWC using so called detailed column superstructures based on the State Operator Network formulation[3]. Due to the complexity of the models and mathematical problems, determination of the optimal structure referring to the suggested approach encountered some obstacles in optimization. Pattison *et al.*[4] also presented a new modelling approach based on the Pseudo-transient method. They reformulated the steady-state MESH (material, equilibrium, summation, and heat) equations of DWC as differential-algebraic equation (DAE) system which has the same steady state solution as the original system. These works applied a complicated EO approach to DWC modelling, which is time-consuming to comprehend. As such, we introduced a much simpler and systematic modelling approach. The proposed method solves the input/output variables connectivity of different equation systems by introducing a port and stream concept. Generally, the approach presents an equation system which functionally similar to a unit operation, i.e., column, reboiler, and condenser, with a presence of ports to identify the standardization of input and output variables. In addition, the existence of streams in connects another individual equation system together. To aid the model development, a MOSAIC modelling software will be used as modelling tools and gPROMS to solve the equation systems.

2. Modelling methodology

This section describes details of the proposed method. For better understanding, this section starts with definition of equations systems and variables involved in modelling of DWC.

2.1 Equation system and variables of DWC

Equation system is combination of fundamental principle of the underlying process or unit operation under considerations by reformulating the MESH (material, equilibrium, summation, and heat) equations. The DWC models in this work were based on the conventional equilibrium-based models of the distillation column. In this work we are focusing on the product composition and composition along the DWC. Energy balance will be our future work. The following assumptions had been taken into account for the model development:

1) Steady-state equilibrium stage model.
2) Average phase equilibrium constant.
3) Material balance.
4) Constant vapour split ratio as it is fixed by column design.

For the rectifying section, pre-fractionator section, main section, and stripping section the component material balance for component i at stage j is given as:

$$0 = V_{j+1}y_{j+1} + L_{j-1}x_{j-1,i} - V_jy_{j,i} - L_jx_{j,i} + F_jz_{j,i} - S_jx_{j,i} \tag{1}$$

Where, S represents a side stream flow rate. Summation equations is given in equation (2) whereas equilibrium relationship is given in equation (3).

$$\sum_{i=1}^{N} x_{j,i} = 1 \quad \sum_{i=1}^{N} y_{j,i} = 1 \tag{2}$$

$$y_{j,i} = K_{j,i}x_{j,i} \tag{3}$$

For the condenser, the material balance is:

$$0 = V^{(upper)} \cdot y_i^{(upper)} - L_0 \cdot x_{D,i} - D \cdot x_{D,i} \tag{4}$$

Whereas, the summation equation is given as:

$$\sum_{i=1}^{N} x_{D,i} = 1 \tag{5}$$

For the reboiler,

Material balance:

$$0 = L^{(bottom)} \cdot x_i^{(bottom)} - V^R \cdot y_i^R - W \cdot x_{W,i} \tag{6}$$

Equilibrium relationship:

$$y^R = K^R \cdot x_{W,i} \tag{7}$$

Summation equation is:

$$\sum_{i=1}^{N} x_{j,i} = 1 \quad \sum_{i=1}^{N} y_{j,i} = 1 \tag{8}$$

At the intersection of rectifying section with pre-fractionator and main column, the vapor mixing is represented by,

$$V_{j=NS+1}y_{j=NS+1,i} = V^{left}y_i^{left} + V^{right}y_i^{right} \tag{9}$$

$$V_{j=1}y_{j=1,i} = V^{left}y_i^{left} \tag{10}$$

$$V_{j=1}y_{j=1,i} = V^{right}y_i^{right} \tag{11}$$

Whereas, liquid splitting is represented by,

$$\alpha L_{j=NS} = L^{left} \tag{12}$$

$$x_{j=NS,i} = x_i^{left} \tag{13}$$

$$(1 - \alpha)L_{j=NS} = L^{right} \tag{14}$$

$$x_{j=NS,i} = x_i^{right} \tag{15}$$

$$L_{j=0}x_{j=0,i} = L^{upper}x_i^{upper} \tag{16}$$

On the other hand, at the intersection of pre-fractionator and main with stripping sections vapor splitting is represented by,

$$V_{j=NS+1}y_{j=NS+1,i} = V^{bottom}y_i^{bottom} \tag{17}$$

$$\beta V_{j=1} = V^{left} \tag{18}$$

$$y_{j=1,i} = y_i^{left} \tag{19}$$

$$(1 - \beta)V_{j=1} = V^{right} \tag{20}$$

$$y_{j=1,i} = y_i^{right} \tag{21}$$

And liquid mixing is represented by,

$$L_{j=0}x_{j=0,i} = L^{left} \cdot x_i^{left} + L^{right} \cdot x_i^{right} \tag{22}$$

$$L_{j=NS}x_{j=NS,i} = L^{left}x_i^{left} \tag{23}$$

$$L_{j=NS}x_{j=NS,i} = L^{right}x_i^{right} \tag{24}$$

The connection between rectifying and condenser unit are given by,

$$V_{j=1}y_{j=1,i} = V^{out}y_i^{out} \tag{25}$$

$$L_{j=0}x_{j=0,i} = L^{in}x_i^{in} \tag{26}$$

Meanwhile, stripping and reboiler connectivity is given by,

$$L_{j=NS}x_{j=NS,i} = L^{out}x_i^{out} \tag{27}$$

$$V_{j=NS+1}y_{j=NS+1,i} = V^{in}y_i^{in} \tag{28}$$

The subscripts *NS* and *NS+1* indicate that liquid and vapour flow on the last stage of each section will be connected to other section. The superscripts in and out are known to be the inlet and outlet flow which happen between stripping/reboiler and rectifying/condenser, while superscript of upper, left, right, and bottom are referring to rectifying, pre-fractionator, main, and stripping section respectively. Next, α indicates a liquid splitting factor and β is for vapour split factor.

2.2 Unit block and ports

The challenge in modelling of DWC is to accommodate the internal flows between the partition walls. In this work, we treated rectifying section, pre-fractionator, main, and stripping section as individual unit block along with the condenser and reboiler. A unit block model consists of sets of mathematical equation systems to describe the

phenomenon occurring inside the unit. This creates a convenient way to model the DWC as a group of 6 sub-unit bocks with underlying equation systems. **Table 1** indicates the underlying classification of equation system involved in the respective unit block.

Table 1. Unit block and its associated equation systems

Unit block	Equation systems involved
Rectifying	1, 2, 3, 9, 12, 13, 14, 15, 25, 26
Pre-fractionator	1, 2, 3, 10, 16, 17, 23
Main	1, 2, 3, 16, 17, 24
Stripping	1, 2, 3, 18, 19, 20, 21, 22, 27, 28
Condenser	4, 5
Reboiler	6, 7, 8

In order to properly connect different unit blocks together, the application of port is introduced into the unit block. Port is used to provide reconciliation of different input and output variables of a unit block to or from another unit block. To further describe the concept, an example to rectifying unit is considered (referring to **Figure 2**). Rectifying unit is located at the top section of the DWC internal configuration. Vapour from the pre-fractionator section and main section will be mixed at the last stage of the rectifying unit, whereas, liquid flow at the last stage will be split into both side of pre-fractionator section and main section. To describe this phenomenon, equation (9) represents the vapour mixing occurred at the last stages of the rectifying section. Port 1 (P1) signifies the vapour flow from the first stage of the pre-fractionator section (Equation (10)), whereas, P5 signifies the vapour flow from the first stage of the main section (Equation (11)). Thus, the input variables involved for the vapour mixing are $V^{left}, V^{right}, y_i^{left}$ and y_i^{right}. Equation (12) to equation (15) on the other other hand signify the splitting of liquid flow flowing down from the last stage of rectifying section into pre-fractionator section and main section. P2 denotes the liquid split to the pre-fractionator represented by equation (12) and equation (13), whereas, P4 denotes the liquid split to the main section represented by equation (14) and equation (15). Therefore, the output variables for the liquid split are $L^{left}, x_i^{left}, L^{right}$, and x_i^{right}. In addition, P6 denotes the liquid flow from condenser to the first stage of the rectifying unit which describes by equation (26). P3, on the other hand, denotes the

vapour flow from the first stage as described by equation (25). Therefore, V^{out} and y_i^{out} are the output variables of the vapour flow, whereas, L^{in}, and x_i^{in} are the input variables of the condenser.
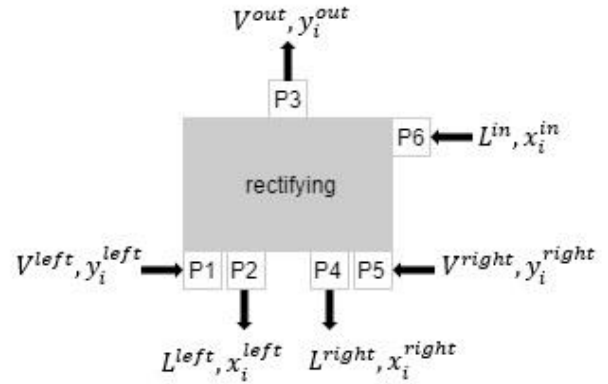
Figure 2. Rectifying Unit Block Model with Ports**.**

For the port to be reconciled, it needs to have an interface variable. An interface consists lists of identified independent variables to restrict the accessibility of the other unrelated variables in the overall equation system. In this example, f and c_i were used as interface variable to represent vapour/liquid flowrate and composition of component i, respectively. Overall, f will represent variables $V^{out}, L^{in}, V^{left}, L^{left}, V^{right}$ and L^{right}, whereas, c_i will represent variables $y_i^{out}, x_i^{in}, y_i^{left}$, x_i^{left}, y_i^{right}, and x_i^{right}. The port and interface application are visualized in **Figure 3.**
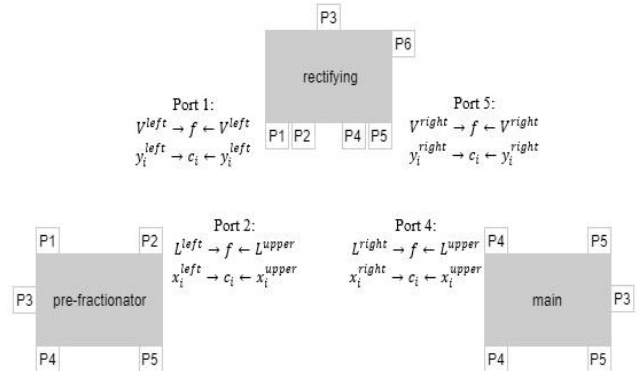
Figure 3. Port and interface application in DWC sub-units block**.**

2.3 Unit block connectivity using stream

When all the unit blocks and its associated ports have been created, they are then ready to be connected to each other using streams. The purpose of stream is to connect two different units block that provides ports to work jointly in a flowsheet. The

implementation of a stream requires list of identified variables in the interface along with ports in order to be combined together. The flow direction of the stream, either "output" port or "input" port indicator needs to be specified for smooth connectivity. The output port represents the start of the stream while input port indicates the end of the streams, depending on how the flow direction works. **Figure 4** exhibits the complete model of DWC with ports and streams application. The dotted and solid lines indicate the flow of liquid and vapor respectively inside DWC.
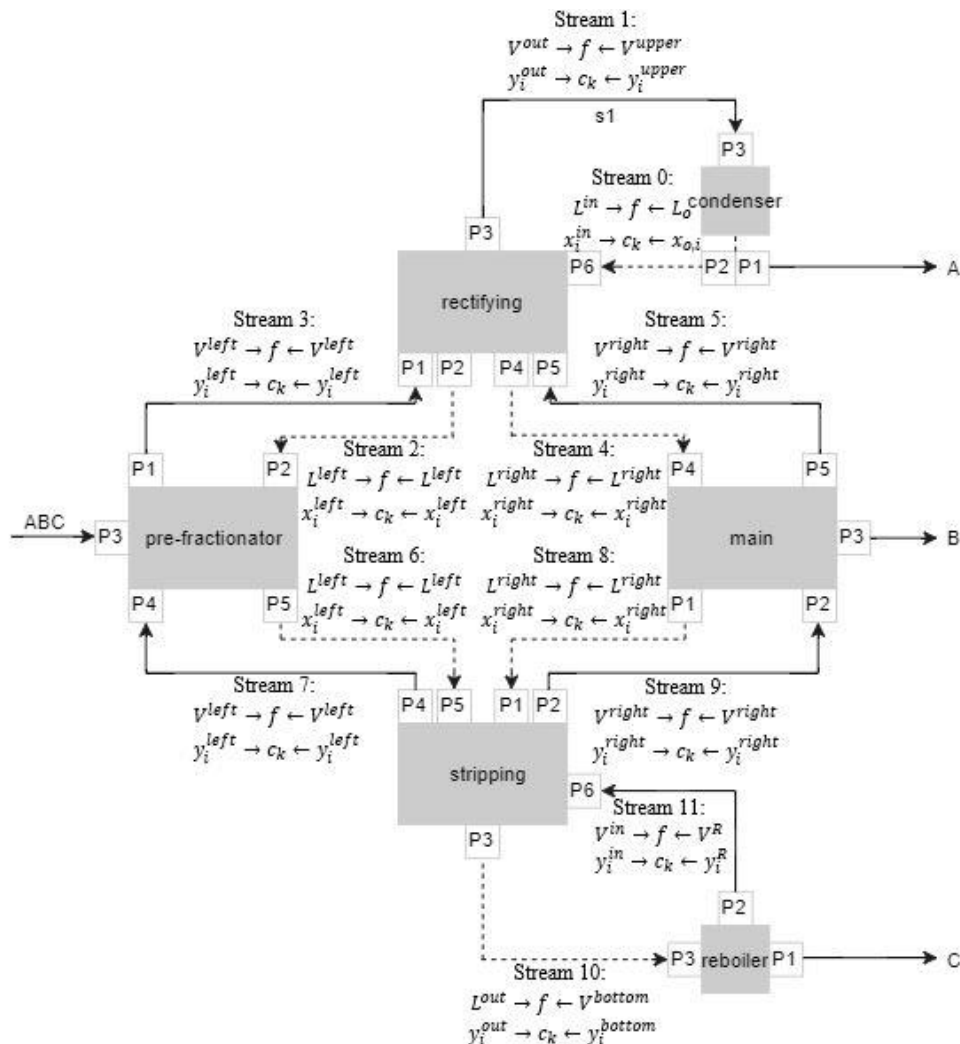
Figure 4. Model of DWC with port-stream application.

3. Model development

The DWC development based on the proposed methodology was performed in MOSAIC. MOSAIC is a web-based equation oriented modelling environment for modelling of chemical processes, which developed by the Process Dynamics and Operations Group at Technische Universitaet Berlin. One of the MOSAIC features is modelling at the documentation level[5]. The model equations in MOSAIC are entered using LaTeX style and saved in MathML which provide higher readable model to the user. MOSAIC additionally works as a code generator which is able to export the developed model into certain programming language code.

3.1 Variable Specification and Classification

One of the important features of EO modelling is the variables' specification required as input data and generated as output predictions. Each variable in the equations will be specified by fixing the value or enabling the modeling tool to manipulate the value[6]. Those variables are classified as design and iteration values. Design variables indicate the fixed value variables, whereas, iteration variables mean calculated variables in the equation systems.

Those variables can be changed either from iteration variables to design variables or vice versa until the DOF becomes zero. For the case of the DWC model, the vapor composition, constant phase equilibrium, liquid and vapor flow in respective unit are assigned as design variables. Meanwhile, the liquid composition and products stream composition are set to be iteration variables. Another important issue to be considered is the initial value for the iteration variables. It should be noted that, in modeling solving, good initial values are crucial since the developed model would work well when all variables near the solution[7]. One may be used SM software, i.e., Aspen Plus is used to aid initilization values estimation for a good convergence.

3.2 DWC model structural analysis

To guarantee that the equation systems of DWC model are well formulated, the degree of freedom (DOF) analysis is carried out to determine if the equation systems are well, under, or over determined. **Figure 5** shows the structural analysis of mixed DOF of the DWC model. The consequences of inaccurate chosen of design variables in the DWC system lead to the insufficient structure analysis (referring to **Figure 5**), and unsolved problems in the compiler or solver.
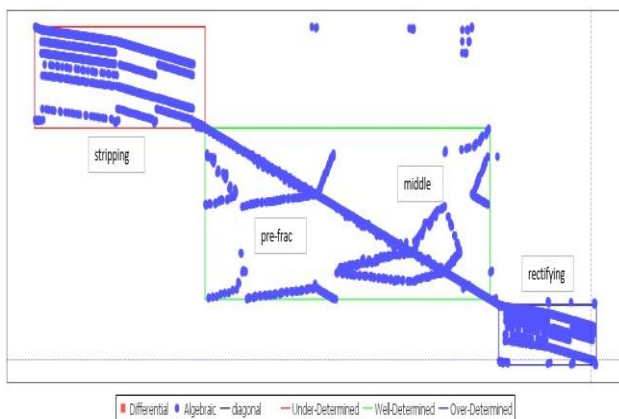
Figure 5. Unstable structure analysis of DWC system**.**

The insufficient structure analysis generates three different colours of rectangle/line which are green, blue, and red. The under-determined equation system represented in blue rectangle line is due to more equations being provided than calculated variables, while the red rectangle line exhibits under-determined equation system caused by less equation being provided than variables to be calcu-

lated. From the figure, the equation systems for pre-frac and middle are well determined. Stripping section and reftifying equation systems on the other hand are under-determined and over-determined, respectively.

From the **Figure 5**, it visualized that the structure of the equation systems is affected by the chosen degree of freedom[8]. In other words, to achieve a well-posed problem, the needs in change of design variable and calculated variable specifications are compulsory to preserve DOF. To ensure that all equation systems are well determined, selection of design and iteration variables is important to solve the given problem, to identify the product stream compositions. Based on the whole structure analysis of DWC, further observation shows that some of the design variables on rectifying equation system are set as iteration variables and likewise some of the iteration variables on stripping equation system are set as design variables. Therefore, to fix this problem, the classification of design and iteration variables should be restructured.

After proper assignments of design and iteration variables, **Figure 6** shows that the overall six sub-equation systems of DWC model are "well determined", which means the model is solveable. Other than that, the structure analysis also gives the information on the type of equations. In this case, the structure analysis indicates that the whole equations system of DWC involved with algebraic equations with non-existing of ordinary differential equations (ODEs) as well as non-existing differential algebraic equations (DAEs).
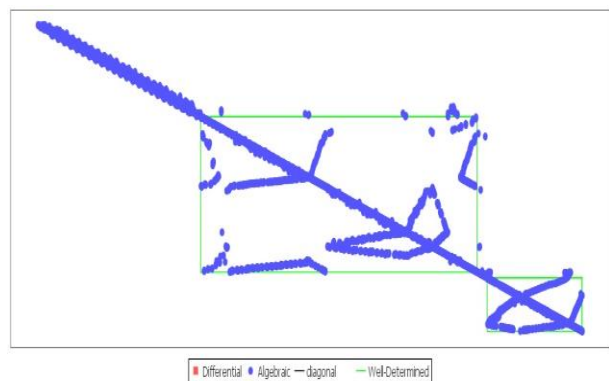
Figure 6. Well determined structure analysis of DWC system**.**

4. Model validation

The completed DWC model simulation in

MOSAIC was exported to gPROMS ModelBuilder to solve the compositions in the column. To demonstrate the capability of the modelling approach and to increase the acceptance of the model, the modelled DWC is validated with two case studies. Case Study 1 refers to open literature experimental data depicted from Nguyen *et al.*[9], whereas, Case Study 2 refers to fatty acid fractionation from Illner and Othman[2]. For Case 1, the model will be compared with the second data set of the experimental work. Furthermore, in Case 2, the model will be compared to a simulated case study for fractionating fatty acid in DWC.

4.1 Case study 1: Separation of ternary mixture: Methanol/ 1-Propanol/ 1-Butanol

The verification data were based on the experimental work by Nguyen *et al.*[9] Their work involved separation of ternary mixtures of alcohol namely methanol, 1-propanol, and 1-butanol using DWC pilot plant.

Table 2. Operating parameter of alcohol ternary mixture for data set 2

Parameter	Specification
Feed flowrate (kg/h)	5.77
Feed temperature (°C)	85.4
Feed composition (wt%)	
Methanol	0.29
1-propanol	0.46
1-butanol	0.25
Liquid split	0.5
Vapor split	0.5
Reboiler duty (kW/h)	5.1
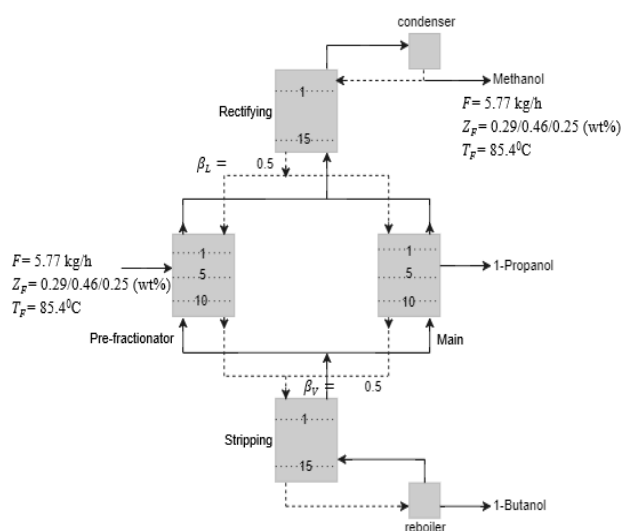
Figure 7. Schematic DWC configuration for the alcohol fractionation.

According to the volatilities of the components,

methanol is withdrawn as a distillate product, while 1-propanol and 1-butanol are collected as side stream and bottom product, respectively. The column structure consists of 15 stages on the rectifying and the stripping section, and 10 stages on the pre-fractionator and main section. The schematic configuration is shown in **Figure 7.** The liquid split was set up to be 0.5 and so does with vapor split as cross sectional areas of pre-fractionator and main column are the same. **Table 2** indicates the operating parameter used in the experimental work.

4.1.1 Initialization value

Good initial values are crucial since the developed model would work well when all variables near the solution[7]. Therefore, to aid the initialization value estimation, Aspen Plus was used in this work. **Figure 8** shows a DWC configuration in Aspen plus flowsheet. A DWC model does not exist in Aspen Plus library due to its customized model. Therefore, an equivalent model of DWC with four rigorous RADFRAC model, two units of mixer and splitter for liquid and vapor internal mixing and splitting purpose were implemented. The results of simulation generated in Aspen Plus were used to provide the initial value of all the unknown variables in the DWC equation systems to gain a good convergence of output value prediction. Once the initialization value was given, the model is ready to be translated into gPROMS code.
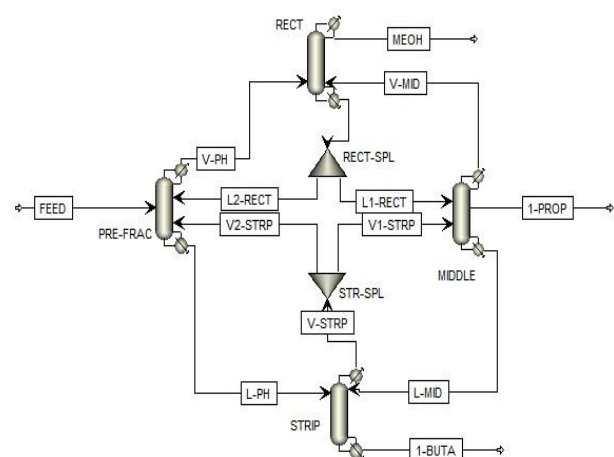
Figure 8. Column configuration of DWC for alcohol mixture.

4.1.2 Model solver

The complete process model of DWC involved large sets of nonlinear algebraic equation (NLE)

and was numerically solved using differential-algebraic solver (DASolver) in gPROMS solution algorithm. This includes Block Decomposition Non-Linear Solver (BDNSOL) and SPARSE solver, which is able to solve the restricted iteration variables that lie within specified lower and upper bound. BDNSOL solver resolves the non-linear equation, according to an individual unit block of rectifying, pre-fractionator, main, stripping, condenser, and reboiler. The variables in each unit blocks were solved using SPARSE through Newton-type iterative method, which resulted on a prediction of component variable in each stage.

4.1.3 Value comparison

The relative error between EO simulation results and literature data was calculated as follows:

$$\text{Relative error (\%)} = \frac{\text{initial} - \text{final}}{\text{initial}} \times 100 \qquad (29)$$

In this study, the relative error which is less than 10% is considered reasonable due to small value of the experimental data from Nguyen *et al*.[9] Moreover, the process characteristic of DWC, such as pressure, energy, and heat transfer were not considered in the modeling work. The verification results are shown in **Table 3**.

Table 3. Relative error between literature data and EO simulation results for data set 2

Parameters	Unit	Literature data	EO simulation	Relative error (%)
Distillate flowrate	(kg/h)	2.00	2.00	0
Methanol composition	(wt%)	0.85	0.93	9.41
Side stream flowrate	(kg/h)	2.17	2.17	0
1-propanol composition	(wt%)	1.00	1.00	0
Bottom stream flowrate	(kg/h)	1.70	1.69	0.58
1-butanol composition	(wt%)	0.89	0.90	1.12

For distillate product stream, the result acquired from EO simulation for Methanol composition was 0.93 wt% which differs about +0.08 wt% from reference literature data and led to 9.41% relative error. The side product stream, 1-propanol demonstrates an equivalent of convergence value with literature data in regards to product flowrate and composition. For bottom stream flowrate, a different about +0.1 kg/h in comparison to literature

experimental data was recorded which resulted in 0.58% relative error. Whereas, the composition of 1-butanol generated from EO simulation appeared to have a slightly different about +0.01 wt% and makes the relative error of 1.12%. Therefore, from the table, the proposed model shows a good convergence in term of products flowrate and compositions and has less than 10% relative error which shows applicability of the proposed approach.

4.2 Case study 2: Fatty acid fractionation

The validated DWC model was then tested to a fatty acid (FA) fractionation. By far, in the oleo-chemical industry particularly for FA, the mixture had only been studied by[2] since most of the industry still using a conventional distillation columns to separate FA mixture[1,10,11]. The configuration of the dividing wall column for fatty acid fractionation was designed similarly using four columns sequence proposed by the authors. Fatty acid fractionation was separated into three cuts light-cut (LC), middle-cut (MC), and heavy cut (HC) according to their boiling points. The boiling point of LC which represented by C_{10} is 269 ℃, while the boiling point of MC (C_{14}) and HC (C_{16}) are 326 ℃ and 350 ℃, respectively. Since C_{10} is the most volatile component, it will be withdrawn as a distillate product. The least volatile component (C_{16}) will be withdrawn at the bottom of the column due to high boiling point, while the side stream goes to component C_{14}. The design parameter input was based on the simulation work done by Illner and Othman[2], but with slide modification that suits the pilot plant design capacity of 5kg/hr.

Figure 9 shows the schematic DWC configuration for fatty acid fractionation. The rectifying section consists of 14 stages, while pre-fractionator section has 21 stages, main section and stripping section have 20 and 24 stages, respectively. The condenser is at stage 0 and reboiler at the last/bottom stage of the column. Feed stream enters at stage 10 from the top in the pre-fractionator section and the side product is withdrawn at stage 3 in the main section. The liquid split ratio is 0.84, and the vapor split ration is 0.5. Thus the wall is located at the middle of the column.

Using the same relative error calculation in

equation (29), **Table 4** compares the product specification value in Aspen Plus and the developed model. Result shows that the highest relative error is 0.88% for bottom stream flow rate. The bottom flowrate from model was -0.01 lower than the initial reference data which is 1.13 kg/h, while for the HC composition, the model shows 0.999 wt% which led to 0% of relative error. For both side stream flowrate and MC product composition, the value indicates zero difference between initial reference data and the model which was 3.451 kg/h and 0.942 wt%, respectively. Same goes to distillate flowrate composition which represented by LC, where the initial input data and final value output prediction was identical. The results conclude the applicability of the developed model.
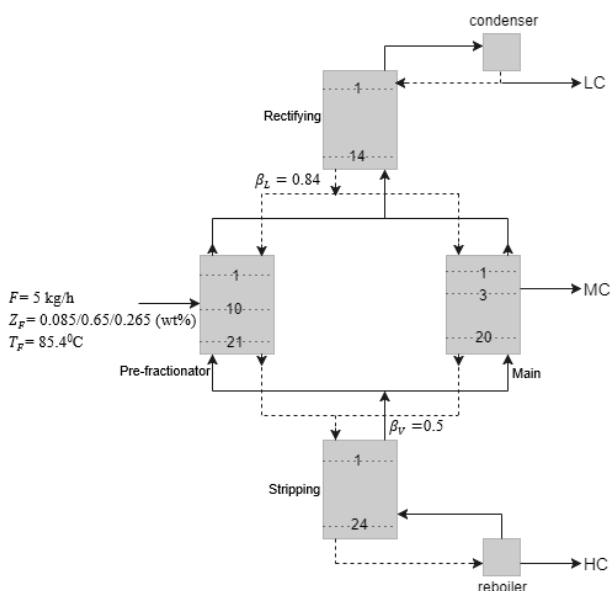
Figure 9. Schematic DWC configuration for fatty acid fractionation.

Table 4. Comparison between specified product value in Aspen Plus and EO simulation

Parameters	Unit	Aspen Plus	EO simulation	Relative error (%)
Distillate flowrate	(kg/h)	0.420	0.420	0
LC composition	(wt%)	0.999	0.999	0
Side stream flowrate	(kg/h)	3.451	3.451	0
MC composition	(wt%)	0.942	0.942	0
Bottom stream flowrate	(kg/h)	1.130	1.120	0.88
HC composition	(wt%)	0.999	0.999	0

4.2.1 FA composition trend in DWC

Figure 10 gives the composition profiles in the rectifying, main, and stripping sections. **Figure 10** (**a**) shows the composition trend for the rectifying section. It can be seen that the highest composition of LC was at stage 1 and remain consistent up to stage 10 with 0.999 to 0.995 wt%. At stage 11 up to stage 13, the composition begins to decrease gradually and became 0.076 wt% at stage 14. Meanwhile, the side component, MC starts to increase slowly from stage 11 at 0.037 wt% to 0.867 wt% at stage 14, while the HC product almost remains at 0.0 wt% at the last stage of rectifying column.

Figure 10 (**b**) shows the trend for LC, MC, and HC product composition in main section. From the graph, as LC component starts to enter the first stage of the main column, the composition indicates 0.0 wt%. On the contrary, MC composition remains constant around at composition of 0.93 wt% at stage 15 until it reached stage 31 and starts to decrease to 0.645 wt% at the last stage of the main column. For HC component, the composition remains constant at stage 15 up to stage 31 with 0.057 wt% and increases slowly at 0.355 wt% when reached the last stage of the main section.

Figure 10 (**c**) shows the composition trend in the stripping column. From the graph, LC component composition remains at 0 wt% along the stripping column, which means zero existence of distillate product on the stripping section, while for MC component, it starts to decrease steadily as it enters the first stage from 0.237 wt% to almost 0.0 wt% until the last stage of stripping section. On the other hand, the composition of HC component begins to increase slowly starting from the stage 35 up to stage 41, and reached the highest composition with 0.999 wt% at the last stage of the stripping section. Therefore, these graphs clearly shows that LC and MC components are separated at the upper stage of the main column, meanwhile, MC and HC components are separated at the bottom stage of the main column.

(a)

(b)

(c)
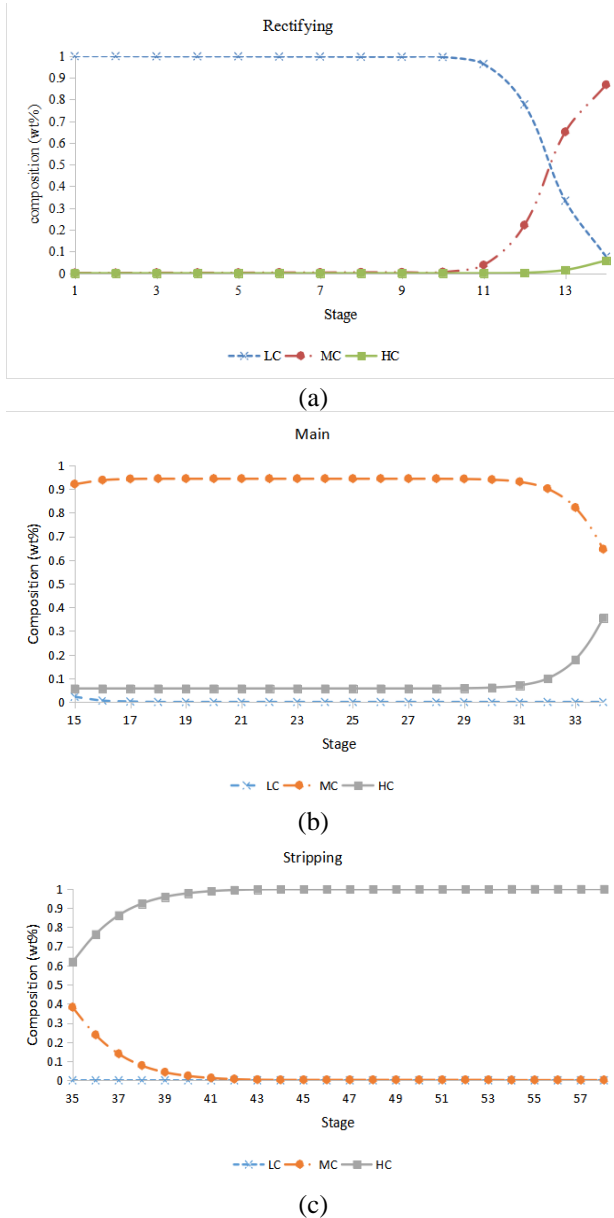
Figure 10. Components trend along **(a)** Rectifying, **(b)** Main, and **(c)** Stripping section**.**

4.2.2 Relative Gain Array (RGA)

To further exploit the developed model, RGA analysis was conducted to the DWC FA fractionation model. Based on the model, RGA analysis could be used to determine suitable control scheme at steady-state. For DWC, a multi-input-multi-output (MIMO) control scheme was used due to the possibility of multiple interaction between manipulated and controlled variables[12].

According to Koko and Barakat[13], there are seven DOF corresponding to seven manipulated variables in DWC. However, the liquid split (β_L) and vapor split (β_V) are not suggested to be a manipulated variables, because they could cause a se-

rious problem in the operation and controllability of DWC[14,15]. Therefore, five available manipulated variables namely reflux flowrate (L_o), distillate flowrate (D), side flowrate (S), bottom flowrate (B), and vapor boilup (V) were used to analyze its interaction to the controlled variables which are distillate, side, and bottom product compositions. For DWC, a combination of three manipulated variables was chosen. Thus, based on the five manipulated variables, there are four possible control scheme configurations namely L-S-V, D-S-V, L-S-B, and D-S-B. To determine the best control scheme configurations, the four control schemes were analyzed.

Table 5 consists of the base case values for the FA fractionation. The open-loop gain was calculated from the step changes on each manipulated variables. The step changes were carried out by changing one manipulated variables at a time while putting the rest of manipulated variables constant at their base case value. For each control schemes configuration, a 10% step change of the base case value on each manipulated variables was applied. The results of the steady-state gain array and its calculated RGA value are presented from **Table 6** up to **Table 9**.

Table 5. FA fractionation base case values

Manipulated variables	Value	Controlled variables	Value
Reflux flowrate, Lo (kg/h)	25.74	LC (wt%)	0.999
Distillate flowrate, D (kg/h)	0.42	MC (wt%)	0.942
Side flowrate, S (kg/h)	3.45	HC (wt%)	0.999
Bottom flowrate, B (kg/h)	1.13		
Vapour boilup, V (kg/h)	35.13		

Table 6. Steady state gain matrix and RGA for L-S-V scheme

CV	Steady state gain			Relative Gain Array (RGA), λ		
	MV$_1$ = L	MV$_2$ = S	MV$_3$ = V			
X$_{LC}$	-0.03559	0	0.00006	0.99999	0	0.00001
X$_{MC}$	-0.00081	-0.01151	-0.00081	0.00001	0.99421	0.00578
X$_{HC}$	0	0.00006	-0.00070	0	0.00579	0.99421

Table 7. Steady state gain matrix and RGA for D-S-V scheme

CV	Steady state gain			Relative Gain Array (RGA), λ		
	MV$_1$ = D	MV$_2$ = S	MV$_3$ = V			
X$_{LC}$	0.04524	-0.00551	-0.00077	1.22945	-0.26012	0.03067
X$_{MC}$	0.02143	-0.01206	0.00032	-0.26089	1.25206	0.00883
X$_{HC}$	-0.00095	-0.00009	-0.00075	0.03143	0.00807	0.96050

77

Table 8. Steady state gain matrix and RGA for L-S-B scheme

CV	Steady state gain			Relative Gain Array (RGA), λ		
	MV_1 = L	MV_2 = S	MV_3 = B			
X_{LC}	-0.03561	0	0	1.00000	0	0
X_{MC}	0.00042	-0.05197	0.00531	0	0.97339	0.02661
X_{HC}	-0.00059	0.00672	0.02513	0	0.02661	0.97339

Table 9. Steady state gain matrix and RGA for D-S-B scheme

CV	Steady state gain			Relative Gain Array (RGA), λ		
	MV_1 = D	MV_2 = S	MV_3 = B			
X_{LC}	0.10476	-0.00029	0	1.11392	-0.11392	0
X_{MC}	0.12976	-0.00490	0.01142	-0.10542	1.43829	-0.33288
X_{HC}	0.00714	0.00075	-0.00779	-0.00851	-0.32437	1.33288

According to the RGA principles, it is strongly recommended to choose the value of relative gains array λ_{ij}, (which are positive and closed to one[13,16]. This shows that the control loop between controlled variable i and manipulated variable j has a strong interaction and did not be effected by the other control loops.

Table 7 and **Table 9** show the RGA value for D-S-V and D-S-B configurations. The values of λ_{11} are 1.22945 and 1.11392, respectively. For the first manipulated variable, it indicates that the manipulation of distillate flow did not only affect the distillate composition (x_{LC}), but also experience an interaction with other controlled variables (x_{MC} and x_{HC}) as well. For the second manipulated variable, which is side flowrate, these configurations show the value of λ_{22} equals to 1.25206 for D-S-V and 1.43829 for D-S-B. This shows that the interaction between side flowrate on side composition (x_{MC}) does have an interference from other controlled variables (x_{LC} and x_{HC}) too. Finally, for the third manipulated variable, the interaction between vapor boilup in D-S-V and bottom flowrate in D-S-B on bottom composition (x_{HC}) give the λ_{33} value of 0.96050 and 1.33288. It means that the interaction of control loop under consideration was provoked by the other control loops (x_{LC} and x_{MC}).

The other two configurations, L-S-V and L-S-B, on the other hand, were selected due to small interaction between the loops. Based on **Table 6** and **Table 8**, for L-S-V and L-S-B configurations, the value of λ_{11} equals to 0.9999 and 1.0000, which show that distillate composition (x_{LC}) only responds to the manipulation of distillate flowrate and did not respond with other manipulated variables (x_{MC} and x_{HC}). For the second manipulated variable for both configurations, which is side flowrate, the values of λ_{22} are 0.99421 and 0.97339, which are close to unity and these indicate that the side flowrate can control the side composition (x_{MC}) with a very small interference from other controlled variables (x_{LC} and x_{HC}). Same goes to λ_{33}, the effect of manipulated variables of vapor boilup in L-S-V and bottom flowrate in L-S-B on bottom composition (x_{HC}) is substantial compared to other controlled variables with the value of 0.99421 and 0.97339, respectively.

Based on the RGA analysis results, the effect of interaction in the D-S-V and D-S-B configurations was higher than unity compared to the L-S-V and L-S-B configurations. In other words, it can be concluded that L-S-V and L-S-B configurations are the best options. With regards to manipulated and controlled variable pairings, the RGA analysis shows that no cross pairing should be implemented on the L-S-V and L-S-B configurations. As a result, the reflux flowrate will control the distillate product (x_{LC}), side flowrate will control the side product (x_{MC}), and bottom vapor boilup would control the bottom product (x_{HC}).

5. Conclusion

In this paper, a systematic approach of modelling complex distillation column with port and stream connectivity was introduced. The method has been applied to modelling of DWC. The proposed method provides a simpler way to model an EO based process by defining the input/output variables of the unit block and standardizing the variables through the existing unit block equation system. However, some aspects should be thoroughly reviewed particularly in solving a large mathematical problem such as verification/classification of variables, DOF, and model structure. Failure to do so leads to errors and unsolved problems. The developed approach had been compared with two case studies for verification and validation purpose and shows good convergence. This approach can be applied on other process system and does not only

applicable on DWC. The model was also extended to RGA analysis. For the fatty acid fractionation, L-S-V and L-S-B configurations are the best control configurations. The analysis also shows that reflux flowrate, side flowrate and vapor boilup are best to control distillate product, side product and bottom product, respectively.

Conflict of interest

The authors declare that they have no conflict of interest.

Acknowledgements

References

1. Aly G, Ashour I. Applicability of the perturbed hard chain equation of state for simulation of distillation processes in the oleochemical industry. Part I: Separation of Fatty Acids. Separation Science and Technology 1992; 27(7): 955–974. Available from: http://doi.org/10.1080/01496399208019735

2. Illner M, Othman MR. Modelling and simulation of a dividing wall column for separation of fatty acid in oleochemical industries; 2014 Oct 29; Kuala Lumpur. Taylor's University & IChemE, Kuala Lumpur: SOMChE & RSCE 2014 Conference; 2014. p. 1–9.

3. Dunnebier G, Pantelides CC. Optimal design of thermally coupled distillation columns. Industrial & Engineering Chemistry Research 1999; 38(1): 162–176.

4. Pattison RC, Gupta AM, Baldea M. Equation-oriented optimization of process flowsheets with dividing-wall columns. AIChE Journal 2015; 62(3): 704–716. doi: 10.1002/aic.15060

5. Kuntsche S, Barz T, Kraus R, et al. MOSAIC a web-based modeling environment for code generation. Computers & Chemical Engineering 2011; 35(11): 2257–2273. Available from: http://doi.org/10.1016/j.compchemeng.2011.03.022

6. Marchetti M, Rao A, Vickery D. Mixed mode simulation — Adding equation oriented convergence to a sequential modular simulation tool. Computer

Aided Chemical Engineering 2001; 9: 231–236. Available from: http://doi.org/10.1016/S1570-7946(01)80034-1

7. Pantelides CC, Nauta M, Matzopoulos M, et al. Equation-oriented process modelling technology: recent advances & current perspectives; 2015 Feb; Abu Dhabi, UAE. Abu Dhabi, UAE: 5th Annual TRC-Idemitsu Workshop; 2015.

8. Gani R, Cameron IT, Lucia A, et al. Process Systems Engineering, 2. Modeling and Simulation. Ullmann's Encyclopedia of Industrial Chemistry 2012. Available from: http://doi.org/10.1002/14356007.o22_o06

9. Nguyen TD, Rouzineau D, Meyer M, et al. Design and simulation of divided wall column: Experimental validation and sensitivity analysis. Chemical Engineering and Processing: Process Intensification 2016; 104: 94–111. Available from: http://doi.org/10.1016/j.cep.2016.02.012

10. Chemtech S, Acid A, Separation A, et al. Separation technology for the chemical process industry [Internet]. Switzerland: Sulzer Ltd.; 2017. Available from: https://www.sulzer.com

11. IPS Engineering. Oleochemical processing plant. Angers, France: IPS Engineering; 2014. Available from: https://www.ips.engineering

12. Sankaranarayanan D, Deepakkumar G. Implementing the concept of relative gain array for the control of MIMO system: Applied to distillation column. Annals University Regional Centre, Coimbatore, India 2015; 4648–4653.

13. Koko IOM, Barakat TAM. Modelling and control analysis of dividing wall distillation columns. University of Khartoum Engineering Journal (UofKEJ) 2015; 5(1): 18–25.

14. Mutalib MIA, Smith R. Operation and control of dividing wall distillation columns. Chemical Engineering Research and Design 1998; 76(3): 319–334. Available from: http://doi.org/10.1205/026387698524965

15. Cho Y, Kim B, Kim D, et al. Operation of divided wall column with vapor sidedraw using profile position control. Journal of Process Control 2009; 19(6): 932–941. Available from: http://doi.org/10.1016/j.jprocont.2008.12.003

16. Chansomwong A, Zanganeh KE, Shafeen A, et al. A decentralized control structure for a CO_2 compression, capture and purification process: An uncertain Relative Gain Array approach. IFAC Proceedings Volumes (IFAC-Papers Online) 2011; 18: 8558–8563. Available from: http://doi.org/10.3182/20110828-6-IT-1002.00663

Applied Chemical Engineering

Focus and Scope

Applied Chemical Engineering (ACE) is an international open-access academic journal dedicated to publishing highly professional research in all fields related to chemical engineering. All manuscripts are subjected to a rigorous double-blind peer review process, to ensure quality and originality. We are interested in original research discoveries. This journal also features a wide range of research in ancillary areas relevant to chemistry.

ACE publishes original research articles, review articles, editorials, case reports, letters, brief commentaries, perspectives, methods, etc.

The research topics of ACE include but are not limited to:

1. Analytical chemistry
2. Chemical engineering
3. Materials chemistry
4. Material synthesis
5. Catalysis
6. Process chemistry and technology
7. Quantum chemistry method
8. Environmental chemical engineering
9. Bio-energy, resources, pollution
10. Reaction kinetics
11. Nanotechnology and bioreactors
12. Surface, coating and film

EnPress Publisher, LLC

EnPress Publisher, LLC, is a scholastic conduit for an assembly of professionals in the domains of science, technology, medicine, engineering, education, social sciences, and many more, as a round table for their intellectual discourse and presentation, and as an instrument to galvanize research designs, policy implementation, and commercial interests, to facilitate the prevailing over their challenges and to encourage to the full advantage of their resources and true potential.

We are the intellectual and academic home for academics, educators, scholars, clinicians, corporate researchers, who all play important roles in a wide range of national and international research organizations, and whose interests, expertise, research approaches, and industry objectives from around the world coalesce together to advance significant contributions in their research and professional fields.

As an instrument of information purveyor, we seek to combine academic rigor and originality with the nuanced development of policy and practice. Via our journals, client database, online campaigns, and social media presence, we offer a platform for industry professionals to interconnect, as well as opening doors towards cost-effective solutions for them to succeed, and we confidently hope to inspire a new generation of multidisciplinary researchers, think-tank experts, policymakers and business entities to innovate and advance their knowledge across fields.